Important Notice

THE UNIVERSITY OF CALGARY

Seismic Imaging in Heterogeneous Anisotropic Media by Nonstationary Phase Shift

by

Robert James Ferguson

A THESIS

SUBMITTED TO THE FACULTY OF GRADUATE STUDIES

IN PARTIAL FULFILLMENT OF THE REQUIREMENTS FOR THE

DEGREE OF DOCTOR OF PHILOSOPHY

DEPARTMENT OF GEOLOGY AND GEOPHYSICS

CALGARY, ALBERTA

NOVEMBER, 1999

THE UNIVERSITY OF CALGARY
FACULTY OF GRADUATE STUDIES

The undersigned certify that they have read, and recommended to the Faculty of Graduate Studies for acceptance, a thesis entitled "Seismic Imaging in Heterogeneous Anisotropic Media by Nonstationary Phase Shift" submitted by Robert James Ferguson in partial fulfillment of the requirements for the degree of Doctor of Philosophy.

_____

Supervisor, Dr. G. F. Margrave,
Department of Geology and Geophysics

_____

Dr. E. S. Krebes,
Department of Geology and Geophysics

_____

Dr. L. R. Lines
Department of Geology and Geophysics

_____

Dr. M. Sacchi
Department of Physics, U of Alberta

_____

Dr. M. A. Slawinski
Department of Mechanical Engineering

_____

Date

ABSTRACT

An exploration of the theory of nonstationary filters as applied to seismic wavefield extrapolation is presented. Depth imaging methods based on nonstationary filters are developed and shown to be suitable for imaging media that are strongly heterogeneous and anisotropic.

Two elementary nonstationary filters arise naturally when deriving recursive explicit wavefield extrapolators from Taylor series or directly from the Helmholtz equation. One of them, a nonstationary combination filter, is the limiting form of more commonly implemented extrapolators such as: Split-step Fourier, Phase screen, PSPI and recursive explicit finite difference.

The elementary nonstationary filters belong to the more general class of pseudo-differential operators. An analysis based on the mathematics of pseudo-differential operators suggests two new extrapolators that are more accurate and more stable than the elementary extrapolators. They also have the desirable property of being symmetric.

ACKNOWLEDGEMENTS

For providing the physical model data used in this thesis I am grateful to Don Lawton and Helen Isaac of the Foothills Research Project (FRP) and Eric Gallant of the Consortium for Research in Elastic Wave Exploration Seismology (CREWES), all of the University of Calgary. For his technical assistance I thank Michael Loughlean of Alberta Energy Company (AEC) Ltd. Thanks also to the staff, students and sponsors of CREWES and an emphatic thank you to Henry Bland and Louise Forgues. My warmest thanks to Dr. Gary F. Margrave for his guidance throughout this enriching project.

DEDICATION

For C. D., P. E. and J. B.

TABLE OF CONTENTS

LIST OF FIGURES

CHAPTER 1

INTRODUCTION

1.0 DEFINITIONS

Recorded seismic wavefields can be used to predict wavefields in the subsurface by propagating them through an earth model using *explicit recursive extrapolators* based on the *one-way wave equation*. The extrapolators are explicit because they are implemented as filters (Berkhout, 1981). They are recursive because model variation normal to the recording surface is accommodated by recursively extrapolating the recorded wavefield through small intervals of constant velocity (Gazdag, 1978). Use of the one-way wave equation implies that the medium is a fluid and that velocity-model gradients are small. Consequently, reflections, multiple reflections, head waves and mode conversions are not generated during extrapolation (Holberg, 1988).

The purpose of predicting wavefields in the subsurface is to estimate seismic *reflectivity* from which a new earth model can be constructed at a scale much finer than in the original. The parameters of the original model are usually inferred from geologic

mapping, sonic logs or seismic semblance analysis. The recorded wavefields are usually available from a number of seismic acquisition techniques (e.g., surface recordings, vertical seismic profiles or cross-bore-hole tomography).

The *operators* of explicit one-way wavefield extrapolators have recently been recognized as *pseudo-differential* operators (Margrave and Ferguson, 1997; 1998a; 1999a; Grimbergen et al., 1998). A pseudo-differential operator is a generalization of translation-invariant (*stationary*) operators to approximately translation invariant (*nonstationary*) operators (Stein, 1993: 231). Generalizing a stationary operator, such as the constant lateral-velocity phase shift method of Gazdag (1978), to a nonstationary operator allows extrapolation of seismic wavefields through strongly heterogeneous media. The equivalence of nonstationary wavefield extrapolation and pseudo-differential operators provides access to a large mathematical literature (for introductory texts see Treves, 1980; Peterson, 1983; Stein, 1993) that, as will be shown in the context of seismic imaging, leads to better wavefield extrapolators.

Historically, the generalization of stationary phase shift to nonstationary phase shift has been done independently of nonstationary filters. For example, in the split-step-Fourier method (Stoffa et al., 1990) the phase shift operator is split into a stationary focussing term and a nonstationary shifting term resulting in good kinematic results (the correct shifting term is used) that are poorly focussed. Better approximations to the above method are available from Wu (1992) and Wu and Wu (1998). Another approximate method is the phase-shift-plus-interpolation method (*PSPI*) of Gazdag and Sguazzero (1984). Lateral velocity variation is approximated with a set of constant reference

velocities and by computing a set of wavefields with stationary phase shift. Each new wavefield corresponds in space to a local constant velocity and they are interpolated into a single result.

Margrave (1998) introduces two forms of nonstationary filters, *combination* and *convolution*, in the context of one-dimensional time-variant filtering and suggests their extension to wavefield extrapolation. Margrave and Ferguson (1997; 1999a) develop the combination extrapolator (PSPI in the nonstationary limit) and the convolution extrapolator (nonstationary phase shift: *NSPS*) and Ferguson and Margrave (1998a; 1998b; 1999) demonstrate the utility of each in depth imaging. The relative computational efficiencies of NSPS and PSPI are compared by Ferguson and Margrave (1997) and found to be equivalent. Ferguson and Margrave (1998b) implement NSPS as a depth imaging method for coincident source receiver (post stack) depth imaging.

Black et al. (1984) and Fishman and McCoy (1985) analytic expressions that are similar to PSPI in the nonstationary limit. Black et al. (1984) provide little insight into the nature of their extrapolator and Fishman and McCoy (1985) do not recognize their expression as PSPI in the nonstationary limit.

Margrave and Ferguson (1998a; 1999b) recognize that PSPI and NSPS are the transpose of one another in the space-frequency domain and can be combined to produce forms that are symmetric in the space domain. Symmetry of explicit extrapolators in the space domain is required by reciprocity considerations (Wapenaar and Grimbergen, 1998).

1.00 Nonstationary filter theory

The following is a summary of Margrave's (1998) theory of nonstationary filters. It is intended to familiarize the reader with the elementary nonstationary filters, nonstationary combination and convolution in a single coordinate prior to implementation in two coordinates as wavefield extrapolators. It also establishes the Fourier transform convention and the operator notation to be used in this thesis.

Stationary filter theory assumes that a linear filter $a(t)$ is described for all t by its response to an impulse at a fixed t $(t = t_0)$ (Figure 1.1a and b). For more complicated input (e.g. Figure 1.1c), filtering by a results in a superposition of shifted and scaled versions of the impulse response of $a(t)$ (Figures 1.1d and 1.2). This process is commonly referred to as *convolution*. A bandpass filter is an example of a linear stationary filter.

In the Fourier transform domain, the convolution of a signal h and a filter a is achieved by multiplying their respective spectra H and A

$$G(\omega) = A(\omega)H(\omega), \tag{1.1}$$

where G is the resulting spectrum and ω are the coordinates of the Fourier domain. The following Fourier transform convention is used: If t is a time coordinate the Fourier transform of h is

$$H(\omega) = \frac{1}{2\pi}\int h(t)\exp(-i\omega t)dt \quad , \tag{1.2}$$

where the limits of integration $-\infty$ to ∞ are implied. If t is a space coordinate

$$H(\omega) = \int h(t)\exp(i\omega t)dt \; . \tag{1.3}$$

1.01 Nonstationary combination

When filter a is *nonstationary* its impulse response varies with coordinates t. Similarly, its spectrum A will vary. For example, a Ricker wavelet whose center frequency changes with time is a nonstationary filter (Figures 1.3a through c). It is not obvious how to incorporate nonstationarity into the convolution equation (1.1), as there is no explicit t dependence. However, the inverse Fourier transform (assuming t = time) of equation (1.1) gives

$$g(t) = \int A(\omega)H(\omega)\exp(i\omega t)d\omega, \tag{1.4}$$

where the t dependence is now explicitly contained on the right hand side by the Fourier kernal. Allowing A to vary with t at this point results in the nonstationary *combination* filter of Margrave (1998)

$$g(t) = \int A(t,\omega)H(\omega)\exp(i\omega t)d\omega, \tag{1.5}$$

expressed in the *mixed* domain. Margrave (1998) calls this a mixed domain filter because A is defined simultaneously in both the Fourier and inverse Fourier domains. Note that

nonstationary filter A varies according to the coordinate t of the output. Combination filters tend to give discontinuous results (Figure 1.3d).

The nonstationary combination filter in equation (1.5) is also a *pseudo-differential* operator equation (Stein, 1993: 231) of the form

$$g(t) = [L_A H(\omega)](t) = \int A(t,\omega) H(\omega) \exp(i\omega t) d\omega, \tag{1.6}$$

where L_A is a *pseudo-differential* operator and A is its *symbol*. (This operator notation is used in Chapters 5 and 6).

1.02 Nonstationary convolution

An alternate to nonstationary combination is nonstationary *convolution* (Margrave, 1998). In equation (1.1), replace spectrum H with the Fourier transform of h

$$G(\omega) = A(\omega) \frac{1}{2\pi} \int h(t) \exp(-i\omega t) dt \tag{1.7}$$

.

Because at this point A is stationary, move A inside the Fourier integral

$$G(\omega) = \frac{1}{2\pi} \int A(\omega) h(t) \exp(-i\omega t) dt \tag{1.8}$$

,

now allow it to vary with t

$$G(\omega) = \frac{1}{2\pi} \int A(t,\omega) h(t) \exp(-i\omega t) dt \quad , \tag{1.9}$$

or in the operator notation introduced above

$$G(\omega) = [L_A h(t)](\omega) = \frac{1}{2\pi} \int A(t,\omega) h(t) \exp(-i\omega t) dt \quad . \tag{1.10}$$

Nonstationary convolution (equations (1.9) and (1.10)) applies A to signal h simultaneously with a Fourier transform. In contrast, nonstationary combination (equations (1.5) and (1.6)) applies A to spectrum H simultaneously with an inverse Fourier transform. Also, A as a convolution filter varies with the input coordinates (e.g., the coordinates corresponding to h), where in a combination filter A varies with output coordinates (e.g., those corresponding to g). In contrast to combination filters, convolution filters tend to produce continuous looking results (Figure 1.3e).

1.1 THESIS OBJECTIVE

The objective of this thesis is to quantify the performance of the elementary nonstationary combination and convolution filters, implemented as wavefield extrapolators in seismic imaging and, where possible, to suggest superior alternatives. This is done both experimentally using a combination of real and synthetic data representing heterogeneous and heterogeneous-anisotropic media and analytically through the mathematics of nonstationary filters and pseudo-differential operators.

In Chapter 2, the elementary filters of nonstationary phase shift, PSPI and NSPS, are derived from the scalar wave equation in a process patterned on the development of

nonstationary filters presented in subsections **1.00** through **1.02** above. That is, stationary phase shift is derived first and then generalized to the two elementary nonstationary forms. An adjoint relationship between PSPI and NSPS is proved and, from this result, the first of two new symmetric extrapolators is introduced.

Chapter 3 is an evaluation of the symmetric extrapolator presented in Chapter 2 using an algorithm that estimates the seismic reflectivity of a heterogeneous subsurface based on a single seismic source gather. For a collection of overlapping source gathers, a seismic image results by stacking the reflectivity estimates. This new prestack depth migration is applied to a widely available synthetic dataset (the Marmousi model) and is shown to provide an accurate image.

The depth-imaging algorithm presented in Chapter 3 is then extended to anisotropic media. Chapter 4 begins with a review of transverse isotropy (TI), a common form of anisotropy and it is a digest of expositions on this subject by a number of different authors leading to the equation for P-wave velocity in a dipping TI medium. Stationary phase shift for TI media (homogeneous anisotropic) is first derived to make obvious the adaptation from isotropy to anisotropy and a number of imaging examples are presented. A prestack algorithm is then developed for nonstationary TI media (heterogeneous anisotropic) and a physical model is used to demonstrate the superiority of this method over an isotropic algorithm.

In Chapter 5, an alternate derivation of the elementary extrapolators is presented based on the Taylor series representation of the extrapolated wavefield. This derivation

establishes the link between PSPI and more commonly implemented recursive explicit extrapolators and indicates they are all approximate forms of PSPI. No common analogue is found for NSPS. The first of two accuracy and stability analyses is given in this Chapter and a second symmetric extrapolator is introduced. The operator notation introduced in section **1.01** is implemented here to simplify the discussion of the various nonstationary extrapolators. For forward (+) extrapolation, PSPI becomes linear operator L_P^+, NSPS becomes L_N^+ and the symmetric operators become L_{PN}^+ (from Chapter 2) and L_A^+ (from Chapter 5). The symmetric extrapolators L_{PN}^+ and L_A^+ are found by numerical experiment to have greater accuracy and stability than the elementary extrapolators.

A more rigorous comparison of L_P^+, L_N^+, L_{PN}^+ and L_A^+ is presented in Chapter 6. The mathematical analogues of the numerical experiments of Chapter 5 are derived and a first order proof of the superior accuracy and stability of L_{PN}^+ and L_A^+ is given.

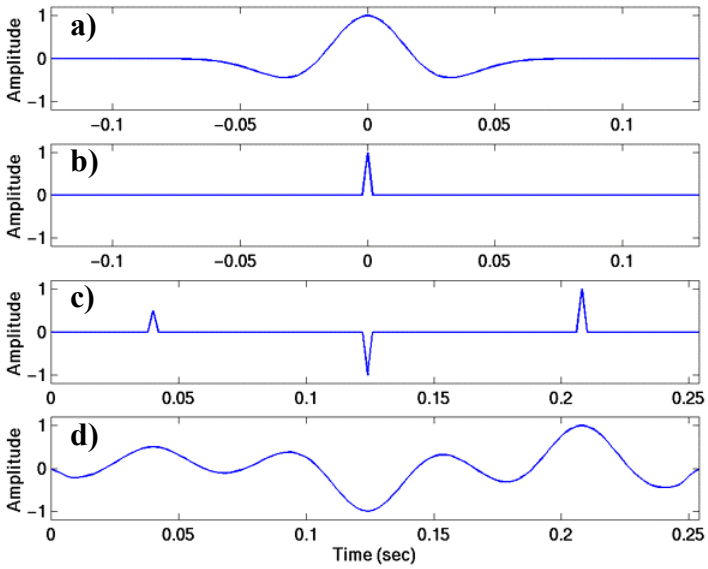

Fig. 1.1. a) The response of filter *a* (a Ricker wavelet with a center frequency of 15Hz) to a unit impulse at $t = 0$. b) is a unit impulse at $t = 0$. c) is the input signal *h*. d) is the result of filtering *h* with *a*.

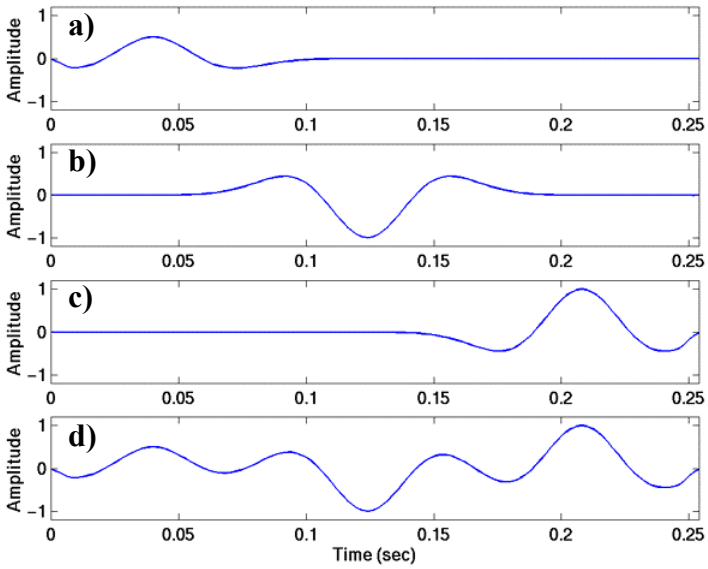

Fig. 1.2. The application of filter *a* to input signal *h* (Figure 1.1d) as a superposition of scaled and time delayed impulse responses. Filter *a* is a Ricker wavelet with a 15Hz center frequency. In a) the impulse response in Figure 1.1a is centered on the first nonzero element of *h* (Figure 1.1c) and scaled to that nonzero value. Similarly b) and c). d) The superposition of a), b) and c) equals the convolution output of Figure 1.1d.

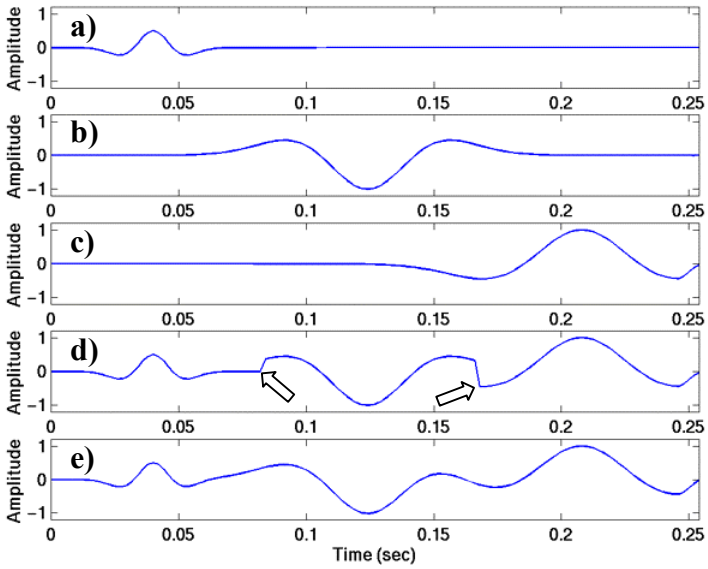

Fig. 1.3. The application of two nonstationary filters. At $t = 0$ filter *a* is a Ricker wavelet with a center frequency of 30Hz. At .082 seconds it abruptly changes to a 15Hz wavelet. It remains at 15Hz until .16 seconds where it abruptly becomes a 10Hz wavelet. a) the impulse response of *a* between .04 seconds is a 30Hz Ricker wavelet. b) at .12 seconds it is a 15Hz wavelet. c) at .21 seconds it is 10Hz wavelet. d) a nonstationary combination filter that mimics the filter response of a) through c) has been applied to the input signal *h* of Figure 1.1c. Combination filters tend to produce discontinuities (as indicated by the arrows) in the output signal where there are discontinuities in the filter. e) the corresponding nonstationary convolution filter has been applied to the input signal *h* of Figure 1.1c. Nonstationary convolution filters tend to produce continuous looking output.

CHAPTER 2

THE ELEMENTARY WAVEFIELD EXTRAPOLATORS

2.0 INTRODUCTION

In this Chapter the nonstationary combination filter (equation 1.5) and the nonstationary convolution filter (equation 1.9) are shown to arise naturally in the derivation of wavefield extrapolators from the Helmholtz equation. A derivation is presented that results in a stationary wavefield extrapolator (velocity is invariant) that has the same form as the filter in equation (1.4). From the stationary extrapolator the nonstationary extrapolators, corresponding to combination and convolution, are then derived. An adjoint relationship between the two extrapolators is demonstrated and a new symmetric wavefield extrapolator is presented.

2.1 REVIEW OF CONSTANT VELOCITY PHASE SHIFT

A review of constant-velocity phase shift (Gazdag, 1978) is helpful in understanding its nonstationary (variable-velocity) extension. The phase-shift method is most useful in situations where only macro contrasts in the required velocity model are

known in depth so, reflections, multiple reflections, head waves and mode conversions cannot be modeled and the elastic wave equation is unnecessary. Propagation is assumed governed by the scalar wave equation and Fourier transforms are used to decompose seismic wavefields into plane waves that are phase shifted from the surface to new depths. The results are then inverse Fourier transformed into new wavefields that are used to estimate reflectivity. In the classical derivation, velocity must remain constant in all coordinates. However, if the subsurface is divided into depth intervals of differing velocities, then wavefields can be phase shifted one depth interval at a time and reflectivity estimated at each depth. The output of one phase shift becomes the input to the next and so on. Continuous velocity variation in depth is then accommodated in the limit of infinitesimally small depth intervals.

Assuming a monochromatic wavefield ψ of frequency ω and spatial coordinates $\mathbf{x_0} = (x, y, z)$ where

$$\psi(\mathbf{x_0}, t) = \int \psi(\mathbf{x_0}, \omega) \exp(i\omega t) d\omega, \tag{2.1}$$

a scalar wave equation for heterogeneous media is

$$\nabla_0^2 \psi(\mathbf{x_0}, \omega) = -\left(\frac{\omega}{c(\mathbf{x_0})} \right)^2 \psi(\mathbf{x_0}, \omega), \tag{2.2}$$

where ∇_0^2 is the Laplacian with respect to coordinates $\mathbf{x_0}$. The wavefield ψ can be represented by an inverse Fourier transform of its spectrum φ

$$\psi(\mathbf{x_0},\omega)=\frac{1}{(2\pi)^3}\int\varphi(\mathbf{k_0},\omega)\exp(-i\mathbf{x_0}\cdot\mathbf{k_0})d\mathbf{k_0}, \tag{2.3}$$

where coordinates $\mathbf{k_0}=(k_x,k_y,k_z)$ are the Fourier duals (wavenumbers) of $\mathbf{x_0}$. Replace ψ in equation (2.2) with equation (2.3) and compute the partial derivatives

$$\int[\mathbf{k_0}\cdot\mathbf{k_0}]\varphi(\mathbf{k_0},\omega)\exp(-i\mathbf{x_0}\cdot\mathbf{k_0})d\mathbf{k_0}=\left(\frac{\omega}{c(\mathbf{x_0})}\right)^2\int\varphi(\mathbf{k_0},\omega)\exp(-i\mathbf{x_0}\cdot\mathbf{k_0})d\mathbf{k_0}\,. \tag{2.4}$$

Then, Fourier transform equation (2.4)

$$[\mathbf{k_0}\cdot\mathbf{k_0}]\varphi(\mathbf{k_0},\omega)=\int\varphi(\mathbf{k_0}',\omega)\int\left(\frac{\omega}{c(\mathbf{x_0})}\right)^2\exp(-i\mathbf{x_0}\cdot[\mathbf{k_0}'-\mathbf{k_0}])d\mathbf{x_0}d\mathbf{k_0}', \tag{2.5}$$

where the order of integration has been reversed. Variation of c with $\mathbf{x_0}$ complicates evaluation of the right hand side of equation (2.5). However, a simple result is obtained if c is constrained to be constant. Thus, for a homogeneous medium $c(\mathbf{x_0})=c$, equation (2.5) reduces to

$$[\mathbf{k_0}\cdot\mathbf{k_0}]\varphi(\mathbf{k_0},\omega)=\left(\frac{\omega}{c}\right)^2\int\varphi(\mathbf{k_0}',\omega)\delta(\mathbf{k_0}'-\mathbf{k_0})d\mathbf{k_0}' \tag{2.6}$$

or,

$$\left[\mathbf{k}_0 \cdot \mathbf{k}_0\right] = \left(\frac{\omega}{c}\right)^2 . \tag{2.7}$$

Equation (2.7) is known as the dispersion relation for scalar waves that can be written as

$$\left[k_z^2 + \mathbf{k} \cdot \mathbf{k}\right] = \left(\frac{\omega}{c}\right)^2 \Rightarrow k_z = \pm\sqrt{\left(\frac{\omega}{c}\right)^2 - \mathbf{k} \cdot \mathbf{k}}\,, \tag{2.8}$$

where $\mathbf{k} = \left(k_x, k_y\right)$. Spectrum φ in equation (2.3) can be modified to force the k_z dependence of equation (2.8)

$$\varphi(\mathbf{k}, k_z, \omega) = \varphi_1(\mathbf{k}, \omega)\delta\left(k_z + \sqrt{\left(\frac{\omega}{c}\right)^2 - \mathbf{k} \cdot \mathbf{k}}\right) + \varphi_2(\mathbf{k}, \omega)\delta\left(k_z - \sqrt{\left(\frac{\omega}{c}\right)^2 - \mathbf{k} \cdot \mathbf{k}}\right),$$

(2.9)

where φ_1 and φ_2 are arbitrary functions of $(\mathbf{k}, \omega)$ to be determined from boundary conditions. The k_z dependence is contained entirely by delta functions, whose action in equation (2.3) is to replace k_z everywhere and collapse the k_z integral. Thus

$$\psi(\mathbf{x}, z, \omega) = \frac{1}{(2\pi)^2}\int\left[\alpha(\mathbf{k}, z, \omega)\varphi_1(\mathbf{k}, \omega) + \alpha(\mathbf{k}, -z, \omega)\varphi_2(\mathbf{k}, \omega)\right]\exp(-i\mathbf{x} \cdot \mathbf{k})d\mathbf{k}\,,$$

(2.10)

where the *phase-shift extrapolator* is

$$\alpha(\mathbf{k}, \pm z, \omega) = \exp\left(\pm iz \sqrt{\left(\frac{\omega}{c}\right)^2 - \mathbf{k} \cdot \mathbf{k}} \right), \qquad (2.11)$$

and z increases downward. Equation (2.10) defines ψ for all z and separates φ into up travelling (φ_1) and down travelling (φ_2) components as can be seen in the sign dependence on z. In the absence of vertical-velocity gradients, but for arbitrary lateral gradients, φ_1 and φ_2 propagate independently of each other (Fishman and McCoy, 1985). Evaluation of equation (2.10) at $z = 0$ gives $\varphi_1 + \varphi_2$ as the spectrum of ψ recorded at the surface $z = 0$

$$\psi(\mathbf{x},0) = \frac{1}{(2\pi)^2} \int [\varphi_1(\mathbf{k}) + \varphi_2(\mathbf{k})] \exp(-i\mathbf{x} \cdot \mathbf{k}) d\mathbf{k} \qquad (2.12)$$

(the dependence on ω has been suppressed). The complete determination of spectra φ_1 and φ_2 requires the first-depth derivative of wavefield ψ evaluated at $z = 0$ as a second boundary condition. Since the derivative is generally not available, the common assumption is made that only waves travelling upwards are recorded. Then $\varphi_2 = 0$ and equation (2.10) reduces to

$$\psi(\mathbf{x}, z) = \frac{1}{(2\pi)^2} \int \alpha(\mathbf{k}, z) \varphi(\mathbf{k}) \exp(-i\mathbf{x} \cdot \mathbf{k}) d\mathbf{k} \,. \qquad (2.13)$$

Equation (2.13) allows $\psi(z = 0)$ to be extrapolated to any depth z. It is also directly comparable to the stationary filter equation (1.4) developed earlier, except that equation (2.13) is implemented in two spatial coordinates instead of a single time coordinate.

2.2 NONSTATIONARY PHASE SHIFT

As demonstrated in section **2.1**, wavefields phase shifted in constant velocity media are exact solutions to the scalar wave equation. For laterally heterogeneous velocity, three alternative approximations are developed here using nonstationary filter concepts (Margrave, 1998). One is proposed by Margrave and Ferguson (1997; 1998a; 1999a) and is referred to as nonstationary phase shift (NSPS). Margrave and Ferguson (1997; 1998a; 1999a) recognize the other as the phase-shift-plus-interpolation method (PSPI) (Gazdag and Sguazzero, 1984) applied in the limit of continuous velocity variation. (The continuous form of PSPI contains no interpolation.) A third method derived here combines NSPS and PSPI into a single operator that has the desirable property of being symmetric in the $(\mathbf{x},\omega)$ domain. NSPS and PSPI also correspond to, respectively, the standard and adjoint standard forms of pseudo-differential operators whose symbols are the nonstationary phase-shift extrapolator α.

In the same way that the stationary filter equation (1.4) was made nonstationary, a direct way to accommodate laterally variable velocity in equation (2.13) is to simply allow α to have $\mathbf{x}$ dependence through $c(\mathbf{x})$. That is,

$$\psi(\mathbf{x},z)=\frac{1}{(2\pi)^2}\int\alpha(\mathbf{x},\mathbf{k},z)\varphi(\mathbf{k},0)\exp(-i\mathbf{x}\cdot\mathbf{k})d\mathbf{k}\,, \tag{2.14}$$

where the nonstationary extrapolator is

$$\alpha(\mathbf{x},\mathbf{k},z) = \exp\left(iz\sqrt{\left(\frac{\omega}{c(\mathbf{x})}\right)^2 - \mathbf{k}\cdot\mathbf{k}}\right). \qquad (2.15)$$

In equation (2.14) $\mathbf{x}$ corresponds to the *output* lateral coordinates and, like A in the nonstationary combination filter equation (1.5), α is controlled by the output coordinates. Equation (2.14) applies a nonstationary phase shift carrying the spectrum $\varphi(z=0)$ to a new depth simultaneous with transformation to space coordinates. Black et al. (1984) and Fishman and McCoy (1985) suggest the same simple extension to constant-velocity phase-shift, but do not recognize PSPI in the limit of continuously variable velocity.

Equation (2.14) is a standard-form pseudo differential operator (Stein, 1993: 231) where $\alpha(\mathbf{x},\mathbf{y},z)$ is the symbol of the operator. It can be written to explicitly contain the input wavefield by replacing $\varphi(z=0)$ with the Fourier transform of $\psi(z=0)$

$$\psi(\mathbf{x},z) = \int \psi(\mathbf{y},0) A(\mathbf{x},\mathbf{y},z)\, d\mathbf{y}\,, \qquad (2.16)$$

where,

$$A(\mathbf{x},\mathbf{y},z) = \frac{1}{(2\pi)^2}\int \alpha(\mathbf{x},\mathbf{k},z)\exp(i[\mathbf{y}-\mathbf{x}]\cdot\mathbf{k})\, d\mathbf{k}\,, \qquad (2.17)$$

and $\mathbf{y}$ corresponds to the lateral coordinates (*input* coordinates) at $z = 0$.

Margrave and Ferguson (1998b) demonstrate, in two spatial dimensions, that extrapolators based on nonstationary combination are not exact solutions to the wave

equation. In three spatial dimensions replacement of nonstationary combination equation (2.14) into the wave equation (2.2) results in the following error term:

$$\varepsilon_{comb} = \iint \left[2z\mathbf{k} \cdot \nabla k_z(\mathbf{x},\mathbf{k}) - z^2 \nabla k_z(\mathbf{x},\mathbf{k}) \cdot \nabla k_z(\mathbf{x},\mathbf{k},z) + iz\nabla^2 k_z(\mathbf{x},\mathbf{k}) \right] \psi(\mathbf{y},0) \exp\left(ik_z(\mathbf{x},\mathbf{k}) - i\mathbf{k} \cdot [\mathbf{x}-\mathbf{y}] \right) d\mathbf{y} d\mathbf{k} \tag{2.18}$$

where k_z is the vertical wavenumber related to symbol α (equation 2.15)

$$k_z(\mathbf{x},\mathbf{k}) = \sqrt{\left(\frac{\omega}{c(\mathbf{x})} \right)^2 - \mathbf{k} \cdot \mathbf{k}} \, . \tag{2.18a}$$

Operator ∇ is the gradient $\frac{\partial}{\partial x}\mathbf{i} + \frac{\partial}{\partial y}\mathbf{j}$ and ∇^2 is the Laplacian $\frac{\partial^2}{\partial x^2} + \frac{\partial^2}{\partial y^2}$. For constant velocity *c* the error vanishes.

An alternate variable-velocity phase shift follows by returning to the constant velocity case (equation (2.13)) and Fourier transforming

$$\varphi(\mathbf{k},z) = \alpha(\mathbf{k},z)\varphi(\mathbf{k},0). \tag{2.19}$$

Next, replace $\varphi(z=0)$ with the Fourier transform of $\psi(z=0)$

$$\varphi(\mathbf{k},z) = \alpha(\mathbf{k},z) \int \psi(\mathbf{y},0) \exp(i\mathbf{y} \cdot \mathbf{k}) d\mathbf{y} \, . \tag{2.20}$$

Since velocity is independent of position, α can be moved inside the Fourier integral

$$\varphi(\mathbf{k},z)=\int\psi(\mathbf{y},0)\alpha(\mathbf{k},z)\exp(i\mathbf{y}\cdot\mathbf{k})d\mathbf{y}\,. \tag{2.21}$$

Velocity is now allowed to vary with input coordinate **y**

$$\varphi(\mathbf{k},z)=\int\alpha(\mathbf{y},\mathbf{k},z)\psi(\mathbf{y},0)\exp(i\mathbf{y}\cdot\mathbf{k})d\mathbf{y}\,. \tag{2.22}$$

Equation (2.22) is a nonstationary phase shift carrying wavefield $\psi(z=0)$ to a new depth simultaneous with a transformation to wavenumbers and is recognizable as a nonstationary convolution filter like equation (2.20). Margrave and Ferguson (1997; 1998a; 1999a) describe this form for seismic imaging calling it nonstationary phase shift (NSPS). Equation (2.22) is a kind of pseudo-differential operator that has the same symbol α as equation (2.14).

Similar to the error equation (2.18) above, extrapolators based on nonstationary convolution are not exact solutions to the wave equation (Margrave and Ferguson, 1998b). In three spatial dimensions replacement of nonstationary convolution equation (2.22) into the wave equation (2.2) gives the following error term:

$$\varepsilon_{conv}=\iint\left[\left(\frac{\omega}{c(\mathbf{x})}\right)^2-\left(\frac{\omega}{c(\mathbf{y})}\right)^2\right]\psi(\mathbf{y},0)\exp(ik_z(\mathbf{y},\mathbf{k})-i\mathbf{k}\cdot[\mathbf{x}-\mathbf{y}])d\mathbf{y}d\mathbf{k} \tag{2.23}$$

where k_z is now a function of input spatial coordinates **y**. For nonstationary convolution, error is not a function of the spatial derivatives of k_z as it is for nonstationary combination. Again, for stationary velocity *c*, the error vanishes. Margrave and Ferguson

(1998b) suggest that nonstationary combination extrapolators are more sensitive to lateral velocity gradients where convolution extrapolators are more sensitive to the size of the depth step z.

Equations (2.22) and (2.14) are adjoints when the sign on z in one of them is reversed. To demonstrate, inverse Fourier transform equation (2.22) to achieve a space domain expression similar to equation (2.16)

$$\psi(\mathbf{x},z)=\int\psi(\mathbf{y},0)B(\mathbf{x},\mathbf{y},z)d\mathbf{y}\,, \tag{2.24}$$

where,

$$B(\mathbf{x},\mathbf{y},z)=\frac{1}{(2\pi)^2}\int\alpha(\mathbf{y},\mathbf{k},z)\exp(i[\mathbf{y}-\mathbf{x}]\cdot\mathbf{k})d\mathbf{k}\,. \tag{2.25}$$

To prove the adjoint relationship it is only necessary to show that the adjoint of $B(\mathbf{x},\mathbf{y},z)$ is $A(\mathbf{x},\mathbf{y},-z)$. That is

$$\begin{aligned} B^{\dagger}(\mathbf{y},\mathbf{x},z)&=\frac{1}{(2\pi)^2}\int\alpha(\mathbf{y},\mathbf{k},-z)\exp(-i[\mathbf{y}-\mathbf{x}]\cdot\mathbf{k})d\mathbf{k}\\ &=\frac{1}{(2\pi)^2}\int\alpha(\mathbf{x},\mathbf{k},-z)\exp(i[\mathbf{y}-\mathbf{x}]\cdot\mathbf{k})d\mathbf{k}\\ &=A(\mathbf{x},\mathbf{y},-z) \end{aligned}\,, \tag{2.26}$$

where superscript † represents the adjoint (Hermitian conjugate). (Velocity variation at **x** and **y** must be the same for equation (2.26) to hold.) Thus, the adjoint of the NSPS operator B is the PSPI operator A with the depth value z changed in sign. Similarly, the adjoint of PSPI is NSPS propagating in the opposite direction.

2.3 A NEW SYMMETRIC NONSTATIONARY PHASE SHIFT

The complimentary relationship between NSPS and PSPI, described in section **2.2**, suggests that it is natural to combine them into a third variable-velocity phase shift that may perform better than PSPI or NSPS alone. Etgen (1994) demonstrates operators like PSPI can become unstable in the presence of instantaneous velocity contrasts of thousands of meters-per-second. Margrave and Ferguson (1999b), expanding on the work of Etgen (1994), demonstrate that the NSPS operator also suffers from instability, but that a hybrid of the two, dubbed symmetric nonstationary phase shift (SNPS), has greater stability. The SNPS operator is shown to have the spatial symmetry required by reciprocity (Wapenaar and Grimbergen, 1998). It is also the first of two symmetric wavefield extrapolators presented in this thesis.

The symmetric operator (i.e., its kernel equals its transpose) results by phase shifting from 0 to $z/2$ by NSPS and from $z/2$ to z by PSPI or vice versa. (Note: PSPI followed by NSPS is symmetric but does not result in an identical extrapolator.) For example, using equation (2.22), phase shift $\psi(z=0)$ from 0 to $z/2$ by NSPS

$$\varphi(\mathbf{k}, z/2) = \int \alpha(\mathbf{y}, \mathbf{k}, z/2)\psi(\mathbf{y}, 0)\exp(i\mathbf{y}\cdot\mathbf{k})d\mathbf{y}\,. \tag{2.27}$$

Next, using equation (2.14), phase shift from $z/2$ to z by PSPI

$$\psi(\mathbf{x},z)=\frac{1}{(2\pi)^2}\int\alpha(\mathbf{x},\mathbf{k},z/2)\varphi(\mathbf{k},z/2)\exp(-i\mathbf{x}\cdot\mathbf{k})d\mathbf{k}\,. \qquad (2.28)$$

Replace φ in equation (2.28) by equation (2.27) and switch the order of integration to give

$$\psi(\mathbf{x},z)=\int\psi(\mathbf{y},0)C(\mathbf{x},\mathbf{y},z)d\mathbf{y}\,, \qquad (2.29)$$

where *C*, the kernal of the SNPS operator, is defined as

$$C(\mathbf{x},\mathbf{y},z)=\frac{1}{(2\pi)^2}\int\alpha(\mathbf{y},\mathbf{k},z/2)\alpha(\mathbf{x},\mathbf{k},z/2)\exp(-i\mathbf{k}\cdot[\mathbf{x}-\mathbf{y}])d\mathbf{k}\,. \qquad (2.30)$$

Equation (2.29) is an $(\mathbf{x},\omega)$ form of a nonstationary phase shift that combines NSPS and PSPI in a single symmetric operator *C* (equation (2.30)). The symmetry of *C* is evident by its invariance under the exchange of coordinates **y** and **x**. The SNPS extrapolator is an explicit extrapolator suitable for 2D or 3D depth migration in complex media. Wapenaar and Grimbergen (1998) use reciprocity concepts to argue that such extrapolators should be symmetric in the $(\mathbf{x},\omega)$ domain. Note that ordinary phase shift has such symmetry and has the property that the adjoint operation simply reverses the extrapolation. SNPS has these same properties.

2.4 CHAPTER SUMMARY

In this Chapter the elementary wavefield extrapolators PSPI (corresponding to nonstationary combination) and NSPS (corresponding to nonstationary convolution) were

derived from the Helmholtz equation. They were shown to have an adjoint relationship that suggests the development of a third symmetric extrapolator SNPS.

CHAPTER 3

DEPTH IMAGING BY NONSTATIONARY PHASE SHIFT

3.0 INTRODUCTION

At a particular depth, the ratio of the source (incident) seismic wavefield ψ_S and the reflected seismic wavefield ψ_R defines seismic reflectivity *r* that can be related to rock properties (e.g., P-wave velocity, S-wave velocity, density). By recursively phase shifting the reference wavefields, $\psi_S(z=0)$ and $\psi_R(z=0)$, to depths $z=(0,z_1,z_2,...,z_n)$ *r* is estimated for all coordinates relevant to the recording aperture. By recursive, a process like the following is meant: 1) $\psi_S(z=0)$ and $\psi_R(z=0)$ are phase-shifted to $\psi_S(z_1)$ and $\psi_R(z_1)$ respectively and $r(z_1)$ is computed; 2) $\psi_S(z_1)$ and $\psi_R(z_1)$ are phase-shifted to $\psi_S(z_2)$ and $\psi_R(z_2)$ respectively and $r(z_2)$ is computed; and 3) the process continues until *r* for the final depth level z_n is computed.

3.1 PRESTACK DEPTH IMAGING

For any depth, ψ_S and ψ_R are not directly measurable but can be deduced from a surface recording $\psi_R(z=0)$ and a model of the source $\psi_S(z=0)$. For example, phase shifting $\psi_R(z=0)$ to a new depth z is achieved with SNPS (equation (2.27))

$$\psi_R(\mathbf{x},z,t) = \int\int \psi_R(\mathbf{y},0,\omega) C(\mathbf{x},\mathbf{y},z,\omega) d\mathbf{y} \exp(i\omega t) d\omega, \tag{3.1}$$

where ω is here explicitly stated. Phase shifting $\psi_S(z=0)$ is similarly described by,

$$\psi_S(\mathbf{x},z,t) = \int\int \psi_S(\mathbf{y},0,\omega) C(\mathbf{x},\mathbf{y},-z,\omega) d\mathbf{y} \exp(i\omega t) d\omega. \tag{3.2}$$

In equation (3.2) the sign reversal on z in C is required to extrapolate downward-travelling waves down while equation (3.1) moves upward-travelling waves down. Amplitudes characteristic of geometric spreading are contained in ψ_R and ψ_S and amplitude variations characteristic of material contrasts are only found in ψ_R. Their ratio defines reflectivity r at depth z

$$r(\mathbf{x},z) = \frac{\psi_R(\mathbf{x},z,t=\tau(\mathbf{x},z))}{\psi_S(\mathbf{x},z,t=\tau(\mathbf{x},z))}, \tag{3.3}$$

where time τ is the instant ψ_S is converted into ψ_R (Temme, 1984). The required amplitudes of ψ_R and ψ_S at $t = \tau$ must be picked (Temme, 1984; Berryhill, 1979, 1984).

An implementation of equation (3.3) that avoids picking reflections is to replace ψ_R and ψ_S with their inverse Fourier transforms

$$r(\mathbf{x},z)=\frac{\int_{-\infty}^{\infty}\psi_R(\mathbf{x},z,\omega)\exp(i\omega\tau(\mathbf{x},z))d\omega}{\int_{-\infty}^{\infty}\psi_S(\mathbf{x},z,\omega)\exp(i\omega\tau(\mathbf{x},z))d\omega}, \tag{3.4}$$

then for r independent of ω

$$\int_{-\infty}^{\infty}[\psi_R(\mathbf{x},z,\omega)-r(\mathbf{x},z)\psi_S(\mathbf{x},z,\omega)]\exp(i\omega\tau(\mathbf{x},z))d\omega=0\,. \tag{3.5}$$

Equation (3.5) is satisfied if

$$r(\mathbf{x},z)=\frac{\psi(\mathbf{x},z,\omega)_R}{\psi(\mathbf{x},z,\omega)_S}\,. \tag{3.6}$$

Equation (3.6) corresponds to a single temporal frequency or *monochromatic* estimate of reflectivity. Averaging r over the range of available ω gives

$$\begin{aligned}\tilde{r}(\mathbf{x},z)&=\frac{1}{[\omega_{\max}-\omega_{\min}]}\left[\int_{-\omega_{\max}}^{-\omega_{\min}}\frac{\psi_R(\mathbf{x},z,\omega)}{\psi_S(\mathbf{x},z,\omega)}d\omega+\int_{\omega_{\min}}^{\omega_{\max}}\frac{\psi_R(\mathbf{x},z,\omega)}{\psi_S(\mathbf{x},z,\omega)}d\omega\right],\\&=\frac{1}{[\omega_{\max}-\omega_{\min}]}\int_{\omega_{\min}}^{\omega_{\max}}\left\{\frac{\psi^*{}_R(\mathbf{x},z,\omega)}{\psi^*{}_S(\mathbf{x},z,\omega)}+\frac{\psi_R(\mathbf{x},z,\omega)}{\psi_S(\mathbf{x},z,\omega)}\right\}d\omega\end{aligned} \tag{3.7}$$

where * is complex conjugation. Equation (3.7) is suitable for estimating r in variable velocity media using a recursion in depth and is equivalent to the imaging condition of

Claerbout (1971). Overlapping each source gather and summing provides an image of the subsurface.

3.2 A PRACTICAL IMPLEMENTATION OF SNPS

If lateral velocity variation is smooth, depth imaging algorithms based on NSPS, PSPI and SNPS can be optimized to reduce run time by limiting the wavenumber bandwidth of the operators (Margrave and Ferguson, 1997). Alternately, if lateral variation in velocity is blocky, then a piecewise constant approximation for the three methods can be obtained using windowing operations and multiple constant-velocity phase shifts (Margrave and Ferguson, 1999a). The latter approach is used here. Though a 2D implementation is presented, the method extends easily to 3D.

For each unique velocity v_j along coordinate *x*, a window Ω_j is constructed such that it takes on a value of 1 at every *x* location where $c(\mathbf{x})$ takes on the value v_j and is zero otherwise. After some analysis (Margrave and Ferguson, 1999a), equation (2.14) (PSPI) becomes

$$\Psi(x,z,\omega)=\sum_j \Omega_j \frac{1}{2\pi}\int_{-\infty}^{\infty}\alpha_j(k_x,z,\omega)\varphi(k_x,0,\omega)\exp(-ik_x x)dx \qquad (3.8)$$

and equation (2.21) (NSPS) is

$$\varphi(k_x, z, \omega) = \sum_j \alpha_j(k_x, z, \omega) \int_{-\infty}^{\infty} \Psi(x,0,\omega)\Omega_j \exp(ik_x x)dx, \qquad (3.9)$$

where window Ω_j is

$$\Omega_j(x) = \begin{Bmatrix} 1, v(x) = v_j \\ 0, otherwise \end{Bmatrix} \qquad (3.10)$$

and

$$\alpha_j(k_x, z, \omega) = \exp\left(iz\sqrt{\left(\frac{\omega}{v_j}\right)^2 - k_x^2} \right). \qquad (3.11)$$

Unlike equations (2.14) (PSPI) and (2.21) (NSPS) the integrals in equations (3.8) and (3.9) are Fourier integrals. Equation (3.8) constructs the PSPI space-domain wavefield by using ordinary phase-shift to extrapolate the input spectrum for each v_j. Then, windows Ω_j are applied and the resulting wavefields are superimposed. In contrast, equation (3.9) constructs the NSPS Fourier-domain wavefield by applying windows Ω_j to the input wavefield, phase shifting each result with the appropriate v_j and summing over all j. The essential difference is that windowing is the last step in PSPI and the first step in NSPS. The cost of NSPS or PSPI is proportional to the number of distinct velocities times the cost of ordinary phase shift.

Similarly, the SNPS operator has a piecewise-constant approximation that is the cascade of the NSPS and PSPI processes. Figures 3.1a, b and Figure 3.2 present a set of

flow charts that illustrate the implementation of, respectively, NSPS, PSPI and SNPS. These expressions accomplish nonstationary phase shift by the fast and relatively simple operations of constant-velocity phase shift and windowing.

3.3 MARMOUSI

The Marmousi model of the Institute Francais du Petrole (IFP) (Bourgeois et al., 1991) is used to demonstrate prestack imaging by SNPS. The 2D model consists of 240 source gathers (pressure recordings), a source waveform and complete velocity and density profiles. IFP used finite differences to generate the seismic data so elastic wave motion is approximated and some dispersion is present (Bourgeois et al., 1991). The underlying geological model represents a profile through the North Quenguela trough in the Cuanza basin of Angola (Bourgeois et al., 1991).

No preprocessing of the Marmousi data was done so the embedded source wavelet and multiples are present. The provided source waveform was used to construct the reference source wavefield during imaging. The velocity model was resampled from a four-meter sample spacing in x and z to 25 meters in x, the depth interval remains at four meters. A piecewise constant approximation to the velocity model was made by rounding each velocity to the nearest 100 m/s, resulting in approximately 10 to 20 unique velocities laterally in each depth step. No attempt was made to determine the optimal set of constant velocities.

Depth imaging of one source gather proceeds as follows:

1) Specify the reflected wavefield as the recorded source gather and pad it from 96 to 256 traces using zero amplitude traces (an example is given in Figure 3.3).

2) Specify the incident wavefield as the source waveform provided. Place the source waveform in a position corresponding to the source location within a gather of 256 zero amplitude traces.

3) Depth image with SNPS (Figure 3.2) using the piecewise constant velocity model. Restrict temporal frequencies to between 5 and 48 Hz.

Due to the limited recording aperture of a single source gather and the complexity of the model, a coherent image of the entire model is not possible from a single source. Figure 3.3 shows a source gather from location 5725m in the model. The resulting imaged gather is shown in Figure 3.4. Coherent reflectivity is only apparent in a narrow region corresponding to specular reflections, amplitude outside this region is noise. A complete image of the entire model is possible by imaging all of the source records, sorting the traces, muting noise and summing. Figure 3.5 shows one common image point (CIP) from location 6500 m in the model. Reflection energy on a CIP gather forms a continuous zone of coherency, as indicated by the annotated lines; data outside of this region are rejected. The resulting summed traces (Figure 3.6) give reflectivity in depth but they represent an average reflectivity over the range of source-receiver offsets in each CIP. For comparison, a bandlimited, zero-offset reflectivity section was computed from the p-wave velocities and densities (Figure 3.7).

All of the major seismic markers are present in the migrated image including three normal growth faults and the target sands. The top and bottom of the sands are resolved but the internal bedding is possibly beyond the resolution of the data. Elsewhere many of the steeply dipping folds have been imaged.

3.4 CHAPTER SUMMARY

A commonly used phase-shift method that approximates wave motion through media with lateral variation in velocity (PSPI) is a nonstationary filter in the limit of continuous lateral velocity variation. An alternative to PSPI, nonstationary phase shift (NSPS), exists by similar intuition and nonstationary filter theory. PSPI and NSPS were shown to be, respectively, the standard and adjoint standard forms of pseudo differential operators, whose symbols are the nonstationary phase-shift extrapolator.

The PSPI and NSPS phase-shift extrapolators can be coupled to obtain a composite extrapolator, called SNPS, which is symmetric in the (x,ω) domain. Symmetry is a desirable property (from reciprocity considerations) and is more stable (see Chapters 5 and 6). Prestack depth imaging of common-source gathers was implemented using the SNPS extrapolator. Reflectivity estimates for each depth were formulated as the ratio of downward extrapolated receiver and source wavefields. This ratio was done independently for each temporal frequency and averaged over all frequencies. A practical implementation of the NSPS, PSPI and SNPS extrapolators was done under the assumption that velocity is piecewise constant. In this case, the extrapolated wavefields are constructed from the basic operators of constant velocity

phase shift for each relevant velocity and appropriate spatial windowing. This implementation extends easily to 3D.

The Marmousi synthetic data set was used to demonstrate the viability of these results. Using a piecewise constant approximation to the exact Marmousi velocities, a high-resolution image was obtained.

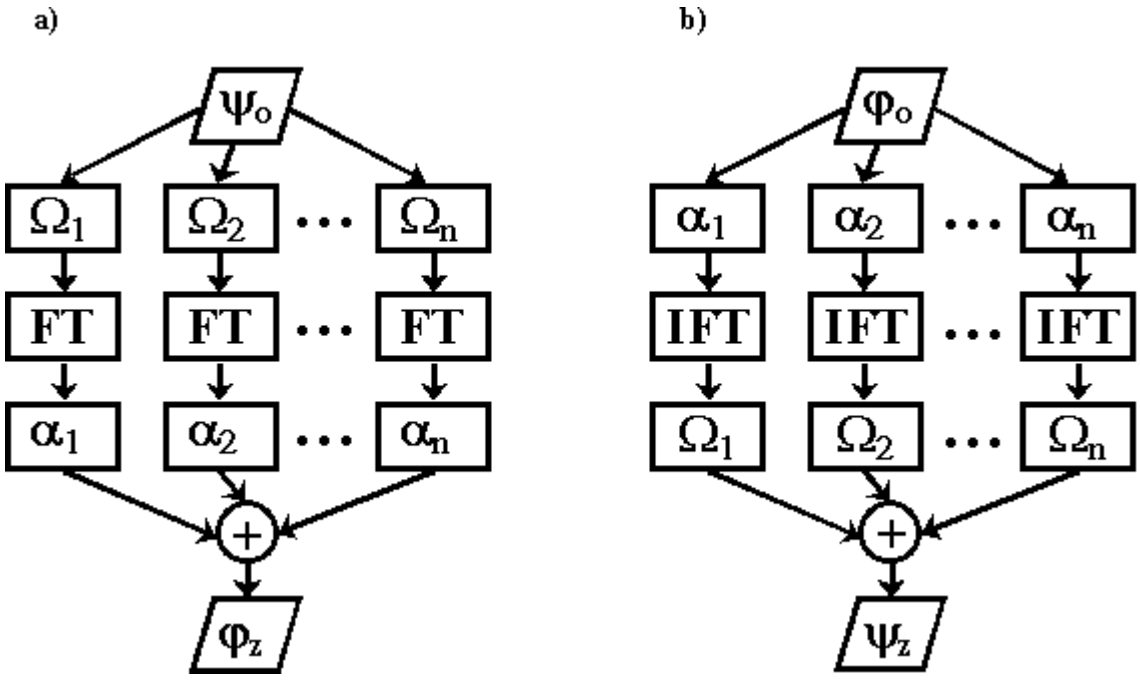

Fig. 3.1. Flow charts of wavefield extrapolation by NSPS (a) and PSPI (b). The windows Ω_j and phase shifts α_j correspond to piecewise constant velocities v_j. NSPS applies Ω_j to wavefield ψ_0 prior to Fourier transforming (FT) and phase shifting. The resulting spectra are summed to form the output spectrum φ_z. PSPI applies Ω_j to φ_0 after phase shifting and inverse Fourier transforming (IFT). The resulting wavefields are summed to form the output wavefield ψ_z. Both processes change spatial domain simultaneous with phase shifting, NSPS goes from x to k_x, while PSPI goes from k_x to x.

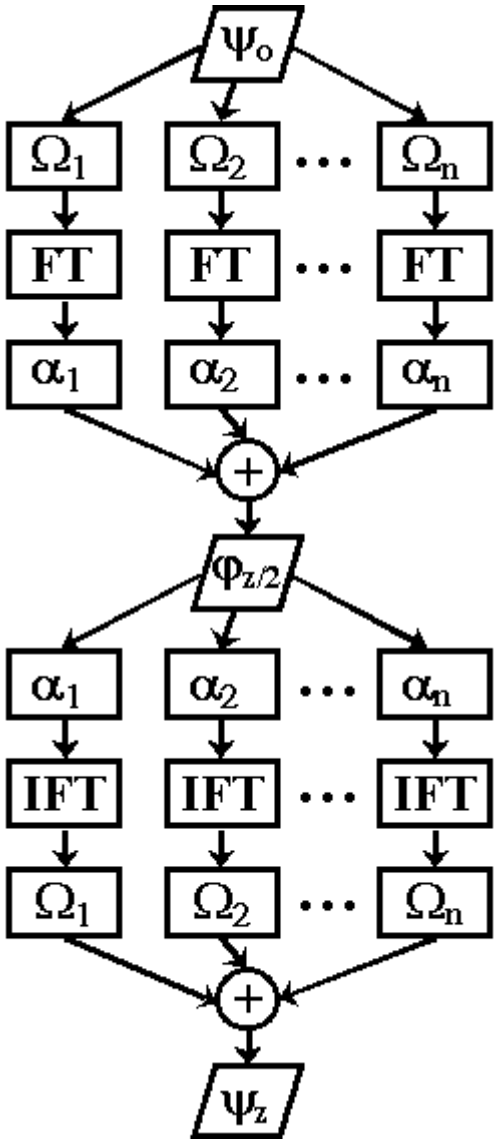

Fig. 3.2. Flow chart of wavefield extrapolation by SNPS. Windows Ω_j and phase shifts α_j correspond to piecewise constant velocities v_j. Phase shift of wavefield ψ_0 to ψ_z proceeds with a *z*/2 step by NSPS (see description in Figure 3.1a) followed by a *z*/2 step by PSPI (see description in Figure 3.1b). SNPS can just as easily be formulated beginning with PSPI and ending with NSPS at the cost of two extra IFTs over k_x.

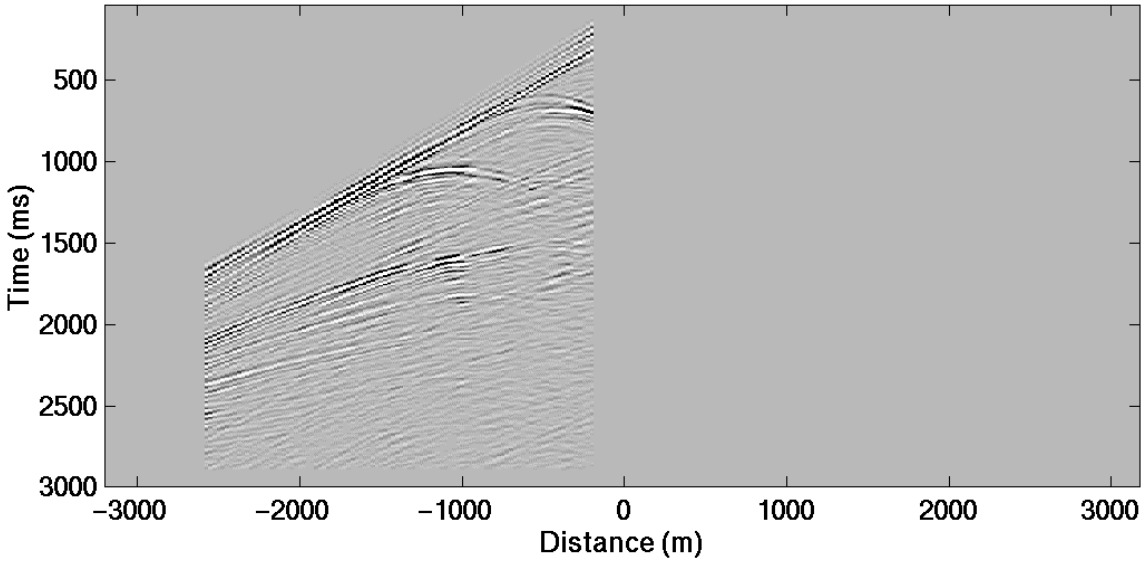

Fig. 3.3. A gather of common-source traces (source gather). The position of the source is at 5475 meters within the model.

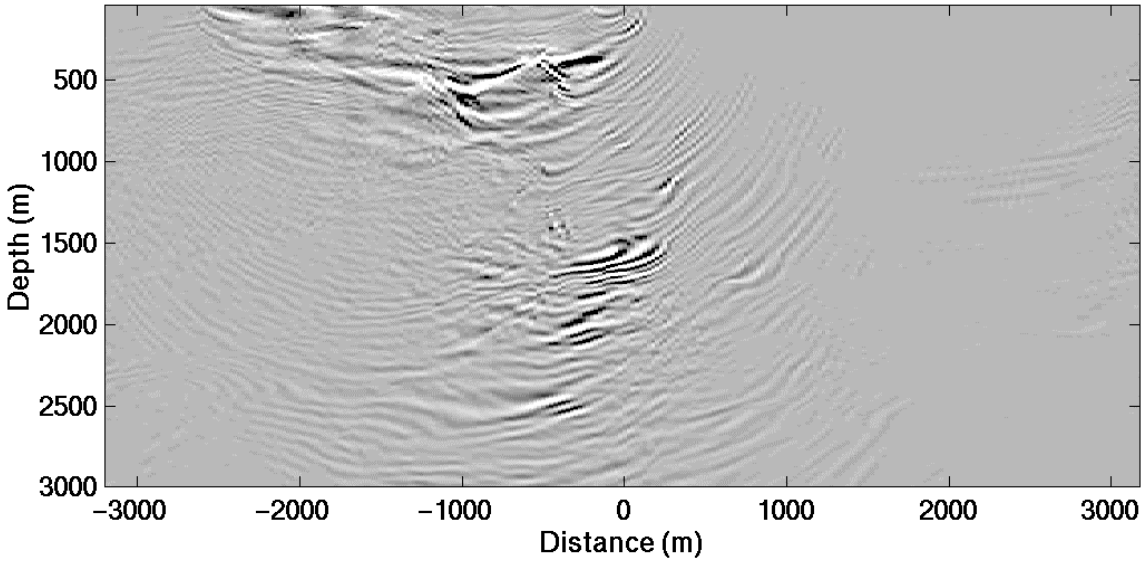

Fig. 3.4. Migrated image of the source gather of Figure 3.3. Coherent reflectivity corresponds to a narrow range of specular reflections due to the limited recording aperture (Figure 3.3). It is desirable to construct a complete image using a large number of overlapping images (Figure 3.6).

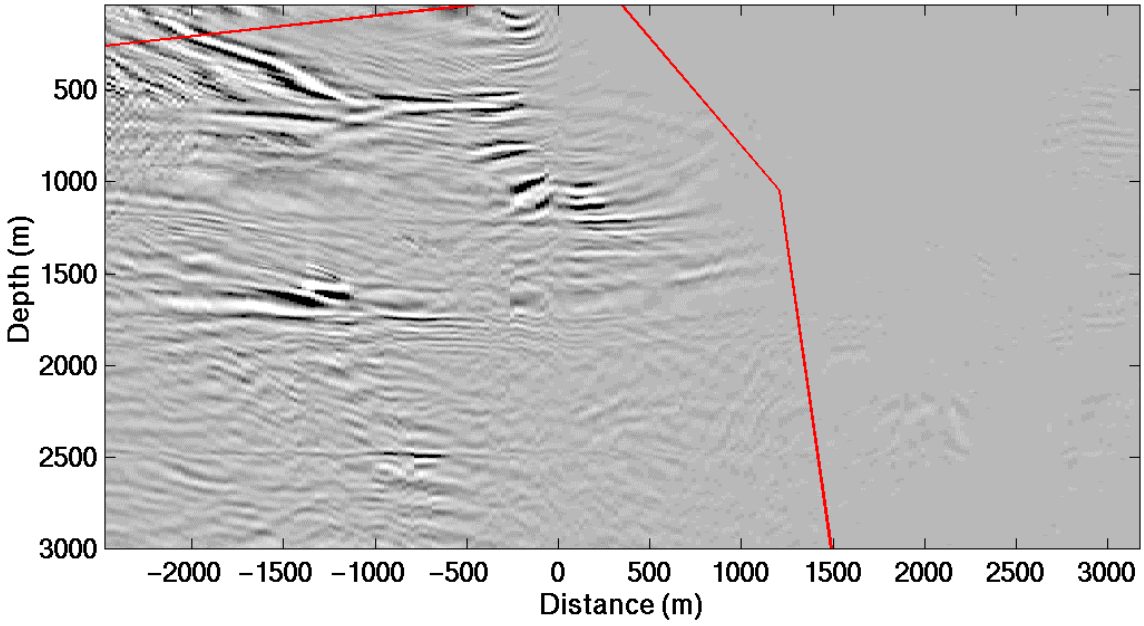

Fig. 3.5. A common-image-point (CIP) gather corresponding to location 6500 m in Figure 3.6. Amplitudes between the mute lines (annotated) are summed to give a single trace.

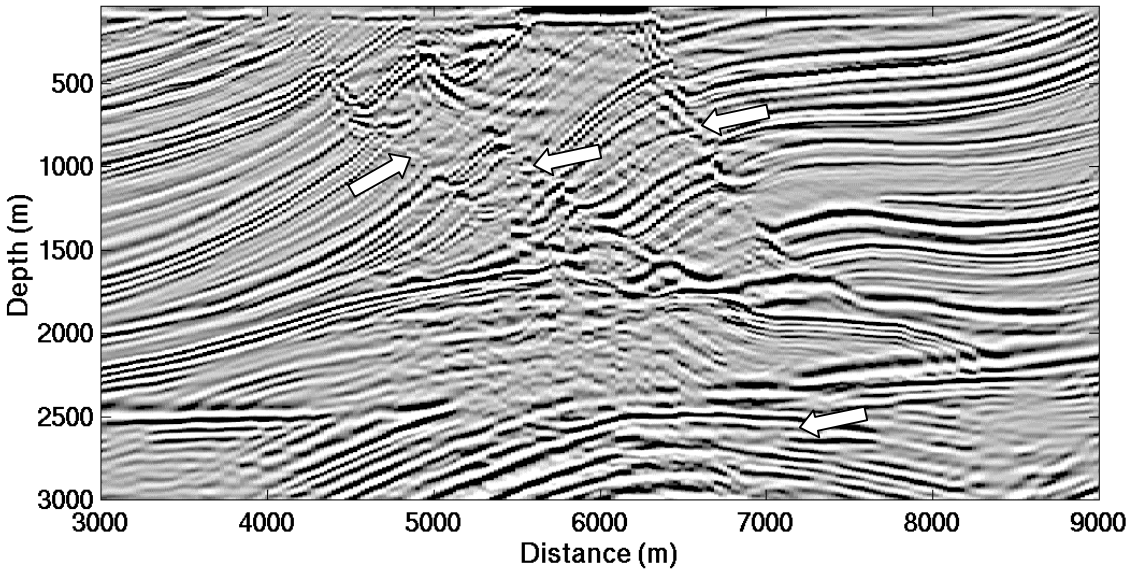

Fig. 3.6. Depth image from nonstationary migration. (The CIP gather in Figure 3.5 is muted and summed to give the trace at distance 6500 m.) Each amplitude represents a mixed reflectivity due to stacking the CIPs. Kinematically, this figure compares favorably with the zero offset reflectivity computed from velocity and density in Figure 3.7. Three faults are indicated towards the top of the section with arrows. The target sand is similarly indicated towards the bottom of the section.

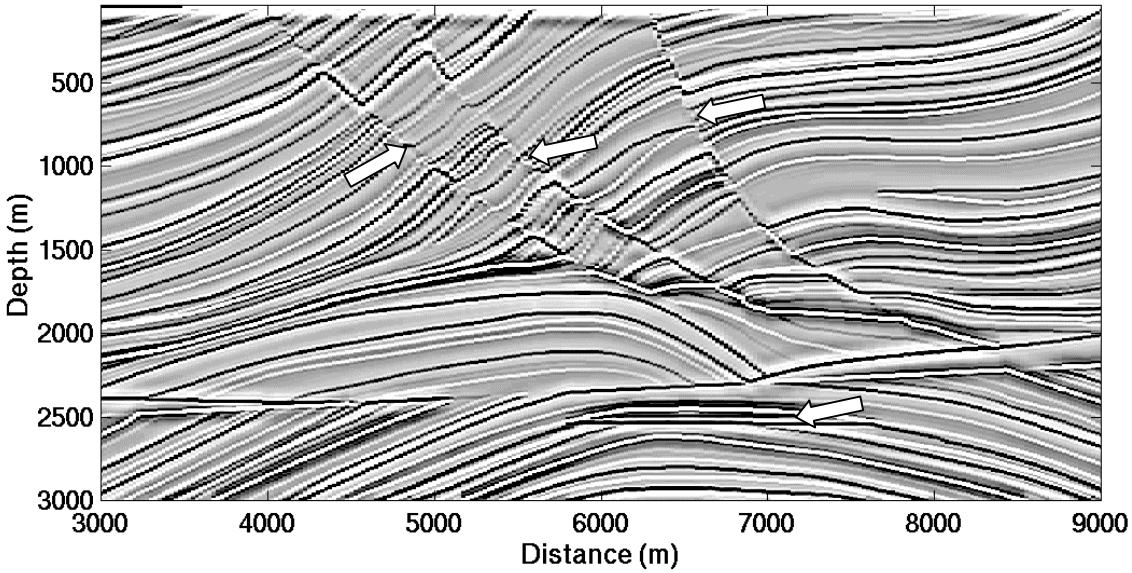

Fig. 3.7. Reflectivity computed from the model velocity and density. The amplitude of each point represents zero offset reflectivity. The same three faults are indicated here, as in Figure 3.7, towards the top of the section with arrows. The target sand is similarly indicated towards the bottom of the section.

CHAPTER 4

PRESTACK DEPTH MIGRATION IN ANISOTROPIC MEDIA BY SYMMETRIC NONSTATIONARY PHASE SHIFT

4.0 INTRODUCTION

In seismic imaging, much effort is spent on estimating the elastic parameters (P- and S-wave velocities) of an assumed isotropic subsurface for the construction of seismic images. Thomsen (1986) points out the inconsistency of these efforts when the subsurface is potentially anisotropic. Martin et al. (1992) demonstrate that isotropic algorithms applied to physical modeling data in transversely isotropic (TI) media produce mispositioning of plane reflectors and steep structures. Isaac and Lawton (1999) show that a TI medium having a symmetry axis of 45 degrees (measured from vertical) causes large errors in the lateral position of a simulated reef edge; enough error that an exploratory well would be significantly mispositioned.

Authors that have presented depth-imaging methods for TI media include Meadows et al. (1987) who extend the imaging method of Stolt (1978) to homogeneous

media with elliptical anisotropy. Uren et al. (1990) present a 2-D poststack Stolt method for homogeneous TI and Gonzalez et al. (1991) use an approximate anelliptic dispersion relation to implement a prestack Stolt method for P-waves in a homogeneous TI medium. Sena and Toksoz (1993) present a 2-D Kirchhoff algorithm (prestack) for weak TI (Thomsen, 1986). Uzcategui (1995) uses explicit depth extrapolators for TI media having a vertical axis of symmetry. Meadows and Abriel (1994) present a 3-D poststack phase-shift time algorithm for a homogeneous TI media to improve the image of data from the Gulf of Mexico. Kitchenside (1992) proposes a 2-D algorithm for homogeneous TI media that builds an extrapolator in the Fourier domain (k_x, ω) and applies it as a truncated and tapered filter in the space-frequency (x, ω) *domain.* Ferguson and Margrave (1998a) present a depth imaging method for heterogeneous TI media that is restricted to coincident source-receiver acquisition geometry.

Most of the above depth-imaging approaches restrict TI in the medium. Meadows and Abriel (1994), Kitchenside (1992) and Gonzalez et al. (1991) assume homogeneous TI. Meadows et al. (1987) assume eliptical TI. Sena and Toksoz (1993) assume weak TI and Uzcategui (1995) assumes TI with a vertical axis of symmetry. Ferguson and Margrave (1998a) do not restrict TI in the medium, but restrict the acquisition geometry of the seismic data to coincident source and receiver. No such restrictions are required for the depth imaging method presented here.

Kitchenside (1992) is followed in the initial development of the TI algorithm, but rather than applying a truncated filter in (x, ω), the complete filter is applied in (k_x, ω).

The resulting homogeneous phase-shift allows variation of velocity in the Fourier coordinates (k_x, ω) and depth z. Generalization to heterogeneous TI is achieved using nonstationary filters. Implementation as a depth-imaging algorithm is done using the symmetric nonstationary filter approach first introduced by Ferguson and Margrave (1999) and further described in Chapter 3.

A difficulty in imaging TI media is discussed by Tsvankin (1997). For a TI medium with a dipping axis of TI symmetry, some phases of the propagating wavefield travel upwards. Here, analogous to Hale et al. (1992), down going phases and upgoing phases are isolated and propagated separately. The combination of the resulting spectra approximates the exact result. The residual error is due to extrapolating the upgoing phases with a portion of the downgoing phases.

Two examples of depth imaging by SNPS in TI media are presented. The SNPS images are compared to isotropic depth imaging and a method that assumes a vertical axis of TI symmetry. This demonstrates the utility of SNPS and its superiority over the other two imaging methods.

4.1 REVIEW OF TRANSVERSE ISOTROPY

Transverse isotropy is a material symmetry that allows a complete specification of the elastic properties of the material with five constants. In this section, the phase velocity of P-waves in TI media is derived from first principles. It is a collection of the work of a number of authors and is intended as a convenient reference. The derivation begins with

the most general stress-strain relationship, having 81 elastic constants and ends with the Thomsen (1986) phase velocity for P-waves.

The most general linear relationship between applied stress σ and material strain ε requires nine stresses σ_{ij}, 9 strains ε_{ij} and 81 elastic constants c_{ijkl}. Using the summation convention of repeated indices

$$\sigma_{ij} = c_{ijkl}\varepsilon_{kl}, \tag{4.1}$$

where indices (i, j, k, l) take on values of 1, 2 and 3. The symmetry of stresses $\sigma_{ij} = \sigma_{ji}$ and strains $\varepsilon_{ij} = \varepsilon_{ji}$ reduce the numbers of independent σ_{ij} and ε_{ij} to 6 (Love, 1927: 39, 79) and the number of independent c_{ijkl} to 36. The path independence of the energy required to strain a material reduce the number of independent c_{ijkl} to 21 (Love, 1927: 99). This last result implies $c_{ijkl} = c_{klij}$.

In contracted notation

$$\text{for } ij \text{ (or } kl\text{)}: 11 \to 1, 22 \to 2, 33 \to 3, 23/23 \to 4, 13/31 \to 5, 12/21 \to 6, \tag{4.2}$$

the stress-strain law is (with $c_{ijkl} \to C_{mn}$)

$$\begin{bmatrix}\sigma_1\\ \sigma_2\\ \sigma_3\\ \sigma_4\\ \sigma_5\\ \sigma_6\end{bmatrix} = \begin{bmatrix} C_{11} & C_{12} & C_{13} & C_{14} & C_{15} & C_{16} \\ & C_{22} & C_{23} & C_{24} & C_{25} & C_{26} \\ & & C_{33} & C_{34} & C_{35} & C_{36} \\ & \text{SYM} & & C_{44} & C_{45} & C_{46} \\ & & & & C_{55} & C_{56} \\ & & & & & C_{66} \end{bmatrix} \begin{bmatrix}\varepsilon_1\\ \varepsilon_2\\ \varepsilon_3\\ \varepsilon_4\\ \varepsilon_5\\ \varepsilon_6\end{bmatrix}. \qquad (4.3)$$

where the lower left triangular portion of the matrix C has been left blank to indicate the symmetry of C_{mn}. If, after a reflection about the plane $x_1 = 0$, $x_2 = 0$ (x_1 and x_2 are lateral coordinates and x_3 is vertical), the elastic constants are unchanged, the number of independent constants is reduced to 13 (Appendix 1), i.e. $C_{35} = C_{36} = C_{45} = C_{46} = C_{15} = C_{25} = C_{16} = C_{26} = 0$. The stress-strain law, equation (4.3), reduces to

$$\begin{bmatrix}\sigma_1\\ \sigma_2\\ \sigma_3\\ \sigma_4\\ \sigma_5\\ \sigma_6\end{bmatrix} = \begin{bmatrix} C_{11} & C_{12} & C_{13} & C_{14} & & \\ & C_{22} & C_{23} & C_{24} & \text{NULL} & \\ & & C_{33} & C_{34} & & \\ & \text{SYM} & & C_{44} & & \\ & & & & C_{55} & C_{56} \\ & & & & & C_{66} \end{bmatrix} \begin{bmatrix}\varepsilon_1\\ \varepsilon_2\\ \varepsilon_3\\ \varepsilon_4\\ \varepsilon_5\\ \varepsilon_6\end{bmatrix} \qquad (4.4)$$

and the material is referred to as monoclinic, with the x_3-axis contained by the symmetry plane. (Zero elements in the upper right of the triangle are left blank.) The normal to the symmetry plane can be thought of as making an angle $\theta = 0$ with the x_1-axis. Surprisingly, if the normal to a second symmetry plane makes an angle $\theta = \pi/c$ with the x_1-axis, where c is an irrational number, the material is symmetric for all θ (Appendix 2). Further, as shown by Love (1927: 152-155), the material has only 5 independent elastic constants (transverse isotropy). The stress-strain law for a TI medium is

$$\begin{bmatrix}\sigma_1\\ \sigma_2\\ \sigma_3\\ \sigma_4\\ \sigma_5\\ \sigma_6\end{bmatrix} = \begin{bmatrix} C_{11} & C_{12} & C_{13} & & & \\ & C_{11} & C_{13} & & \text{NULL} & \\ & & C_{33} & & & \\ \text{SYM} & & & C_{44} & & \\ & & & & C_{44} & \\ & & & & & C_{66}\end{bmatrix}\begin{bmatrix}\varepsilon_1\\ \varepsilon_2\\ \varepsilon_3\\ \varepsilon_4\\ \varepsilon_5\\ \varepsilon_6\end{bmatrix}, \tag{4.5}$$

where $C_{66} = \frac{1}{2}(C_{11} - C_{12})$.

The equation of motion can be developed (Appendix 3) by equating the stress gradient with the product of density and particle acceleration (Love, 1927: 84-85)

$$\rho \frac{\partial^2 u_i}{\partial t^2} = \frac{\partial}{\partial x_j}\sigma_{ij}, \tag{4.6}$$

or, replacing σ_{ij}

$$\rho \frac{\partial^2 u_i}{\partial t^2} = \frac{\partial}{\partial x_j} c_{ijkl} \frac{\partial u_k}{\partial x_l}, \tag{4.7}$$

where u_i are components of displacement in the subscripted directions, ρ is the density of the material and t is time and $c_{ijkl}\varepsilon_{kl} = c_{ijkl}\partial u_k / \partial x_l$ is used. A plane wave solution to the wave equation may be written as (Daley and Hron, 1977)

$$u_i = U_i \exp(i\omega[t-\tau]) \ , \tag{4.8}$$

where U_i are amplitude components, ω is temporal frequency and phase function τ describes the travel time of the wavefront

$$\tau = \omega[\mathbf{x}\cdot\mathbf{k}], \tag{4.9}$$

where the spatial coordinates are $\mathbf{x} = (x_1, x_2, x_3)$, the wavenumbers are $\mathbf{k} = (k_1, k_2, k_3)$ and t is time. Substitution of the planewave (equation (4.8)) into the elastic-wave equation (4.7) gives

$$[\Gamma_{jk} - \lambda\delta_{jk}]U_j = 0\,, \tag{4.10}$$

where

$$\Gamma_{jk} = \frac{c_{ijkl}}{\rho}\frac{\partial\tau}{\partial x_l}\frac{\partial\tau}{\partial x_i} = \frac{c_{ijkl}}{\rho}p_i p_l\,, \tag{4.12}$$

and, assuming that U_i are not identically zero, the following eignvalue problem results

$$\det[\Gamma_{jk} - \lambda\delta_{jk}]U_j = 0\,. \tag{4.11}$$

The components of slowness $\mathbf{p} = (p_1, p_2, p_3)$ are

$$\frac{\partial \tau}{\partial x_1} = \frac{\cos\psi \sin\theta}{v(\psi,\theta)}$$
$$\frac{\partial \tau}{\partial x_2} = \frac{\sin\psi \sin\theta}{v(\psi,\theta)}, \qquad (4.13)$$
$$\frac{\partial \tau}{\partial x_3} = \frac{\cos\theta}{v(\psi,\theta)}$$

with angle θ measured from the x_3 axis and azimuth ψ as in Figure 4.1. Velocity $v(\psi,\theta)$ is the phase velocity of the wave type being considered.

Unfortunately, the determinant in equation (4.11) results in 6th order powers of $v(\psi,\theta)$ and a correspondingly unwieldy description. The solution is greatly simplified (Appendix 4) when wave propagation in the *y* coordinate is ignored i.e., $\psi = 0$. Three positive values of *v* result corresponding to quasi-P, quasi-SV and quasi-SH wavefront propagation (Daley and Hron, 1977). The equation for P-waves is

$$2\rho v_p^2 = C_{33} + C_{44} + (C_{11} - C_{33})\sin^2\theta + \sqrt{(C_{33} - C_{44})^2 + 2C_1 \sin^2\theta + C_2 \sin^4\theta}\,, \qquad (4.14)$$

where

$$C_1 = 2[C_{13} + C_{44}]^2 - [C_{33} - C_{44}][C_{11} + C_{33} - 2C_{44}] \qquad (4.15)$$

and

$$C_2 = [C_{11} + C_{33} - 2C_{44}]^2 - 4[C_{13} + C_{44}]^2 . \quad (4.16)$$

P-wave velocity in a TI medium is thus a function of 4 of the 5 independent elastic constants and phase angle θ. Thomsen (1986) presents a convenient rendering of P-wave velocity (as well as the qSV and qSH) in terms of parameters α_0, β_0, ε and δ^*. The first two correspond to P-wave (α_0) and S-wave (β_0) velocity measured parallel to the axis of TI symmetry. These four parameters are the following functions of the 4 elastic constants in equation (4.5)

$$\alpha_0 = \sqrt{\frac{C_{33}}{\rho}}, \beta_0 = \sqrt{\frac{C_{44}}{\rho}} \quad (4.17)$$

and

$$\varepsilon = \frac{C_{11} - C_{33}}{2C_{33}}, \delta^* = \frac{1}{2C_{33}^2}\left[2(C_{13} + C_{44})^2 - (C_{33} - C_{44})(C_{11} + C_{33} - 2C_{44})\right]. \quad (4.18)$$

The exact P-wave phase velocity in terms of the Thomsen (1986) parameters becomes

$$v_p^2 = \alpha_0^2\left[1 + \varepsilon \sin^2(\theta) + D^*(\theta)\right], \quad (4.19)$$

where,

$$D^*(\theta)=\frac{1}{2}\left[1-\beta_0^2/\alpha_0^2\right]$$
$$\left[-1+\sqrt{1+\frac{4\delta^*}{\left(1-\beta_0^2/\alpha_0^2\right)^2}\sin^2(\theta)\cos^2(\theta)+\frac{4\varepsilon\left(1-\beta_0^2/\alpha_0^2+\varepsilon\right)}{\left(1-\beta_0^2/\alpha_0^2\right)^2}\sin^4(\theta)}\right]. \quad (4.20)$$

In the next section, the equation (4.19) for P-wave phase velocity v_p, as a function of phase angle θ, is related to the coordinates of Fourier space for the propagation of wavefields.

4.2 STATIONARY PHASE SHIFT FOR TI MEDIA

Depth imaging in a homogeneous TI medium (the anisotropy is stationary in the lateral coordinates) is simple to develop from the stationary phase shift method of Gazdag (1978). As described in section **3.1**, the spectrum of the recorded seismic wavefield is recursively extrapolated downwards. At each depth level, as the wavefield moves down, an imaging condition is invoked that forms the output data. Generalization of this method from an isotropic to anisotropic media exploits the relationship of horizontal slowness to wavenumber k_x and temporal frequency (ω).

The phase shift extrapolator central to the Gazdag (1978) method is (equation 2.13 is repeated here in two spatial dimensions)

$$\psi(x,z)=\frac{1}{2\pi}\int\alpha(k_x)\varphi(k_x,0)\exp(-ixk_x)dk_x, \tag{4.21}$$

where the monochromatic (in temporal frequency ω) wavefield $\psi(z)$ is deduced from the k_x spectrum of $\varphi(z=0)$. Equation (4.21) carries spectrum φ to space coordinates as a product with *symbol* α. Symbol α in two dimensions is given by

$$\alpha(k_x)=\exp\left(iz\sqrt{\left(\frac{\omega}{v}\right)^2-k_x^2}\right). \tag{4.22}$$

Here, extrapolation is in the positive *z* direction and *v* is the velocity in the medium.

The velocity *v* in equation (4.22) is held constant in all lateral coordinates and variation of *v* with depth is enabled by recursive extrapolation. Thus, the medium must be homogeneous and isotropic in the lateral coordinate. The demand for isotropy can be relaxed, however, because the phase shift method does not restrict velocity to constant wavenumbers.

Similar to the method of Kitchenside (1992), the relationship between horizontal slowness and wavenumber and frequency

$$p=\frac{\sin(\theta)}{v(\theta)}=\frac{k_x}{\omega}, \tag{4.23}$$

is exploited where $v(\theta)$ is computed using equation (4.19). If the TI medium is dipping (i.e., the axis of TI symmetry is not vertical) equation (4.23) must be rotated by the angle between the axis of TI symmetry and vertical. In Figure 4.2 horizontal slowness *p* for

Weathered Gypsum is plotted against phase angle θ. A polynomial fit to this curve provides an empirical relationship between θ and *p*

$$\theta = a_0 + a_1 \frac{k_x}{\omega} + a_2 \left(\frac{k_x}{\omega} \right)^2 + \ldots + a_n \left(\frac{k_x}{\omega} \right)^n , \tag{4.24}$$

where a_i are the polynomial coefficients. (The appropriate value for *n* is determined by numerical experimentation.) At every (k_x, ω) in $\varphi(0)$ a phase angle θ is defined by equation (4.23) through the polynomial of equation (4.24) and the appropriate velocity is computed using equation (4.19). The phase shift symbol becomes

$$\alpha(k_x) = \exp\left(iz \sqrt{\left(\frac{\omega}{v(k_x/\omega)} \right) - k_x^2} \right), \tag{4.25}$$

where *v* is now no longer constant but a function of horizontal slowness k_x/ω.

A difficulty presents itself when the axis of symmetry ϕ of the medium is nonzero (Tsvankin, 1997), as can be seen in Figure 4.2. A range of k_x/ω, between the horizontal lines propagate only in the downward direction, but a smaller range between the horizontal lines on Figure 4.3 propagate simultaneously up and down. (The dashed part of the line indicates the upgoing part.) In a procedure similar to the turning wave migration of Hale et al. (1992) the purely downgoing phases, corresponding to the solid line in Figure 4.2, are separated from the upgoing phases and propagated. The upgoing phases, corresponding to the phases below the line on Figure 4.3, are then separated and propagated upward. However, only those phases corresponding to the dashed part of the

curve are upgoing. Error is introduced in the upgoing phases because phases corresponding to the solid part of the curve are also propagated upward.

Figure 4.4 shows the depth-migration impulse-response of phase shift (coincident source-receiver) in a homogeneous TI medium. The axis of symmetry is 45 degrees. The material simulated is the Weathered Gypsum described by Thomsen (1986) and the elastic parameters are annotated on Figure 4.4. The solid line represents a wavefront, or a line of constant time, computed by raytracing using group velocity (which is the velocity at which the wavefront propagates. Thomsen (1986) provides a formula for the derivation of this velocity from phase velocity and the resulting curve is only kinematically correct. The migration impulse response tracks the theoretical curve very well. On the left side, the impulse response exceeds 90 degrees, but the migration impulse response is able to track it (distortion beyond 90^{o} is due to the unavoidable up propagation of downgoing phases). The quality of the impulse response means that reliable imaging of structures, at least up to 90 degrees, is possible for a homogeneous TI medium. This is generalized to heterogeneous TI media in a later section.

4.3 ISOTROPIC REEF WITH AN ANISOTROPIC OVERBURDEN

As a test of the homogeneous TI method, seismic data from a physical model designed to simulate reef, were obtained from the Physical Modeling Facility at the University of Calgary, courtesy of the Foothills Research Project. The physical model consists of a block of Phenolic material with orthorhombic anisotropy (for a description of orthorhombic symmetry see Ting, 1996: 45) overlying a block of Plexiglas that is

isotropic. The overburden was oriented such that it responded to a 2-D acquisition as a TI medium. A step cut into the Plexiglas represents an imaging target such as a reef edge. Figure 4.5 shows the geometry of the model scaled (1000:1) into units of meters. The anisotropic parameters are labeled in Figure 4.5.

The resulting constant offset seismic data scaled into units of seconds and meters is shown in Figure 4.6. The offset between the source and receiver transducers is 200m in the scaled units. Imaging the constant offset data by TI phase shift provides an accurate picture of the model, as in Figure 4.7, where the imaged reef tracks the true reef given by a dashed line and the top of the isotropic material is correctly located. Figures 4.8 and 4.9 are included to illustrate the error of using an isotropic imaging method (Figure 4.8) or an imaging method that assumes a vertical axis of TI symmetry (VTI) (Figure 4.9). In both figures, reflectors are imaged approximately 60m to shallow and the reef edge is positioned approximately 400m to the left of the true position. The only difference between the isotropic and VTI images is found in their diffraction responses (at the top and bottom edges of the reef).

4.4 SYMMETRIC NONSTATIONARY PHASE SHIFT FOR TI MEDIA

Symmetric nonstationary phase shift (Margrave and Ferguson, 1999b) uses nonstationary filter theory (Margrave, 1998) to remove the requirement that velocity remain constant in the lateral coordinate. The resulting symmetric operator is more accurate and more stable than other explicit wavefield extrapolators (Chapter 5; Chapter 6; Margrave and Ferguson, 1999b). In two dimensions SNPS (equation 2.27) is written as

$$\psi(x,z) = \int \psi(y,0) \frac{1}{2\pi} \int \alpha\left(x, k_x, \frac{z}{2}\right) \alpha\left(y, k_x, \frac{z}{2}\right) \exp(-ik_x[x-y]) dk_x dy\,, \quad (4.26)$$

where the product of symbols $\alpha(x)$ and $\alpha(y)$ is

$$\alpha\left(x, k_x, \frac{z}{2}\right) \alpha\left(x, k_x, \frac{z}{2}\right) = \exp\left(\frac{iz}{2}\sqrt{\left(\frac{\omega}{v(x)}\right)^2 - k_x^2} + \frac{iz}{2}\sqrt{\left(\frac{\omega}{v(y)}\right)^2 - k_x^2}\right). \quad (4.27)$$

Lateral coordinates at $z = 0$ (input) are represented by y and output coordinates at $z = 0$ are represented by x. (The equivalent linear operator in equation (4.26) is symmetric under an exchange of coordinates x and y as shown in Chapter 2.) Using the same polynomial fitting procedure as in the homogeneous TI case, except that a polynomial is created at every x and y location, the product of symbols $\alpha(x)$ and $\alpha(y)$ (equation (4.27)) for heterogeneous TI is

$$\alpha\left(x, k_x, \frac{z}{2}\right) \alpha\left(x, k_x, \frac{z}{2}\right) = \exp\left(\frac{iz}{2}\sqrt{\left(\frac{\omega}{v(x, \omega/k_x)}\right)^2 - k_x^2} + \frac{iz}{2}\sqrt{\left(\frac{\omega}{v(y, \omega/k_x)}\right)^2 - k_x^2}\right).$$

(4.28)

In Chapter 3, an efficient implementation of equation (4.28) for isotropic media was presented based on Ferguson and Margrave (1999). The symmetric extrapolator is broken into two steps and each step proceeds as a set of stationary phase shifts corresponding to a velocity profile that is piecewise continuous laterally. The extension to TI simply requires replacement of the isotropic extrapolator (equation (3.11)) with the

anisotropic one of equation (4.25). Then, instead of just P-wave velocity, all four anisotropic parameters $\alpha_0, \beta_0, \varepsilon$ and δ^* are made piecewise continuous laterally.

Figures 4.12 and 4.14 are impulse responses for poststack migration by symmetric nonstationary phase shift for two different geological scenarios. Figure 4.12 is the impulse response for poststack migration through the velocity structure of Figure 4.11. The input to the experiment is given in Figure 4.10. The velocity structure of Figure 4.11 has Weathered Gypsum on the left side (with a 45 degree axis of symmetry) and a similar but isotropic material on the right. Figure 4.12 clearly shows the difference between wave propagation through an isotropic verses and anisotropic medium. The TI impulse response is skewed down and to the right while the isotropic curve is symmetric. In Figure 4.14, the impulse on the left has first propagated through an isotropic medium to a depth of 400m where it entered a TI medium (Figure 4.13). The resulting impulse response is symmetric from 0 to 400m and non-symmetric from 400m to 800m. The reverse is true for the right side. The impulse began in a TI medium and entered and isotropic medium at 400m (Figure 4.13) and is then non-symmetric from 0 to 400m and symmetric from 400m to 800m.

4.5 ANISOTROPIC THRUST SHEET MODEL

A second physical model is that of a flat reflector overlain by a TI thrust sheet embedded in an isotropic background. It represents a true anisotropic/nonstationary problem (the anisotropic parameters vary in the lateral coordinate). The thrust sheet is

composed of four blocks (Figure 4.15) – each with a different axis of TI symmetry. The base of the model consists of a flat aluminum plate that provides a strong reflection.

A single source gather is given in Figure 4.16 and spans the first 4000m of the model with the source location at 2040m. The major reflection at the bottom of the gather corresponds to a reflection from the aluminum plate. The apparent moveout of the reflection is continuous because its energy has propagated only through the isotropic material of the Plexiglas and the block of TI material with the vertical axis of symmetry. In contrast, to the right of the source location, reflected energy has propagated through all three of the TI blocks that have nonvertical axes of TI symmetry and the resulting apparent moveout on the reflection is discontinuous.

TI depth migration of the source gather (Figure 4.17), using SNPS, results in an image of the aluminum plate that is flat on both sides of the source. The lack of continuity below the source location is due to the 200m gap in the near offsets on the source gather (Figure 4.16). Isotropic depth migration resolves a poor image of the aluminum plate (Figure 4.18).

The image provided by assembling all of the TI migrated source gathers (Figure 4.19) provides a very good image of the reflector at the correct depth and the joints between the blocks are correctly positioned. Assembling all of the source gathers from isotropic migration into a single image provides a distorted picture (Figure 4.20). The joints between blocks have been imaged, but in the wrong places and the aluminum plate has a large artifact anticline formed directly below the dipping TI blocks.

4.6 CHAPTER SUMMARY

A new depth imaging method for dipping TI media was presented based on the symmetric nonstationary phase shift (SNPS) method of Ferguson and Margrave (1999). Their method is a cascade of two nonstationary extrapolators and is more accurate and more stable than other explicit-one-way extrapolators (Chapters 5 and 6, Margrave and Ferguson, 1999b). It was adapted for depth imaging in a TI medium. No restriction was placed on the strength of the anisotropy, its heterogeneity or its axis of symmetry. Depth imaging of two TI models (physical seismic data) by SNPS provided superior images to those from isotropic and VTI (vertical transverse isotropy) methods.

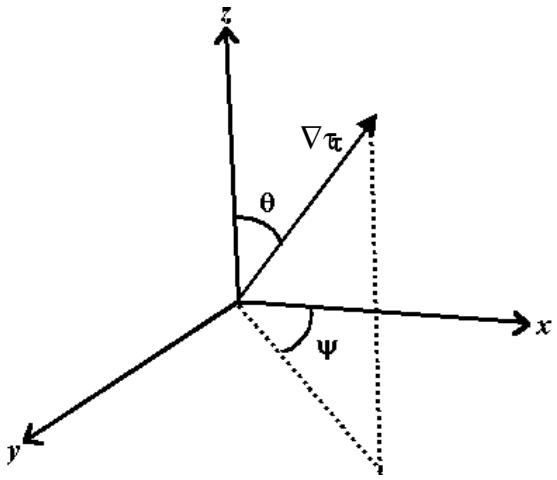

Fig. 4.1. Angle θ is the inclination of travel time $\nabla\tau$, normal to a planewave, from the *z* axis. The *z* axis is aligned with the TI axis of symmetry. Angle ψ is angle relative to the *x* axis.

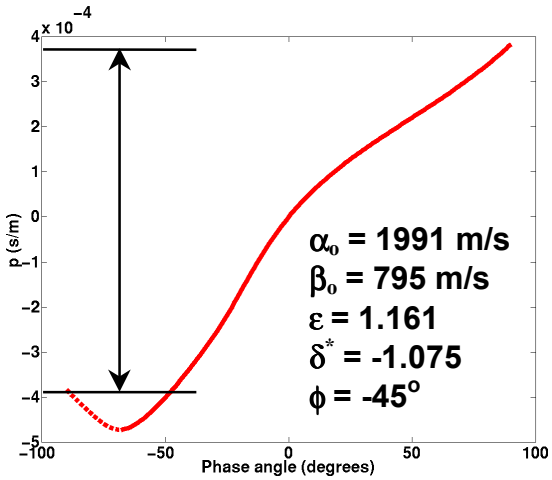

Fig. 4.2. Horizontal slowness p vs. phase angle θ for Weathered Gypsum. (The anisotropic parameters are annotated.) This material was chosen due to its extreme anisotropy. The range of $p = k_x/\omega$ between the solid lines are phases that are propagated down. The phases corresponding to the solid part of the curve out side of the lines are propagated simultaneously up and down. The down going phases are responsible for the coherent energy up to 90 degrees on Figure 4.4.

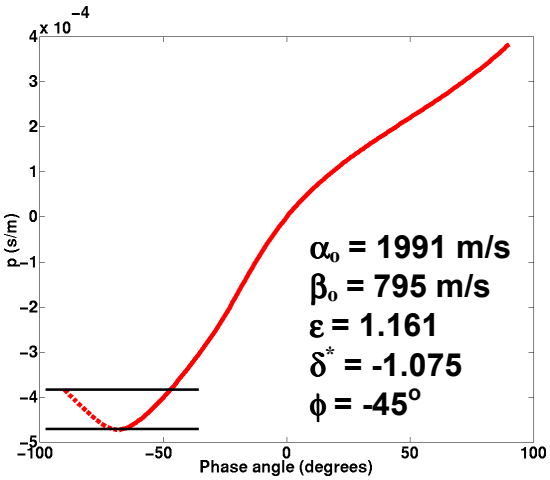

Fig. 4.3. Horizontal slowness *p* vs. phase angle θ for Weathered Gypsum. The phases corresponding to the dashed line are propagated up, however they cannot be separated from the downgoing phases corresponding to the solid part of the curve between the lines. These phases are propagated up as well. The result in the impulse response of Figure 4.4 is the ability to track the theoritical response, though only approximately, beyond 90 degrees.

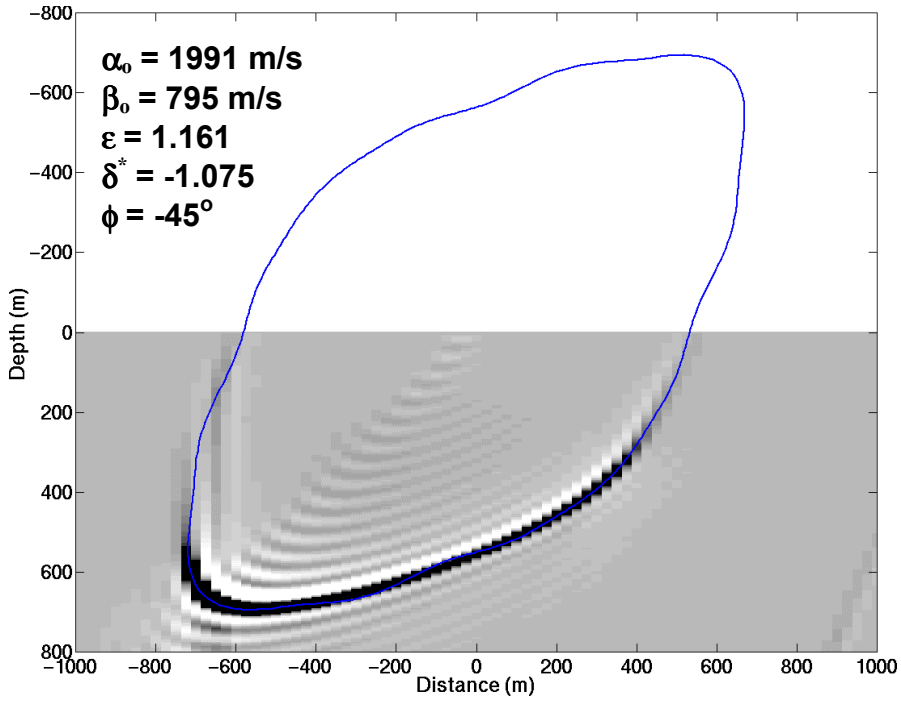

Fig. 4.4. The impulse response (equivalently a constant time curve) for phase shift in a homogeneous TI medium whose axis of symmetry is 45°. (This impulse corresponds to poststack depth imaging.) The continuous curve is the theoretical curve up to 90°. Beyond 90° the tracking is somewhat distorted due to the unavoidable propagation upwards of downgoing phases (see Figure 4.3).

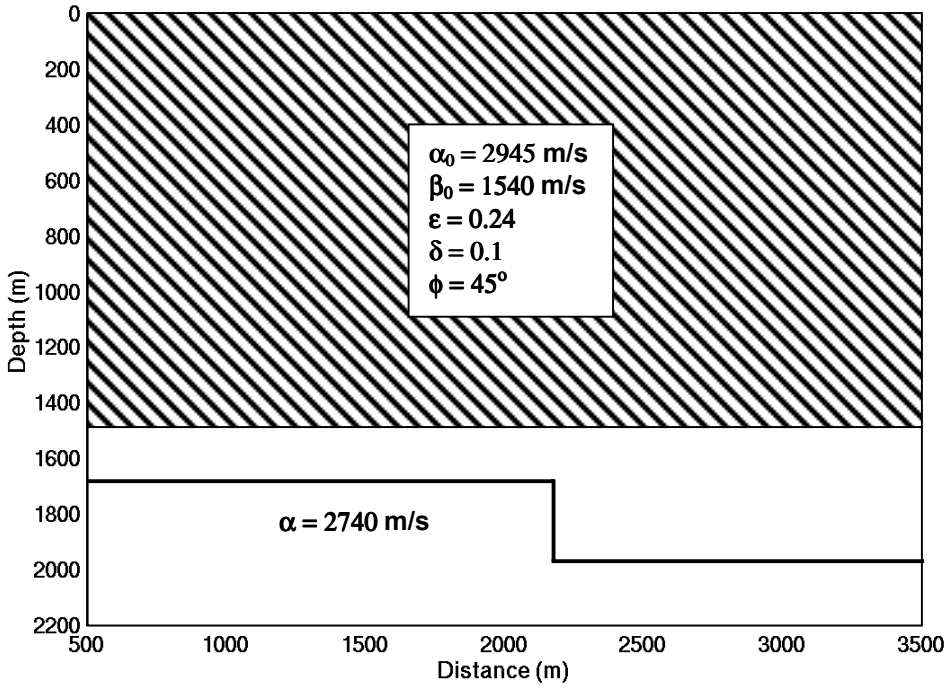

Fig. 4.5. Model of an isotropic reef with an anisotropic overburden. The dimensions and elastic parameters of the model are annotated. The axis of TI symmetry in the overburden is 45^o.

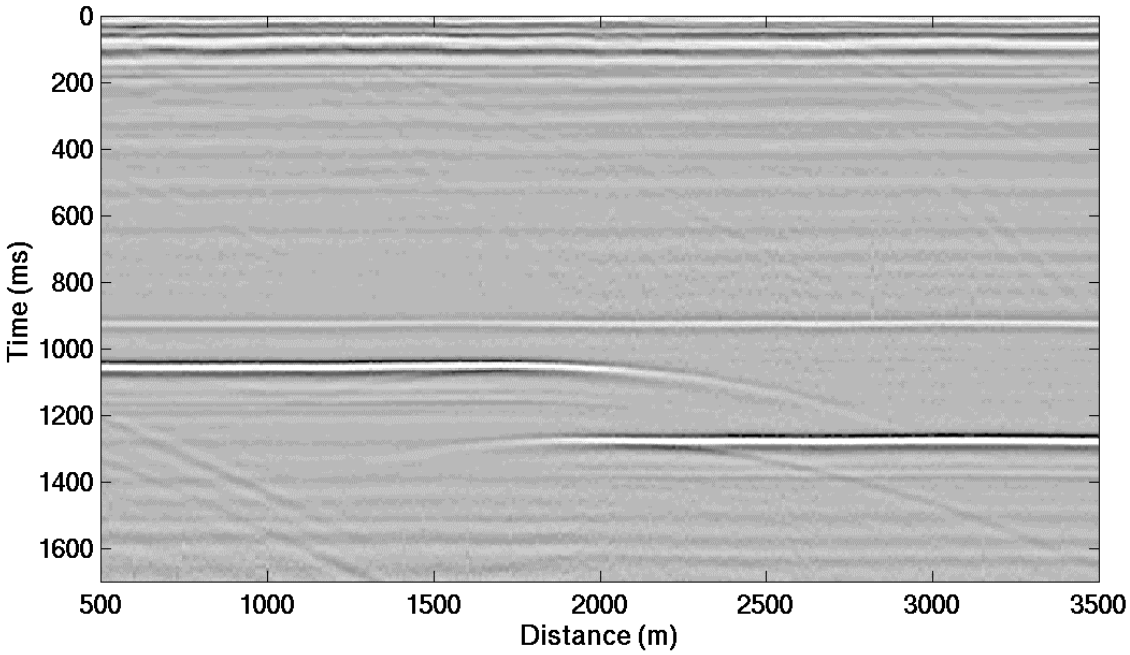

Fig. 4.6. Constant offset seismic data acquired from the model in Figure 4.5.

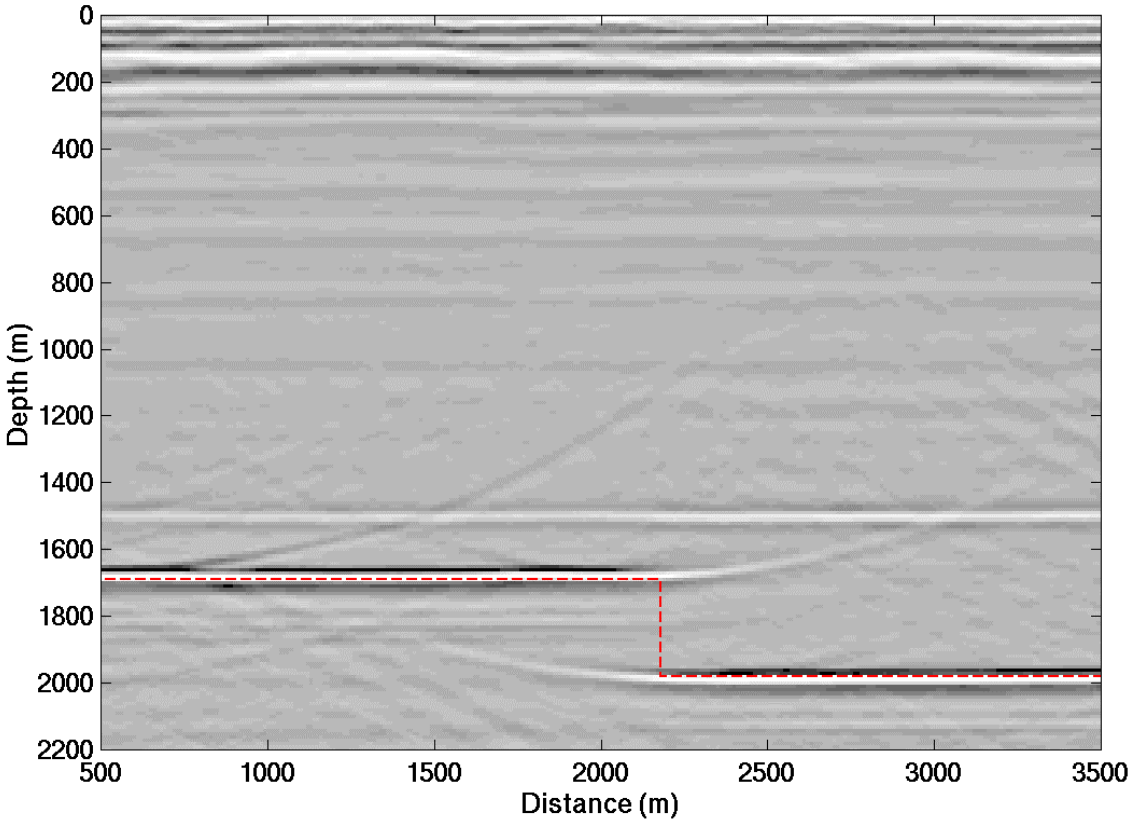

Fig. 4.7. Depth image of the constant offset data in Figure 4.6 using SNPS. The interface between the anisotropic overburden and the isotropic target zone is correctly positioned in depth (~1440m). The reef surfaces and reef edge have been correctly positioned in depth and lateral location (the true geometry of the reef is represented by the dashed line). The imaging artifacts visible at the reef edges are most probably due to the directivity of the source and receiver transducers.

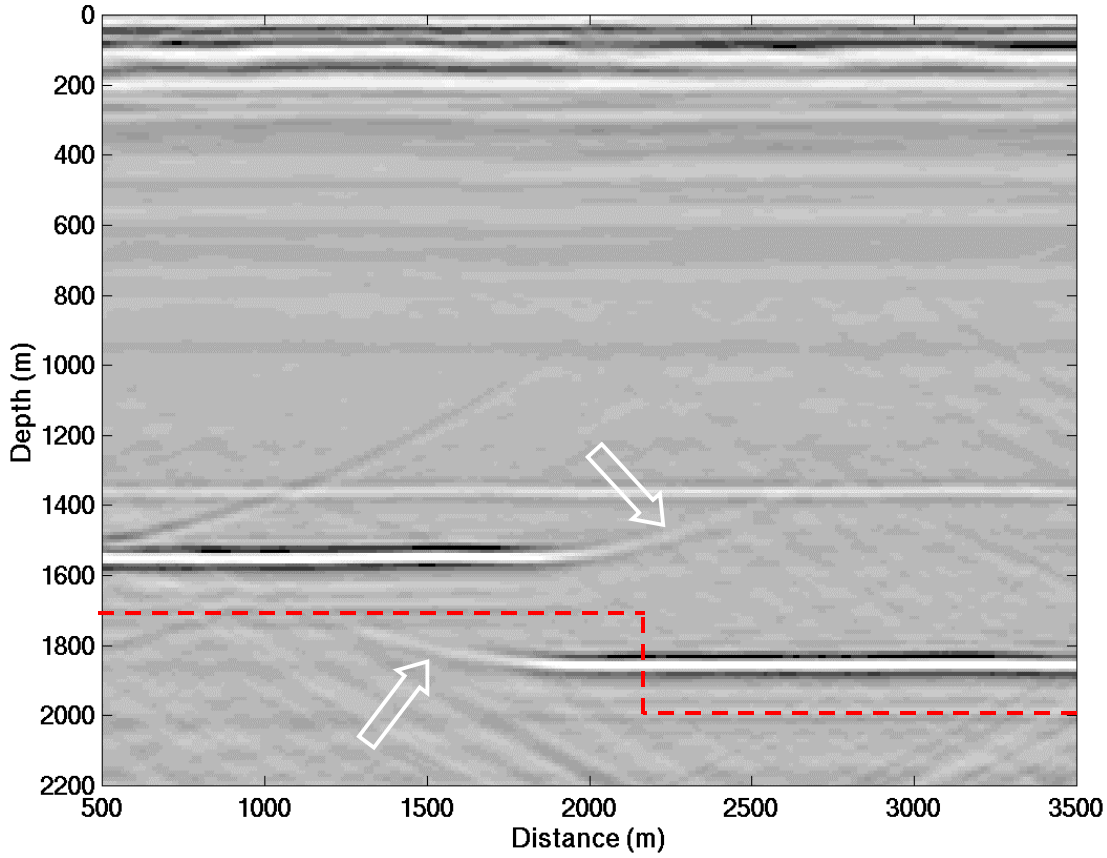

Fig. 4.8. Isotropic depth image of the constant offset data (Figure 4.6). Flat lying reflectors are positioned approximately 60m too shallow and the reef edge is shifted approximately 400m to the left. Diffractions from the top and bottom of the reef edges are annotated for comparison with Figure 4.9.

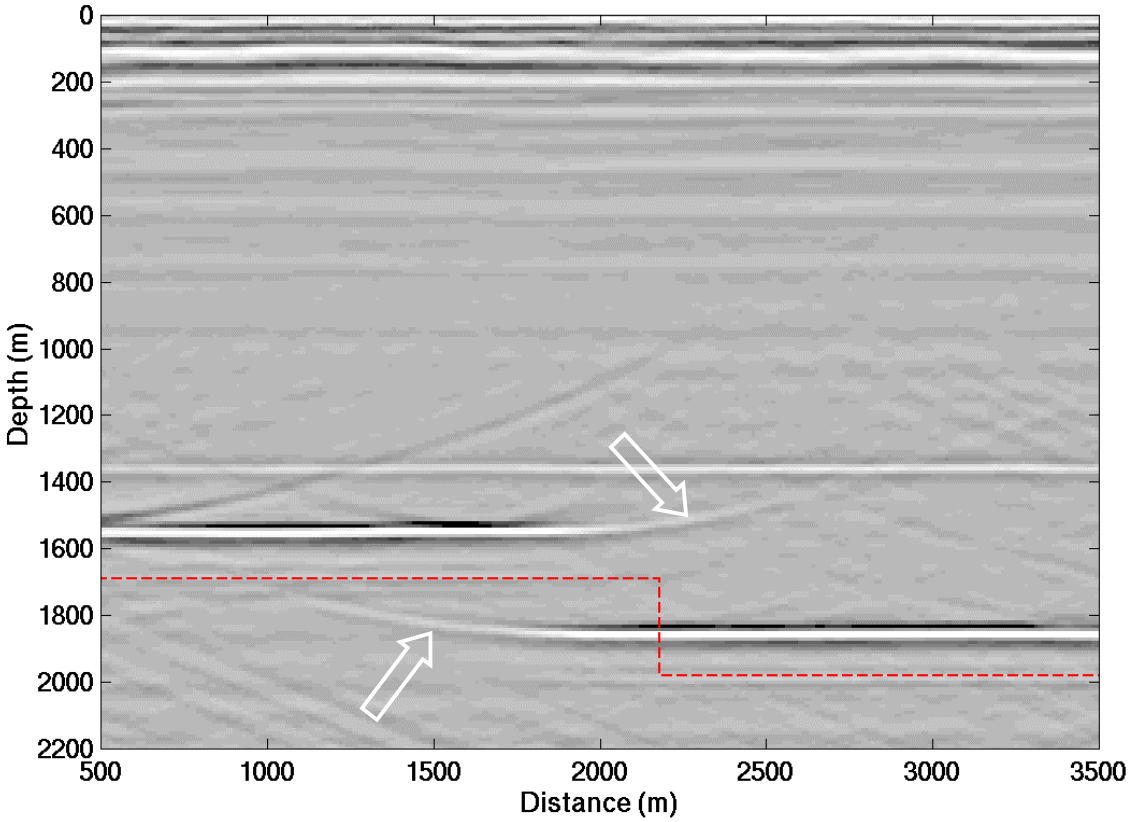

Fig. 4.9. Depth image of the constant offset data (Figure 4.6) assuming a vertical axis of TI symmetry (VTI). All flat lying reflectors are positioned approximately 60m too shallow in depth. The reef edge is positioned approximately 400m to the left of its true position. This image and the isotropic image above (Figure 4.8) differ significantly in their diffraction responses as seen at the reef edges (arrows), but nowhere else.

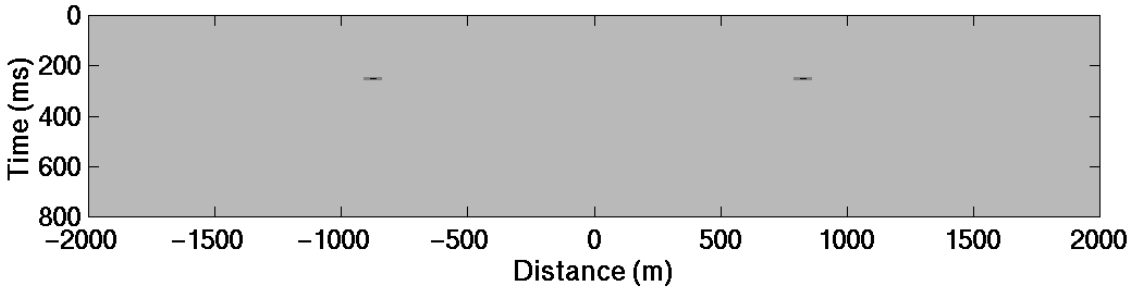

Fig. 4.10. Input impulses for depth imaging tests.

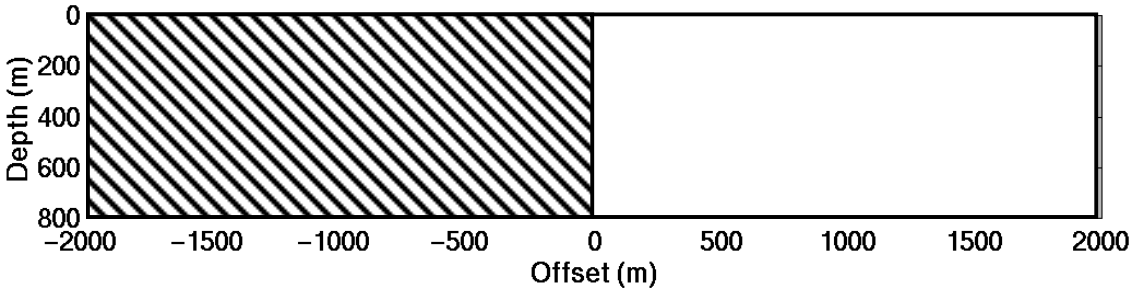

Fig. 4.11. Model of anisotropic Weathered Gypsum (see Figure 4.4 for the anisotropic parameters) welded laterally to isotropic Weathered Gypsum (ε and δ^* are zero). On the left, the axis of TI symmetry is 45^o.

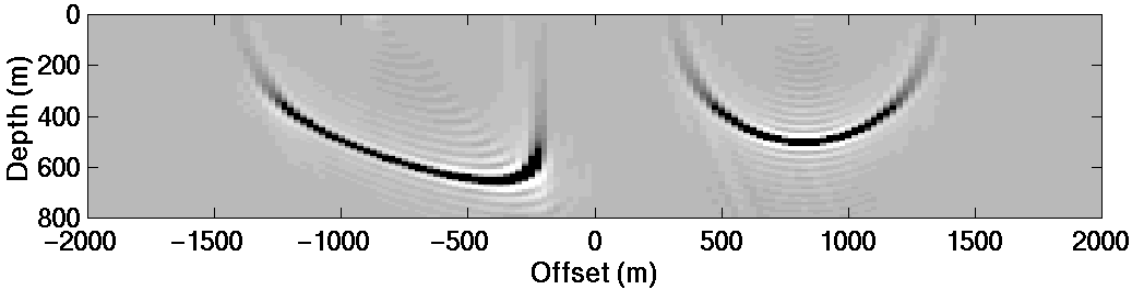

Fig. 4.12. Impulse response of SNPS for the model of Figure 4.11. The symmetry of the impulse response on the right side compared to the asymmetry of the left side demonstrates the ability of the method to migrate through heterogeneous TI media.

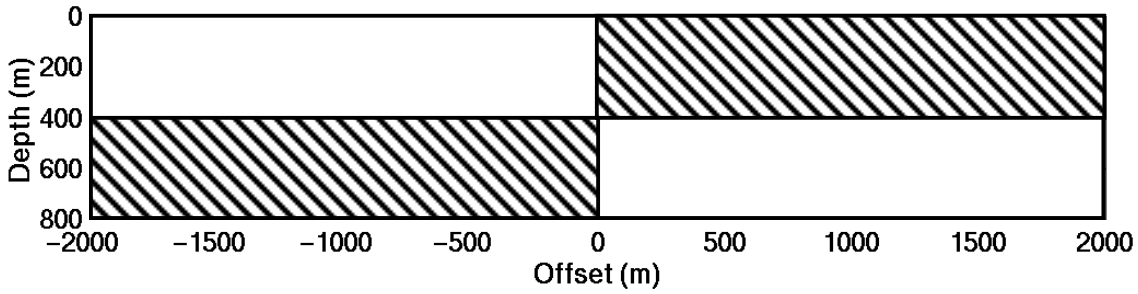

Fig. 4.13. Model of a heterogeneous TI medium where the quadrants of the model in Figure 4.11 have been swapped.

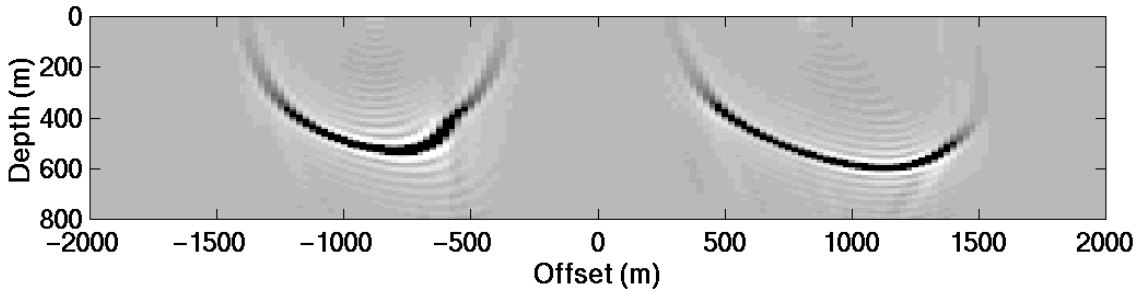

Fig. 4.14. Impulse response of SNPS for the model of Figure 4.13. The impulse response on the left side is symmetric until 400m where it encounters the dipping TI medium and becomes antisymmetric. The right side is anti symmetric until 400m where it encounters an isotropic medium and continues as a symmetric response.

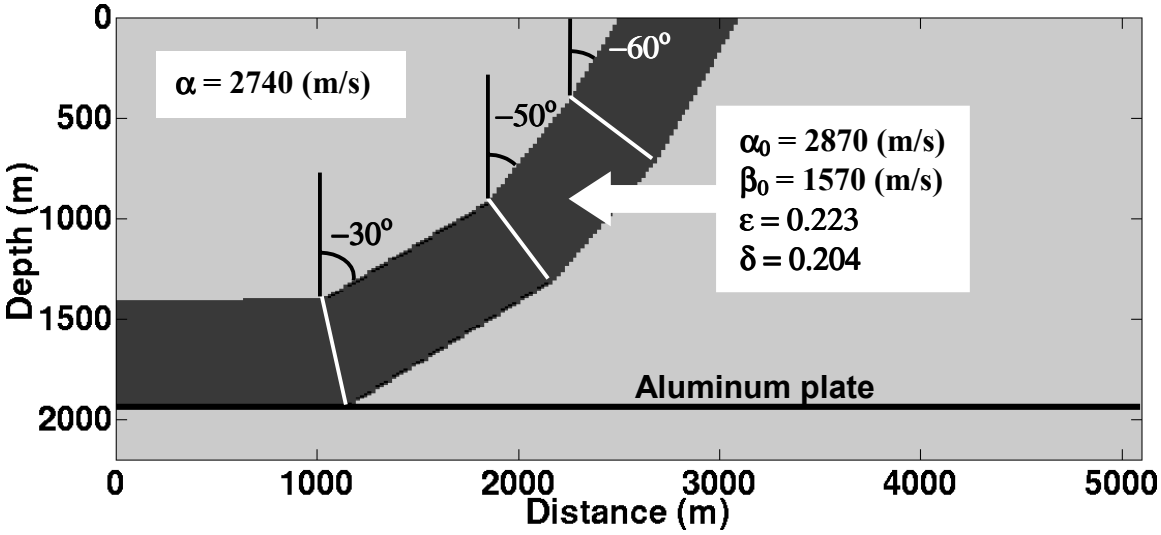

Fig. 4.15. Model of a TI thrust sheet embedded in an isotropic background. The thrust sheet is composed of four blocks of TI material with similar anisotropic parameters (annotated) but different axes of symmetry.

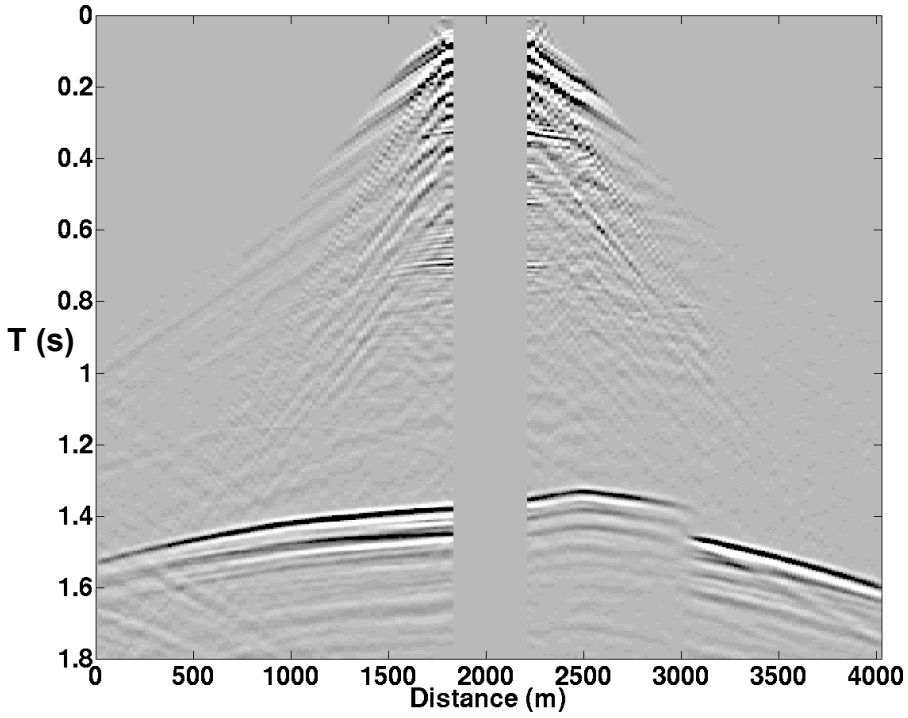

Fig. 4.16. Seismic source gather corresponding to source location 2040m in Figure 4.15. The major reflection at the bottom of the section corresponds to the base of the model. The apparent moveout of the reflection to the left of the source is continuous because most of the reflection energy propagated only through the isotropic material part of the model and the TI block with the vertical axis of symmetry. The reflection energy to the right of the source has propagated through the three blocks with nonvertical axes of TI symmetry and so appears discontinuous.

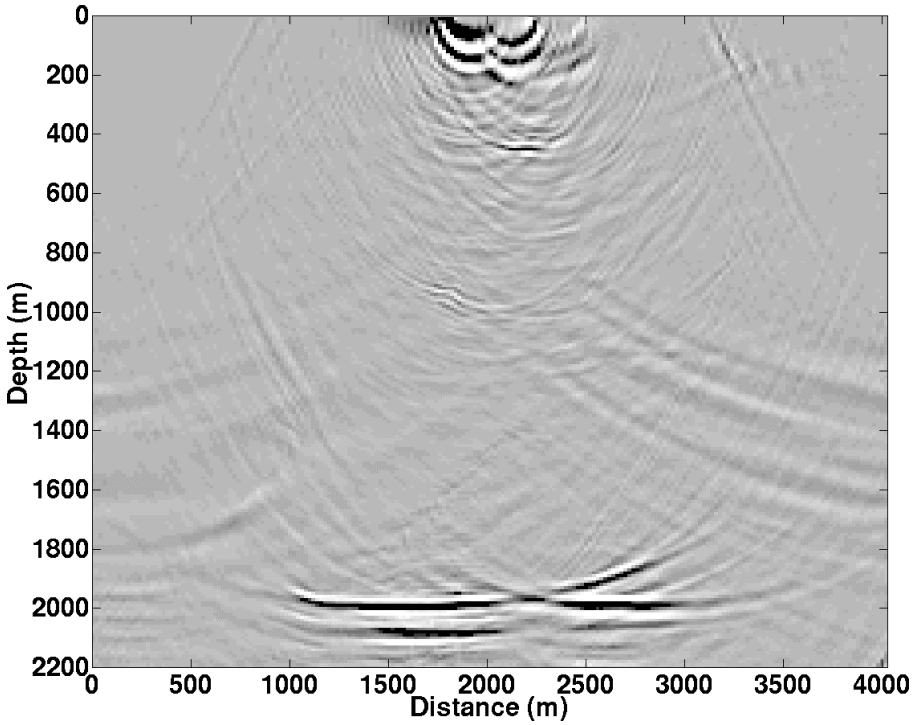

Fig. 4.17. TI depth image corresponding to the source gather in Figure 4.16 by SNPS. The base of the model is correctly imaged. The discontinuity of the image below the show point corresponds to the gap between the live traces centered on the source location (Figure 4.16).

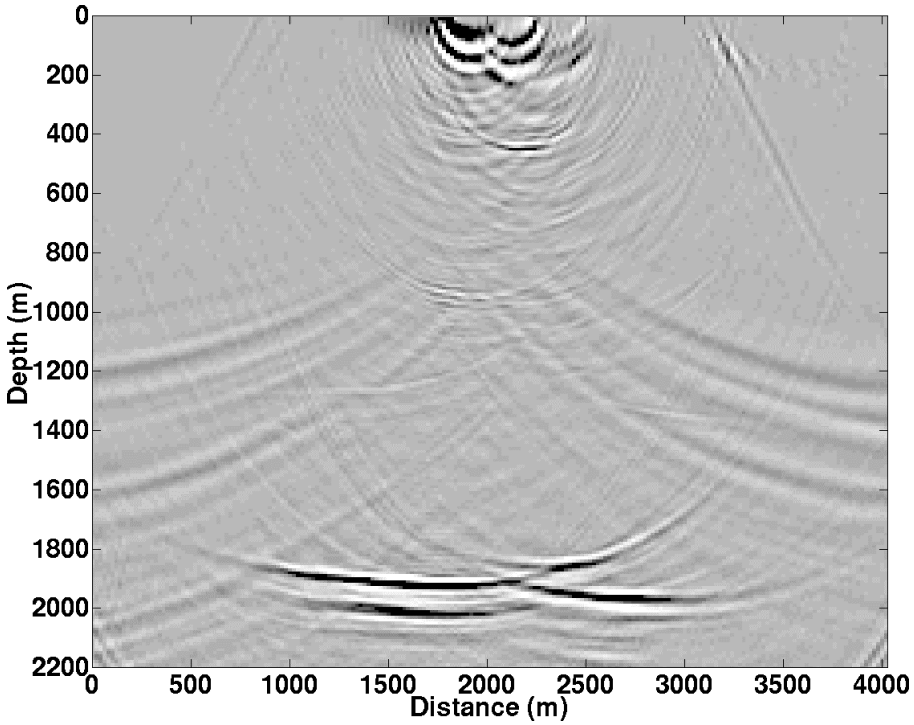

Fig. 4.18. Isotropic depth image corresponding to the source gather in Figure 4.16. The base of the model has been poorly imaged.

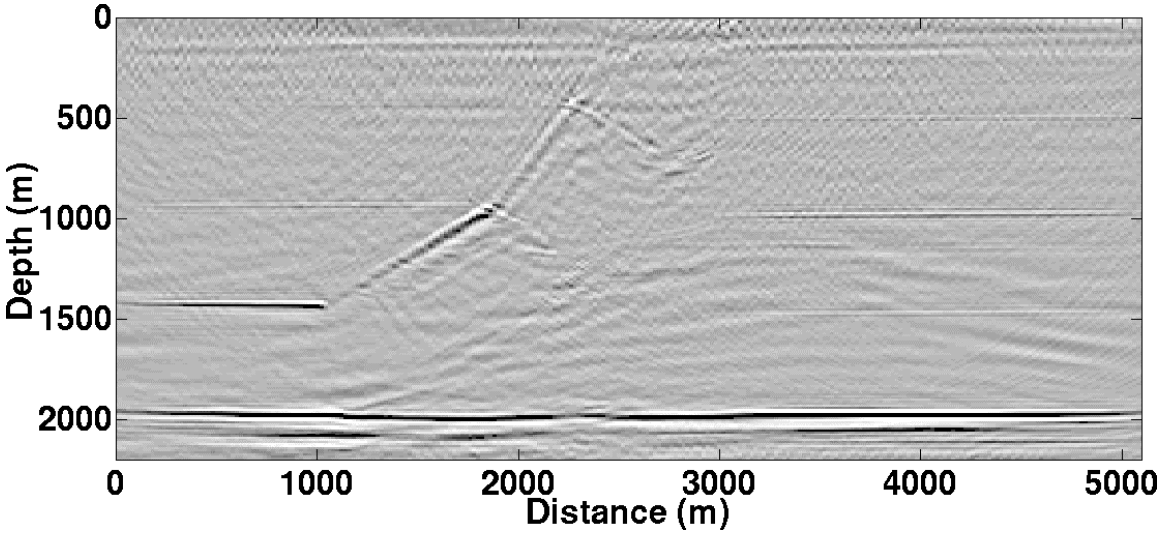

Fig. 4.19. The superposition of all TI depth-imaged source gathers. The base of the model has been correctly imaged and the interfaces between the TI blocks are imaged and positioned quite well compared to the model (Figure 4.15) and the image from isotropic migration (Figure 4.20).

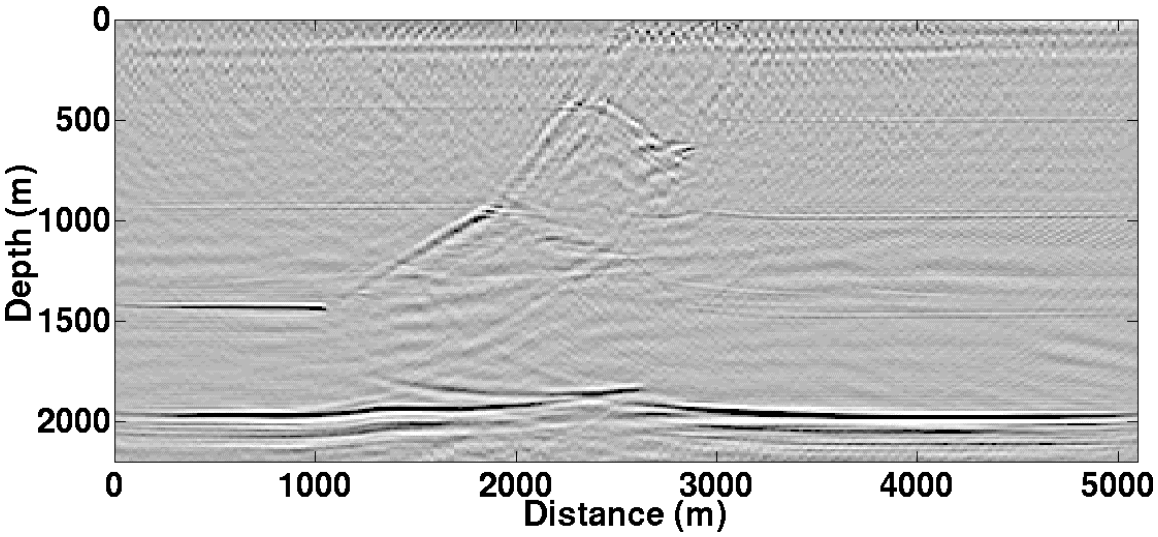

Fig. 4.20. The superposition of all isotropic-depth images of the source gathers. The base of the model has been poorly imaged and the interfaces between the TI blocks are mispositioned.

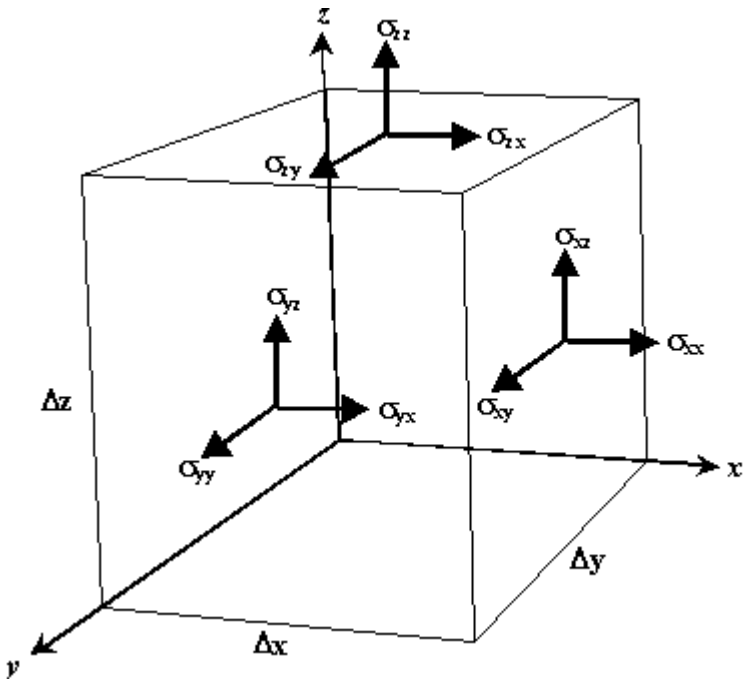

Fig. 4.21. Components of stress σ_{ij} acting on a small volume whose sides are Δx, Δy and Δz.

CHAPTER 5

TAYLOR SERIES DERIVATION OF NONSTATIONARY WAVEFIELD EXTRAPOLATORS

5.0 INTRODUCTION

In this Chapter, the NSPS and PSPI extrapolators are derived from a Taylor series representation for the extrapolation of a seismic wavefield. For extrapolation from z = 0 to z, the Taylor series requires all orders of depth derivatives (evaluated at $z = 0$) of the seismic wavefield. For the second derivative, the Helmholtz equation, with velocity a function of lateral coordinates, provides two alternate expressions that are exact for the second partial derivative. These expressions are nonstationary filters of combination and convolution form (sections **1.01** and **1.02**) or, equivalently, pseudo-differential equations in the normal and adjoint forms whose symbols are the square of the vertical wavenumber.

If the assumption is made that the n^{th} derivative is obtained by an equation similar to those for the second derivative, but with a symbol equal to the vertical wavenumber

evaluated at the n^{th} power, then two explicit formulae for the Taylor series are obtained. The formula that uses the combination form results in the PSPI extrapolator (equation 2.14) while the other (the convolution form) gives the NSPS operator (equation (2.21)). Following Etgen (1994), PSPI (in the nonstationary limit) is shown to be exactly equal to explicit frequency-space $(f-x)$ extrapolation methods implemented as infinitely long finite difference extrapolators and is therefore more accurate than $(f-x)$ implementations (they use truncated series). Both formulae, NSPS and PSPI, are shown to be approximate, but approximate in complementary ways.

Using a theorem for the *composition* of two pseudo-differential operators (Stein, 1993: 237-238) it is shown that the errors made by PSPI tend to cancel those made by NSPS. This suggests that a new symmetric extrapolator, built by averaging PSPI and NSPS, might be more accurate. The direct average of PSPI and NSPS is an explicit extrapolator for complex media that offers advantages in both accuracy and stability over other explicit methods. A similar analysis suggests a fourth operator that is a cascade of NSPS and PSPI. (This symmetric operator was first introduced by Margrave and Ferguson, 1998a and implemented in depth imaging by Ferguson and Margrave, 1999 and is described in detail in section **2.3**.) An operator notation is introduced to provide simpler and more compact description of nonstationary extrapolators.

A qualitative comparison of the four extrapolators is presented to illustrate their relative accuracy and stability. A wavefield consisting of a null background, in which a number of impulses are embedded, is extrapolated a large distance (200m) through a strongly varying velocity field. The resulting impulse responses are then reversed through

the same field. The two symmetric operators are found to more accurately recover the input through this inversion process. No formal proof is given to establish the equivalence of invertability and accuracy however, the perfect invertability (in the nonevanescent region) of stationary phase shift suggests that this test is adequate.

Relative stability is demonstrated by singular value decomposition. The extrapolation operators responsible for the forward propagation portion of the preceding experiment are decomposed into their constituent unitary and singular matrices. In the nonevanescent region, only phase changes should be applied to the wavefield and any singular values that are not equal to unity in this region represent non-physical growth or decay. All four extrapolators are found to be unstable in this way (Etgen, (1994) demonstrates the instability of PSPI), but the two symmetric extrapolators are found to be more stable and the average operator is the most stable.

5.1 THE SEISMIC WAVEFIELD AND NONSTATIONARY FILTERS

A seismic wavefield $\psi(z)$ at depth z in the subsurface is predictable from a wavefield $\psi(0)$ recorded at $z = 0$ by Taylor series (Berkhout, 1981). All orders of the depth derivatives of ψ must be known at $z = 0$ however, from the Helmholtz equation, only the second-depth derivative is exactly known. Two equivalent forms of the second derivative, derived from the Helmholtz equation, are classifiable as *pseudo differential operators* and *nonstationary filters*. This classification leads to the symmetric nonstationary phase-shift extrapolators developed in a later section. For now, it is demonstrated that the two equivalent second derivatives give rise to two approximate

forms for the first depth derivative and thus to two elemental (however not equivalent) forms for all the required depth derivatives. These forms are elemental in that they are simple and complementary and can be combined to get higher order extrapolators.

The series expansion of $\psi(z)$, in the z coordinate, gives $\psi(z)$ in terms of a known wavefield, for example $\psi(0)$ recorded at the surface $z = 0$

$$\psi(\mathbf{x},z)=\psi(\mathbf{x},0)+z\left[\frac{\partial}{\partial z}\psi(\mathbf{x},z)\right]_{z=0}+\frac{z^2}{2}\left[\frac{\partial^2}{\partial z^2}\psi(\mathbf{x},z)\right]_{z=0}+\cdots, \qquad (5.1)$$

where ψ is a monochromatic (in temporal frequency ω) wavefield given in lateral coordinates $\mathbf{x}=(x,y)$ and depth coordinate z. Unknown are the depth derivatives $\frac{\partial^n}{\partial z^n}$ of ψ.

An expression for the second depth derivative is found using the Helmholtz equation

$$\frac{\partial^2}{\partial z^2}\psi(\mathbf{x},z)=-\left[\nabla_{\mathbf{x}}^2+\left(\frac{\omega}{c(\mathbf{x})}\right)^2\right]\psi(\mathbf{x},z), \qquad (5.2)$$

where $\nabla_{\mathbf{x}}^2$ is the Laplacian over the lateral coordinates and $c(\mathbf{x})$ is the velocity at which ψ propagates. Fourier transform of the Helmholtz equation over $\mathbf{x}$ gives

$$\frac{\partial^2}{\partial z^2}\varphi(\mathbf{k},z) = -\int\left[\nabla_{\mathbf{x}}^2 + \left(\frac{\omega}{c(\mathbf{x})}\right)^2\right]\psi(\mathbf{x},z)\exp(i\mathbf{k}\cdot\mathbf{x})d\mathbf{x}\,, \tag{5.3}$$

where the spectrum φ of ψ is

$$\varphi(\mathbf{k},z) = \int\psi(\mathbf{x},z)\exp(i\mathbf{k}\cdot\mathbf{x})d\mathbf{x} \tag{5.4}$$

and $\mathbf{k} = (k_x, k_y)$ are wavenumber coordinates. Computation of the integral in equation (5.3) (Appendix 5) results in an expression for the second depth derivative of φ

$$\frac{\partial^2}{\partial z^2}\varphi(\mathbf{k},z) = -\int k_z^2(\mathbf{x},\mathbf{k})\psi(\mathbf{x},z)\exp(i\mathbf{k}\cdot\mathbf{x})d\mathbf{x}\,, \tag{5.5}$$

where the square of the vertical wave number k_z is

$$k_z^2(\mathbf{x},\mathbf{k}) = \left(\frac{\omega}{c(\mathbf{x})}\right)^2 - \mathbf{k}\cdot\mathbf{k}\,. \tag{5.6}$$

Equation (5.5) is an exact prescription for the second z derivative of ψ and is an *adjoint-form pseudo-differential operator that maps a wavefield ψ to the second-depth* derivative of a spectrum φ and whose symbol is $-k_z^2$. It is also a nonstationary convolution filter. As a nonstationary filter, equation (5.5) is classified as a mixed-domain filter: the input is a wavefield and the output is a spectrum (Margrave, 1998). Any nonstationary filters can also be re-expressed in the Fourier and space domains (Margrave, 1998).

Another exact prescription for the second depth derivative is found by substituting for ψ on the right-hand side of equation (5.2) with the inverse Fourier transform of φ

$$\psi(\mathbf{x},z)=\frac{1}{(2\pi)^2}\int\varphi(\mathbf{k},z)\exp(-i\mathbf{k}\cdot\mathbf{x})d\mathbf{k}\,, \tag{5.7}$$

giving for the Helmholtz equation (5.2)

$$\frac{\partial^2}{\partial z^2}\psi(\mathbf{x},z)=-\frac{1}{(2\pi)^2}\left[\nabla_{\mathbf{x}}^2+\left(\frac{\omega}{c(\mathbf{x})}\right)^2\right]\int\varphi(\mathbf{k},z)\exp(-i\mathbf{k}\cdot\mathbf{x})d\mathbf{k}\,. \tag{5.8}$$

The operator contained by the square brackets in equation (5.8) can be moved inside the Fourier integral (Appendix 6) with the result

$$\frac{\partial^2}{\partial z^2}\psi(\mathbf{x},z)=-\frac{1}{(2\pi)^2}\int k_z^2(\mathbf{x},\mathbf{k})\varphi(\mathbf{k},z)\exp(-i\mathbf{k}\cdot\mathbf{x})d\mathbf{k}\,. \tag{5.9}$$

Equation (5.9) is a pseudo differential operator (Stein, 1993: 231) that maps a spectrum φ to the second-depth derivative of a wavefield ψ and whose symbol is k_z^2. It is also a nonstationary combination filter (Margrave, 1998). Like the convolution filter in equation (5.5) the combination filter is a mixed domain filter; the input and output are in different Fourier domains. The equivalence of the second derivatives, equations (5.9) and (5.5), is shown in Appendix 7.

5.2 ESTIMATION OF ALL DEPTH DERIVATIVES

The nonstationary convolution filter of equation (5.5) suggests that the n^{th} depth derivative is approximately

$$\frac{\partial^n}{\partial z^n}\varphi(\mathbf{k},z) \approx \left[D_+^n \psi(\mathbf{x},z)\right](\mathbf{k}) = \int \left[\pm ik_z(\mathbf{x},\mathbf{k})\right]^n \psi(\mathbf{x},z)\exp(i\mathbf{k}\cdot\mathbf{x})d\mathbf{x}, \qquad (5.10)$$

where the subscript '+' in the operator D_+^n indicates the operator applies a forward Fourier transform. The vertical wavenumber k_z is

$$k_z(\mathbf{x},\mathbf{k}) = \sqrt{\left(\frac{\omega}{c(\mathbf{x})}\right)^2 - \mathbf{k}\cdot\mathbf{k}}\,. \qquad (5.11)$$

From the combination filter of equation (5.9)

$$\frac{\partial^n}{\partial z^n}\psi(\mathbf{x},z) \approx \left[D_-^n \varphi(\mathbf{k},z)\right](\mathbf{x}) = \frac{1}{(2\pi)^2}\int \left[\pm ik_z(\mathbf{x},\mathbf{k})\right]^n \varphi(\mathbf{k},z)\exp(-i\mathbf{k}\cdot\mathbf{x})d\mathbf{k}, \qquad (5.12)$$

where the subscript (-) in derivative operator D_-^n indicates the operator applies an inverse Fourier transform and k_z is given by equation (5.11).

In this development it is assumed that velocity is invariant over the depth interval z and, in such a medium, the wavefield is decoupled into downgoing (+) and upgoing (-) modes (Fishman and McCoy, 1985). The desired direction of propagation dictates the choice of sign for k_z for both of equations (5.10) and (5.12).

The operators D_-^n and D_+^n provide, equivalently, the exact second derivatives, D_-^2 and D_+^2, but can only approximate the others. In the limit of constant *v* they become exact for all *n*. In a later section (**5.5**) the errors due to using the approximate derivatives D_-^n and D_+^n are characterized and found have opposing tendencies. In the next section, the derivative formulae are shown to give rise to NSPS and PSPI.

5.3 NONSTATIONARY FILTERS AND TAYLOR SERIES

The approximate depth derivatives D_-^n and D_+^n, given above by equations (5.10) and (5.12), when used in the series expansion for $\psi(z)$, give rise to the two elemental extrapolation methods. Derivative D_-^n leads to the phase-shift-plus-interpolation (PSPI) extrapolator (Gazdag and Sguazzero, 1984) in the limit of continuous lateral variation in velocity (Margrave and Ferguson, 1997; 1998a; 1999a). The other, D_+^n, leads to the nonstationary phase shift (NSPS) extrapolator of Margrave and Ferguson (1997; 1998a; 1999a).

Returning to the series representation of a wavefield ψ equation (5.1) the required n^{th} depth derivatives are replaced by D_-^n

$$\psi(\mathbf{x},z)=\psi(\mathbf{x},0)+z\left[D_-^1\varphi(\mathbf{k},0)\right](\mathbf{x})+\frac{z^2}{2}\left[D_-^2\varphi(\mathbf{k},0)\right](\mathbf{x})+\cdots, \qquad (5.13)$$

that can be written explicitly in terms of k_z (using equation (5.12)) as

$$\psi(\mathbf{x},z)=\frac{1}{(2\pi)^2}\int\left\{1\pm izk_z(\mathbf{x},\mathbf{k})+\frac{i^2z^2}{2}k_z^2(\mathbf{x},\mathbf{k})\pm\cdots\right\}\varphi(\mathbf{k},0)\exp(-i\mathbf{k}\cdot\mathbf{x})d\mathbf{k}\,, \qquad (5.14)$$

where the first term in equation (5.13) has been replaced by the inverse Fourier transform of φ and the resulting infinite series of inverse Fourier transforms is collected under a single transform. Recognizing the series expansion for the exponential function (the term in the curly braces) equation (5.14) becomes

$$\psi(\mathbf{x},z)=\left[L_P^{\pm}\varphi(\mathbf{k},0)\right](\mathbf{x})=\frac{1}{(2\pi)^2}\int\alpha(\mathbf{x},\mathbf{k},\pm z)\varphi(\mathbf{k},0)\exp(-i\mathbf{x}\cdot\mathbf{k})d\mathbf{k}\,, \qquad (5.15)$$

where linear operator $L_P^{\pm}$ is introduced. In this operator notation, subscript P stands for PSPI and the superscript determines the direction of propagation along the depth coordinate. The symbol of this pseudo-differential operator is

$$\alpha(\mathbf{k},\pm z)=\exp(\pm izk_z(\mathbf{x},\mathbf{k})), \qquad (5.16)$$

where k_z is given by equation (5.11). Linear operator $L_P^{\pm}$ applies the mixed domain form of a nonstationary filter known to be PSPI in the limit of continuous lateral variation in velocity (Margrave and Ferguson, 1997; 1998a; 1999a). It is also a standard form pseudo-differential operator (Stein, 1993: 231).

Fishman and McCoy (1985) develop the same limiting form of PSPI as a generalization of wave propagation in a homogeneous medium to a heterogeneous medium. They characterize it as a high frequency approximation (Fishman and McCoy, 1985).

The development of a second expression for wavefield extrapolation using D_+^n (equation (5.10)) requires the Fourier transform of the series representation of ψ (equation (5.1))

$$\varphi(\mathbf{k},z)=\varphi(\mathbf{k},0)+z\left[\frac{\partial}{\partial z}\varphi(\mathbf{k},z)\right]_{z=0}+\frac{z^2}{2}\left[\frac{\partial^2}{\partial z^2}\varphi(\mathbf{k},z)\right]_{z=0}+\cdots. \qquad (5.17)$$

Replacing the depth derivatives in equation (5.17) with D_+^n gives

$$\varphi(\mathbf{k},z)=\varphi(\mathbf{k},0)+z\left[D_+^1\psi(\mathbf{x},z)\right](\mathbf{k})+\frac{z^2}{2}\left[D_+^2\psi(\mathbf{x},z)\right](\mathbf{k})+\cdots, \qquad (5.18)$$

that is written in explicit terms of k_z as

$$\varphi(\mathbf{k},z)=\int\left\{1\pm izk_z(\mathbf{x},\mathbf{k})+\frac{i^2z^2}{2}k_z^2(\mathbf{x},\mathbf{k})\pm\cdots\right\}\psi(\mathbf{x},0)\exp(i\mathbf{k}\cdot\mathbf{x})d\mathbf{x}. \qquad (5.19)$$

The lead term $\varphi(z=0)$ in equation (5.18) has been replaced by the Fourier transform of ψ and the resulting infinite series of Fourier transforms is collected under a single transform. Again, recognizing the series expansion for the exponential, equation (5.19) becomes

$$\varphi(\mathbf{k},z)=\left[L_N^{\pm}\psi(\mathbf{x},0)\right](\mathbf{k})=\int\alpha(\mathbf{x},\mathbf{k},\pm z)\psi(\mathbf{x},0)\exp(i\mathbf{k}\cdot\mathbf{x})d\mathbf{x}, \qquad (5.20)$$

with α given by equation (5.16). Linear operator $L_N^{\pm}$ is the mixed domain form of a nonstationary wavefield extrapolator known as NSPS (Margrave and Ferguson, 1997; 1998a; 1999a). It is also the adjoint form pseudo-differential operator.

5.4 PSPI AND EXPLICIT FINITE DIFFERENCE METHODS

Implementation of nonstationary wavefield extrapolation can be done explicitly and without further approximation as is shown in Chapters 3 and 4. Here it is necessary, for greater understanding, to compare nonstationary methods with familiar explicit methods like finite difference. As will be shown, finite difference methods extend naturally from the nonstationary filter methods presented above.

In two spatial dimensions (x,z) the symbol k_z (equation (5.11)) of depth derivative D_-^1 (equation (5.12) with $n = 1$) is expanded as

$$k_z(x,k_x)=\frac{\omega}{c(x)}\left[1-\frac{1}{2}\left(\frac{c(x)}{\omega}\right)^2 k_x^2+\frac{1}{8}\left(\frac{c(x)}{\omega}\right)^4 k_x^4-\cdots\right]. \qquad (5.21)$$

Recognizing that $\frac{\partial}{\partial x^2}\Leftrightarrow k_x^2$ leads to a series expression for D_-^1

$$\left[D_-^1\psi(x,z)\right](x)=\pm\frac{\omega}{c(x)}\left[1+\frac{i}{2}\left(\frac{c(x)}{\omega}\right)^2\frac{\partial^2}{\partial x^2}-\frac{1}{8}\left(\frac{c(x)}{\omega}\right)^4\frac{\partial^4}{\partial x^4}+\cdots\right]\psi(x,z), \quad (5.22)$$

where the series representation has been moved outside of the integral and the inverse Fourier transform of φ has been computed (Berkhout, 1981). In practice, the spatial derivatives are approximated by finite difference operators and the series in square brackets is truncated (Claerbout, 1976). Extrapolation of wavefield ψ then proceeds by equation (5.1) where the required orders of depth derivatives are computed using appropriate applications of equation (5.22). Equation (5.1) must be truncated to a

tractable number of terms as well. Modern implementations use better approximations to the square root and increasing numbers of terms in the series (see for example Holberg, 1988; Blacquiere et al., 1989; Hale, 1991a, 1991b; Soubaras, 1992).

Wavefield extrapolation by finite differences above is developed directly from the nonstationary filter of equation (5.12) and three levels of approximation are uncovered: the truncation of the square root, the truncation of the Laplacian and the truncation of the series representing the wavefield. These three approximations are in addition to those of nonstationary methods; thus, a nonstationary phase shift implementation will always be more accurate than the finite difference methods defined here. The increased accuracy of nonstationary methods comes at the expense of increased computational effort.

The first depth derivative expression used to develop the finite difference method also leads directly to PSPI (in the limit of continuous lateral velocity variation) equation (5.15). Therefore, the limiting form of PSPI is equivalent to an infinite series representation of the finite difference method. Etgen (1994) has also observed the equivalence of PSPI and finite differences.

5.5 ERROR ASSOCIATED WITH NSPS AND PSPI

The wavefield extrapolators $L_N^{\pm}$ (NSPS, equation (5.20)) and $L_P^{\pm}$ (PSPI, equation (5.15)) follow from two approximate forms of the n^{th} depth derivatives D_+^n (equation (5.10)) and D_-^n (equation (5.12)). It is natural to compare the exact second derivatives (equations (5.5) and (5.9)) to those that arise from two applications of the approximate

first derivatives D_+^1 and D_-^1. This comparison reveals complex valued error terms in both approximations that have opposing trends.

Beginning with D_+^1 the approximate second derivative is

$$\frac{\partial^2}{\partial z^2}\varphi(\mathbf{k},z) \approx \left[D_+^1 D_+^1 \psi(\mathbf{y},z)\right](\mathbf{k}) = -\int \hat{k}_z^2(\mathbf{y},\mathbf{k})\psi(\mathbf{y},z)\exp(i\mathbf{k}\cdot\mathbf{y})d\mathbf{y}, \qquad (5.23)$$

where symbol $\hat{k}_z^2$ is (Appendix 8)

$$\hat{k}_z^2(\mathbf{y},\mathbf{k}) = \frac{1}{(2\pi)^2}\iint k_z(\mathbf{x},\mathbf{k})k_z(\mathbf{y},\mathbf{m})\exp(i[\mathbf{m}-\mathbf{k}]\cdot[\mathbf{y}-\mathbf{x}])d\mathbf{m}d\mathbf{x}. \qquad (5.24)$$

From D_-^1 the approximate second derivative is

$$\frac{\partial^2}{\partial z^2}\psi(\mathbf{x},z) \approx \left[D_-^1 D_-^1 \varphi(\mathbf{m},z)\right](\mathbf{x}) = -\frac{1}{(2\pi)^2}\int \bar{k}_z^2(\mathbf{x},\mathbf{m})\varphi(\mathbf{m},z)\exp(-i\mathbf{m}\cdot\mathbf{x})d\mathbf{m},$$

(5.25)

where symbol $\bar{k}_z^2$ is (following a procedure analogous to Appendix 8)

$$\bar{k}_z^2(\mathbf{x},\mathbf{m}) = \frac{1}{(2\pi)^2}\iint k_z(\mathbf{x},\mathbf{k})k_z(\mathbf{y},\mathbf{m})\exp(i[\mathbf{m}-\mathbf{k}]\cdot[\mathbf{x}-\mathbf{y}])d\mathbf{y}d\mathbf{k}. \qquad (5.26)$$

Equations (5.23) and (5.25) are pseudo-differential equations with symbols $\hat{k}_z^2$ and $\bar{k}_z^2$ that map wavefield ψ (equation (5.23)) and spectrum φ (equation (5.25)) to their approximate second depth derivatives simultaneous with a change in Fourier domain.

Note, $\hat{k}_z^2$ and $\bar{k}_z^2$ are functions of different spatial variables; $\hat{k}_z^2$ depends upon the input lateral coordinates, while $\bar{k}_z^2$ depends upon the output coordinates. Their symbols, $\hat{k}_z^2$ and $\bar{k}_z^2$, are themselves composed of symbols $k_z(\mathbf{x},\mathbf{k})$ and $k_z(\mathbf{y},\mathbf{k})$. A general theorem for this composition of symbols (Stein, 1993: 237-238, or Taylor, 1996: 11-13) can be used to provide asymptotic formulae for $\hat{k}_z^2$ and $\bar{k}_z^2$. From Appendix 8 the formulae are

$$\begin{aligned}\hat{k}_z^2(\mathbf{x},\mathbf{m}) &= k_z^2(\mathbf{x},\mathbf{m}) - i\nabla_{\mathbf{m}}k_z(\mathbf{x},\mathbf{m})\cdot\nabla_{\mathbf{x}}k_z(\mathbf{x},\mathbf{m}) \\ &+ \frac{i^2}{2}\nabla_{\mathbf{m}}\nabla_{\mathbf{m}}k_z(\mathbf{x},\mathbf{m}):\nabla_{\mathbf{x}}\nabla_{\mathbf{x}}k_z(\mathbf{x},\mathbf{m}) - \cdots\end{aligned} \tag{5.27}$$

and

$$\begin{aligned}\bar{k}_z^2(\mathbf{x},\mathbf{m}) &= k_z^2(\mathbf{x},\mathbf{m}) + i\nabla_{\mathbf{m}}k_z(\mathbf{x},\mathbf{m})\cdot\nabla_{\mathbf{x}}k_z(\mathbf{x},\mathbf{m}) \\ &+ \frac{i^2}{2}\nabla_{\mathbf{m}}\nabla_{\mathbf{m}}k_z(\mathbf{x},\mathbf{m}):\nabla_{\mathbf{x}}\nabla_{\mathbf{x}}k_z(\mathbf{x},\mathbf{m}) + \cdots\end{aligned} \quad . \tag{5.28}$$

The first terms in these asymptotic forms reproduce the action of the exact second-depth derivative. However, terms of higher order represent error and the odd valued terms are complex. Generation of complex terms by application of D_+^1 or D_-^1 may explain the instability of $L_P^{\pm}$ observed by Etgen (1994) and, as will be shown, the equivalent instability of $L_N^{\pm}$. Uncontrolled complex values in the exponent k_z of α (equation (5.16)) can lead to instability during recursive application.

The validity of these asymptotic series requires the existence of all orders of spatial and wavenumber derivatives of k_z as given by equation (5.11). The wavenumber

derivatives will exist to all orders except possibly at the evanescent boundary. The spatial derivatives impose a condition of smoothness upon $c(\mathbf{x})$. This condition is not necessarily required for the NSPS and PSPI extrapolators themselves, but it is needed for this form of error analysis.

5.6 SYMMETRIC NONSTATIONARY PHASE SHIFT OPERATORS

In this section, two new nonstationary extrapolators $L_A^{\pm}$ and $L_{PN}^{\pm}$ are developed that are more accurate and more stable than $L_P^{\pm}$ and $L_N^{\pm}$. The accuracy and stability of the *average* extrapolator, $L_A^{\pm}$, is the result of averaging $L_P^{\pm}$ and $L_N^{\pm}$ as suggested by the depth-derivative analysis above to reduce error and improve stability. The second extrapolator $L_{PN}^{\pm}$ results from recognizing the complimentary nature of $L_P^{\pm}$ and $L_N^{\pm}$ as was shown in section **2.3**; $L_N^{\pm}$ carries a wavefield ψ to a spectrum φ and $L_P^{\pm}$ carries a spectrum φ to a wavefield ψ. Both extrapolators at some level average the vertical wavenumbers k_z corresponding to $L_P^{\pm}$ and $L_N^{\pm}$ resulting in greater accuracy and stability (shown in the next section).

Assuming that error decreases with increasing order in their series, then the average of symbols $\hat{k}_z^2$ and $\bar{k}_z^2$

$$\frac{\hat{k}_z^2(\mathbf{x},\mathbf{m})+\bar{k}_z^2(\mathbf{x},\mathbf{m})}{2}=k_z^2(\mathbf{x},\mathbf{m})+\frac{i^2}{2}\nabla_{\mathbf{m}}\nabla_{\mathbf{m}}k_z(\mathbf{x},\mathbf{m}):\nabla_{\mathbf{x}}\nabla_{\mathbf{x}}k_z(\mathbf{x},\mathbf{m})+\cdots \quad , \quad (5.29)$$

may have greater accuracy due to cancellation of every other term. Note also that the average symbol is always real valued (i.e., the complex terms have canceled). The above suggests that the depth derivatives required by equation (5.1) may be more stable and more accurately computed by averaging derivatives D_-^n and D_+^n. (A complete analysis would require characterizing the errors involved with all orders of depth derivatives. It is not attempted here.) Equation (5.1) is then written

$$\begin{aligned}\psi(\mathbf{x},z)=\psi(\mathbf{x},0)+\frac{1}{2}z\left[\left[D_-^1\varphi(\mathbf{k},z)\right](\mathbf{x})+\frac{1}{(2\pi)^2}\int\left[D_+^1\psi(\mathbf{x},z)\right](\mathbf{k})\exp(-i\mathbf{k}\cdot\mathbf{x})d\mathbf{k}\right]_{z=0}\\ +\frac{1}{2}\frac{z^2}{2}\left[\left[D_-^2\varphi(\mathbf{k},z)\right](\mathbf{x})+\frac{1}{(2\pi)^2}\int\left[D_+^2\psi(\mathbf{x},z)\right](\mathbf{k})\exp(-i\mathbf{k}\cdot\mathbf{x})d\mathbf{k}\right]_{z=0}+\cdots\end{aligned} \quad , \quad (5.30)$$

where derivatives corresponding to D_+^n are inverse Fourier transformed prior to averaging with those corresponding to D_-^n. Collecting terms, writing the derivatives explicitly in k_z and recognizing the series representation of the exponential reduces equation (5.30) to the average of the output of $L_P^{\pm}$ and the inverse Fourier transform of the output of $L_N^{\pm}$

$$\psi(\mathbf{x},z)=\frac{1}{2}\left[\begin{array}{l}\dfrac{1}{(2\pi)^2}\int\alpha(\mathbf{x},\mathbf{k},z)\varphi(\mathbf{k},z)\exp(-i\mathbf{k}\cdot\mathbf{x})d\mathbf{k}\\ +\dfrac{1}{(2\pi)^2}\iint\alpha(\mathbf{y},\mathbf{k},z)\psi(\mathbf{y},z)\exp(-i\mathbf{k}\cdot[\mathbf{x}-\mathbf{y}])d\mathbf{y}d\mathbf{k}\end{array}\right]. \qquad (5.31)$$

Replacing φ in equation (5.31) with the Fourier transform of ψ and collecting terms results in the following pseudo-differential operator equation

$$\begin{array}{l}\psi(\mathbf{x},z)=\left[L_A^{\pm}\psi(\mathbf{y},0)\right](\mathbf{x}) \;=\frac{1}{2}\left[L_N^{\pm}\psi(\mathbf{y},0)\right](\mathbf{x}) \;+\frac{1}{2}\left[L_P^{\pm}\psi(\mathbf{y},0)\right](\mathbf{x})\\ \frac{1}{2}\int\psi(\mathbf{y},0)\frac{1}{(2\pi)^2}\int[\alpha(\mathbf{y},\mathbf{k},\pm z)+\alpha(\mathbf{x},\mathbf{k},\pm z)]\exp(-\mathbf{k}\cdot[\mathbf{x}-\mathbf{y}])d\mathbf{k}d\mathbf{y}\end{array}. \qquad (5.32)$$

Unlike $L_N^{\pm}$ and $L_P^{\pm}$, $L_A^{\pm}$ is symmetric under the exchange of coordinates **x** and **y**.

A fourth extrapolator that is also symmetric is a cascade of $L_N^{\pm}$ and $L_P^{\pm}$ (section **2.3**). Beginning with $L_N^{\pm}$, extrapolate ψ through half the depth interval *z*/2

$$\left[L_N^{\pm\frac{1}{2}}\psi(\mathbf{y},0)\right](\mathbf{k})=\int\alpha\left(\mathbf{y},\mathbf{k},\pm\frac{z}{2}\right)\psi(\mathbf{y})\exp(i\mathbf{k}\cdot\mathbf{y})d\mathbf{y} \qquad (5.33)$$

and extrapolate the resulting spectrum through the remaining depth interval *z*/2

$$\left[L_P^{\pm\frac{1}{2}}L_N^{\pm\frac{1}{2}}\psi(\mathbf{y},0)\right](\mathbf{x})=\int\alpha\left(\mathbf{x},\mathbf{k},\pm\frac{z}{2}\right)\int\alpha\left(\mathbf{y},\mathbf{k},\pm\frac{z}{2}\right)\psi(\mathbf{y})\exp(i\mathbf{k}\cdot\mathbf{y})d\mathbf{y}\exp(-i\mathbf{k}\cdot\mathbf{x})d\mathbf{k}. \qquad (5.34)$$

Upon switching the order of integration the SNPS extrapolator $L_{PN}^{\pm}$ is defined

$$\left[L^{\pm}_{PN}\psi(\mathbf{y},0)\right](\mathbf{x}) = \left[L_P^{\pm\frac{1}{2}} L_N^{\pm\frac{1}{2}} \psi(\mathbf{y},0)\right](\mathbf{x})$$
$$= \int \psi(\mathbf{y}) \int \alpha\left(\mathbf{x},\mathbf{k},\pm\frac{z}{2}\right)\alpha\left(\mathbf{y},\mathbf{k},\pm\frac{z}{2}\right)\exp(-i\mathbf{k}\cdot[\mathbf{x}-\mathbf{y}])d\mathbf{k}d\mathbf{y} \quad . \qquad (5.35)$$

The subscript in $L^{\pm}_{PN}$ indicates $L_N^{\pm\frac{1}{2}}$ is applied first, followed by $L_P^{\pm\frac{1}{2}}$.

Like $L^{\pm}_{A}$, $L^{\pm}_{PN}$ is symmetric under an exchange of coordinates **x** and **y** (section **2.3**). (A fifth operator $L^{\pm}_{NP}$ would extrapolate spectra instead of wavefields.) Multiplication of the symbols α in equation (5.35) averages their respective vertical wavenumbers k_z suggesting that, like $L^{\pm}_{A}$, $L^{\pm}_{PN}$ can be expected to be more accurate and have greater stability than $L^{\pm}_{N}$ and $L^{\pm}_{P}$.

The average extrapolator $L^{\pm}_{A}$ and the cascade operator $L^{\pm}_{PN}$ are symmetric explicit extrapolators suitable for 2D or 3D depth imaging. Wapenaar and Grimbergen (1998) use reciprocity concepts to argue that accurate extrapolators should be symmetric in the $(\mathbf{x},\omega)$ domain. Note that ordinary phase shift has such symmetry. Many other symmetric forms, beyond the scope of this thesis, are possible including the Weyl form, which uses symbol $\alpha\left(\frac{\mathbf{x}+\mathbf{y}}{2},\mathbf{k},z\right)$.

5.7 AN ACCURACY AND STABILITY ANALYSIS

Extrapolators L^{+}_{P}, L^{+}_{N}, L^{+}_{A} and L^{+}_{PN} are assessed by first computing then inverting their respective impulse responses and by examining their singular value matrices. This is

done for a large extrapolation distance (200m) through a strongly variable velocity field. In the inversion experiment, the most accurate extrapolators, L_A^+ and L_{PN}^+, return the best images of the input. (This direct relationship between invertability and accuracy is not strictly proven but is inferred by analogy with the perfectly invertable stationary phase shift.) The most stable extrapolators, again L_A^+ and L_{PN}^+, have singular values closest to unity in the nonevanescent region. Relative stabilities are established because, over a large number of recursions, singular values not equal to unity will cause nonphysical growth or decay of the wavefield.

Figures 5.2a and 5.2b show the impulse responses $L_N^+\psi_{imp}$ and $L_P^+\psi_{imp}$ for extrapolation of the impulses ψ_{imp}, Figure 5.1a, through the velocity profile of Figure 5.1b. The velocity profile is a step function and two characteristic types of extrapolated wave energy are expected; one corresponding to the slow velocity on the right and one for the fast velocity on the left. In Figure 5.2a, $L_N^+\psi_{imp}$, the two types of wave energy are continuously superimposed (similar to Figure 1.3e), but there is no refraction at the velocity boundary. This is in contrast to the discontinuous superposition (similar to Figure 1.3d) with change in slope at the velocity boundary provided by $L_P^+\psi_{imp}$ (Figure 5.2b).

5.8 ACCURACY

Conducting the same experiment as above, but using the rapidly varying profile of Figure 5.3, produces the impulse responses $L_N^+\psi_{imp}$ and $L_P^+\psi_{imp}$ (Figures 5.4a and 5.4b).

Note how the characteristics of $L_N^+\psi_{imp}$ and $L_P^+\psi_{imp}$ are retained: $L_N^+\psi_{imp}$ gives a smooth superposition and $L_P^+\psi_{imp}$ gives discontinuous superposition.

Inversion of impulse responses $L_N^- L_N^+\psi_{imp}$ and $L_P^- L_P^+\psi_{imp}$ (Figures 5.4a and 5.4b) are given in Figures 5.5a and 5.5b. (The data of Figures 5.4a and 5.4b are extrapolated backward 200m.) Ideally, in the nonevanescent region, ψ_{imp} is resolved but because L_N^+ and L_P^+ are approximate extrapolators, reversing the direction of propagation does not restore the input. As $z \to 0$ $L_N^+\psi_{imp}$ and $L_P^+\psi_{imp}$ become perfectly invertable (not shown).

The impulse responses $L_{PN}^+\psi_{imp}$ and $L_A^+\psi_{imp}$ for extrapolation of the data in Figures 5.1a and 5.1b are given in Figures 5.6a and 5.6b. For $L_{PN}^+\psi_{imp}$, note how the discontinuous appearance of $L_P^+\psi_{imp}$ has been combined with that of the continuous appearance $L_N^+\psi_{imp}$. Impulse response $L_A^+\psi_{imp}$ is clearly the average of $L_N^+\psi_{imp}$ and $L_P^+\psi_{imp}$.

For the rapidly varying profile of Figure 5.3 impulse responses $L_{PN}^+\psi_{imp}$ and $L_A^+\psi_{imp}$ are given in Figures 5.7a and 5.7b. Arrows are annotated to indicate where obvious points of comparison are found. These points show that the characteristic averaged appearance of $L_A^+\psi_{imp}$ and the combined appearance of $L_{PN}^+\psi_{imp}$ are preserved. Inversions of these data, $L_{PN}^- L_{PN}^+\psi_{imp}$ and $L_A^- L_A^+\psi_{imp}$, are given in Figures 5.8a and 5.8b.

Unlike $L_N^- L_N^+ \psi_{imp}$ and $L_P^- L_P^+ \psi_{imp}$, inversion of the symmetric operators $L_{PN}^- L_{PN}^+ \psi_{imp}$ and $L_A^- L_A^+ \psi_{imp}$ provide good images of ψ_{imp}.

Because constant velocity phase shift has the attributes of perfect accuracy and invertability in the nonevanescent zone, the more accurate nonstationary extrapolator should demonstrate superior invertability. Based on this test, L_{PN}^+ and L_A^+ are more accurate extrapolators than L_N^+ and L_P^+ and because L_P^+ is the limiting form of explicit finite difference extrapolators, L_{PN}^+ and L_A^+ should be more accurate than explicit finite difference extrapolators as well.

5.9 STABILITY

The singular values of extrapolators L_P^+, L_N^+, L_A^+ and L_{PN}^+ are given in Figure 5.9 for the velocity profile of Figure 5.3. A depth interval of 100m and a temporal frequency of 40Hz were used. Under recursion, as in depth imaging by downward continuation, singular values not equal to unity in the nonevanescent zone cause nonphysical growth and decay of the wavefield. (Natural amplitude variations must be the result of superposition alone.) As Figure 5.9 shows, L_P^+, L_N^+, L_A^+ and L_{PN}^+ have singular values greater than zero, but those corresponding to L_A^+ and L_{PN}^+ are smaller; L_A^+ is closest to unity. The evanescent boundary occurs at about the 70th singular value and it is clear that L_A^+ decreases from unity sooner than the rest indicating the potential to be dispersive.

Figures 5.10a through 5.11b plot maximum singular value against a range of temporal frequencies and depth intervals (the scales are the same). The values for L^+_{PN} are smaller than those for L^+_P and L^+_N except at the largest depth intervals and temporal frequencies where they are slightly larger. The values for L^+_A average about 80% the value of the others, indicating that L^+_A is the most stable extrapolator of the four.

5.10 CHAPTER SUMMARY

Taylor series expansion of extrapolated wavefields was used to derive the elementary nonstationary wavefield extrapolators combination and convolution. Beginning with the Helmholtz equation (5.35) with velocity variation confined to the lateral coordinates, two exact nonstationary filter operators were found for the required second-depth derivative of the recorded wavefield. One is the convolution of a nonstationary wavenumber operator with the recorded wavefield and the other is the combination of the recorded spectrum with the same operator. These second-depth derivatives are equivalent in the space and Fourier domains.

Two general formulae for the depth derivatives were deduced from the exact second derivatives. Application to the Taylor series of the formula corresponding to convolution resulted in nonstationary phase shift (NSPS). The combination formula resulted in phase-shift-plus-interpolation in the nonstationary limit (PSPI). Comparison of the nonstationary extrapolators with commonly implemented explicit finite difference $(f-x)$ methods demonstrated that PSPI is equivalent to infinite series implementations

of $(f-x)$ methods. Thus, PSPI is the more accurate one-way extrapolator. There is no commonly implemented $(f-x)$ analogue to NSPS.

The relationship between nonstationary extrapolators and pseudo-differential operators provided a comparative basis for the exact second derivative and those implied by the two general derivative formulae. The comparison suggested that errors corresponding to nonstationary convolution and combination are complementary. That is, the average of their vertical wavenumbers tends to increase the order of the error and cancel complex values. A new symmetric extrapolator and an existing one (i.e., symmetric nonstationary phase shift), that exploit this relationship, were found to be more accurate and more stable than either NSPS or PSPI.

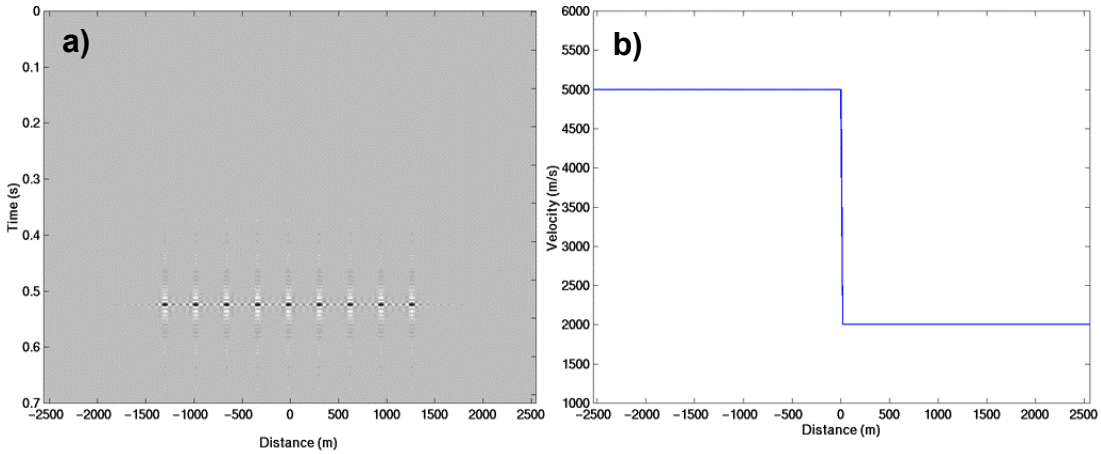

Fig. 5.1. a) impulses ψ_{imp} (bandlimited in space and time) used to generate impulse responses $L_N^+\psi_{imp}$, $L_P^+\psi_{imp}$, $L_{PN}^+\psi_{imp}$ and $L_A^+\psi_{imp}$. b) the velocity profile used to generate the impulse responses of Figures 5.2a, 5.2b, 5.6a and 5.6b.

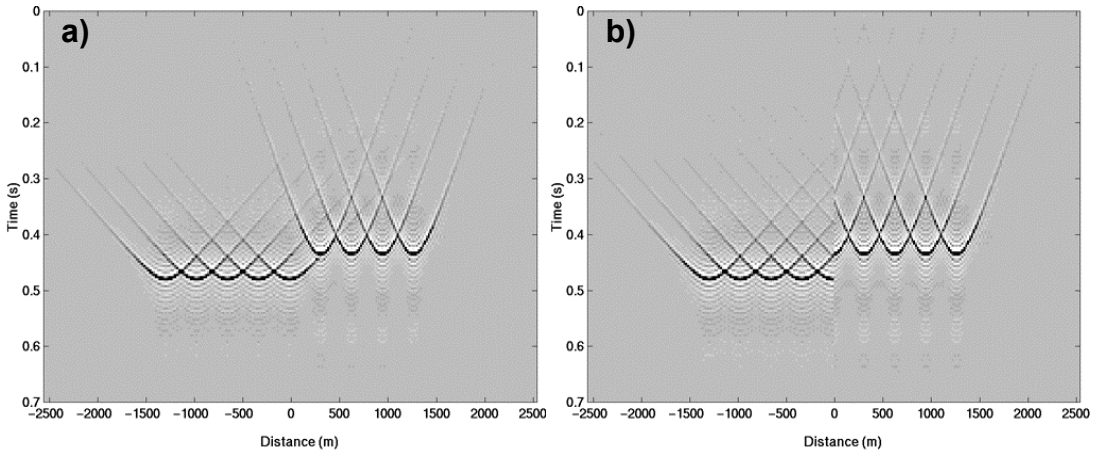

Fig. 5.2. Impulse responses $L_N^+\psi_{imp}$ and $L_P^+\psi_{imp}$ for extrapolation of the data of Figure 5.1a 200m through the velocity profile of Figure 5.1b. a) a smooth superposition is characteristic of $L_N^+\psi_{imp}$. b) a discontinuous superposition is characteristic of $L_P^+\psi_{imp}$.

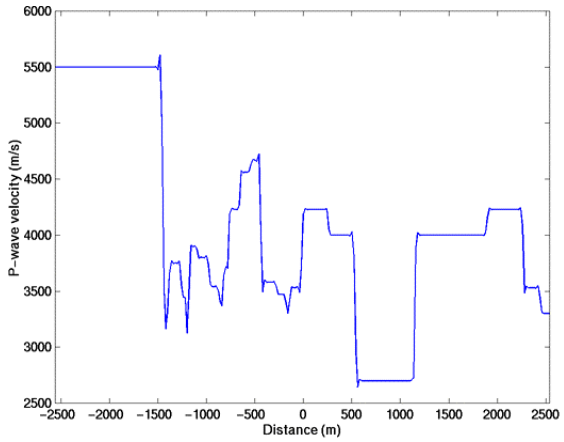

Fig. 5.3. a) A strongly varying velocity profile used to generate the impulse responses of Figures 5.4a, 5.4b, 5.7a and 5.7b.

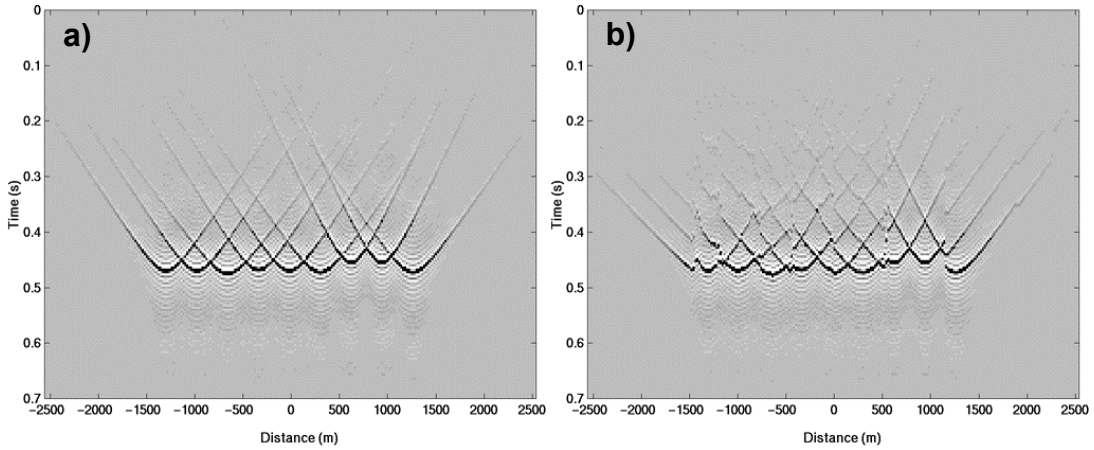

Fig. 5.4. Impulse responses $L_N^+\psi_{imp}$ and $L_P^+\psi_{imp}$ for the velocity profile of Figure 5.3. The depth interval was 200m. a) the characteristic smooth superposition of $L_N^+\psi_{imp}$ is retained. b) the characteristic discontinuous superposition for $L_P^+\psi_{imp}$ is also retained.

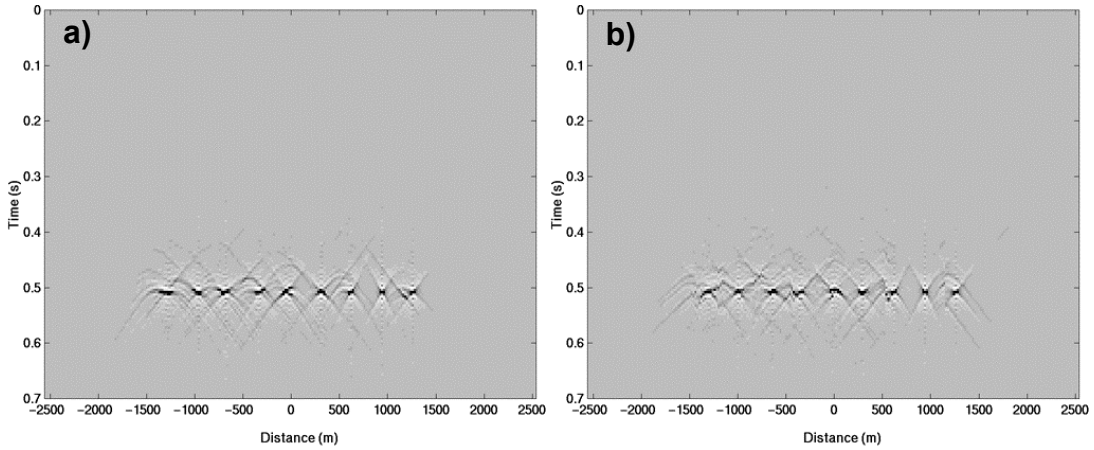

Fig. 5.5. The impulse responses of Figures 5.4a and 5.4b are inverted by extrapolating them –200m through the velocity profile of Figure 5.3. a) $L_N^-L_N^+\psi_{imp}$. b) $L_P^-L_P^+\psi_{imp}$. Neither inversion does a good job of recovering the input of Figure 5.1.

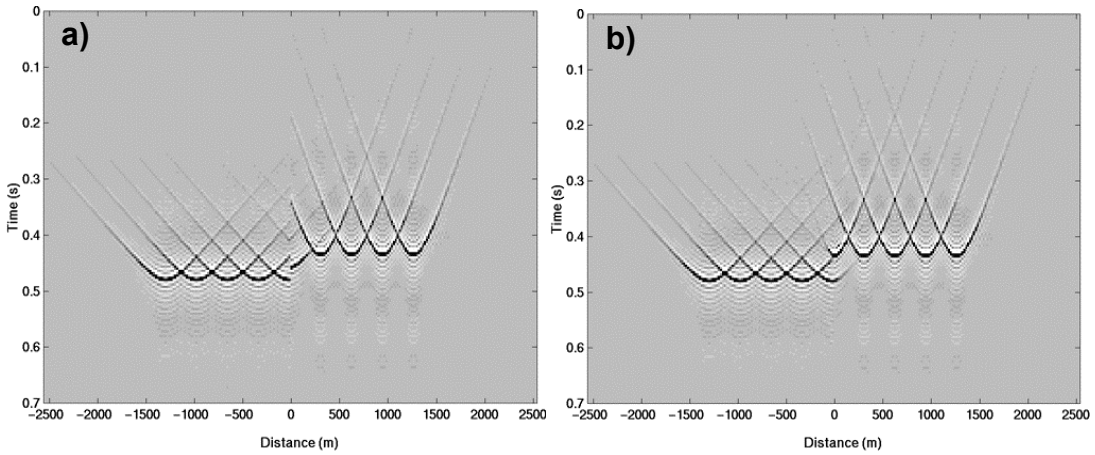

Fig. 5.6. Impulse responses $L_{PN}^{+}\psi_{imp}$ and $L_{A}^{+}\psi_{imp}$ for the data of Figures 5.1a and 5.1b. The depth interval was 200m. a) $L_{PN}^{+}\psi_{imp}$ combines the truncation effect of $L_{P}^{+}\psi_{imp}$ and the smooth superposition of $L_{N}^{+}\psi_{imp}$. b) averaging of $L_{N}^{+}\psi_{imp}$ and $L_{P}^{+}\psi_{imp}$ across velocity boundaries is characteristic of $L_{A}^{+}\psi_{imp}$.

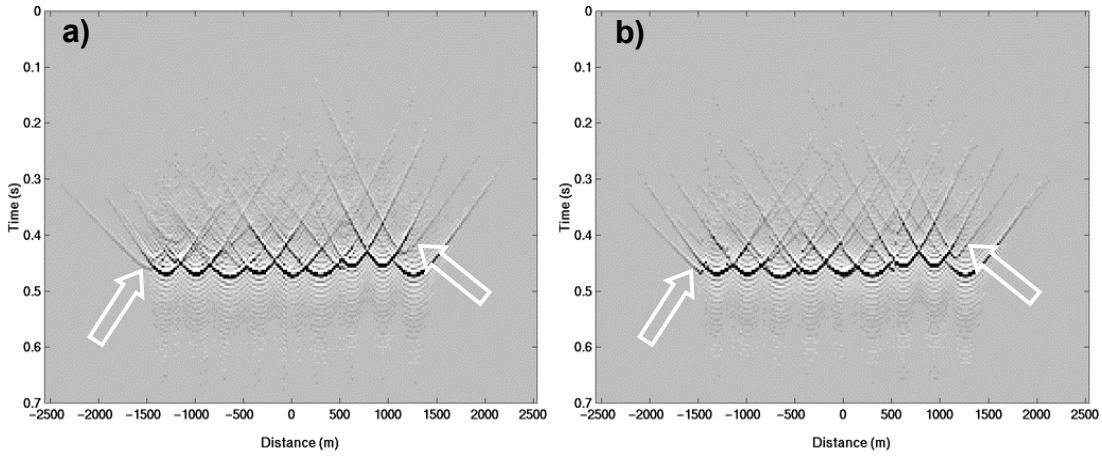

Fig. 5.7. Impulse responses $L^{+}_{PN}\psi_{imp}$ and $L^{+}_{A}\psi_{imp}$ for the velocity profile of Figure 5.3. The depth interval was 200m. a) the averaging effect of $L^{+}_{A}\psi_{imp}$ is difficult to see due to the complexity of the model. Arrows indicate two of the more obvious averaging characteristics of $L^{+}_{A}\psi_{imp}$ (this is most easily seen in comparison with Figure 5.7b. b) the combination of the effects of $L^{+}_{N}\psi_{imp}$ and $L^{+}_{P}\psi_{imp}$ characteristic of $L^{+}_{PN}\psi_{imp}$ are also difficult to see. Arrows are placed in the same locations as Figure 5.7a to aid comparison.

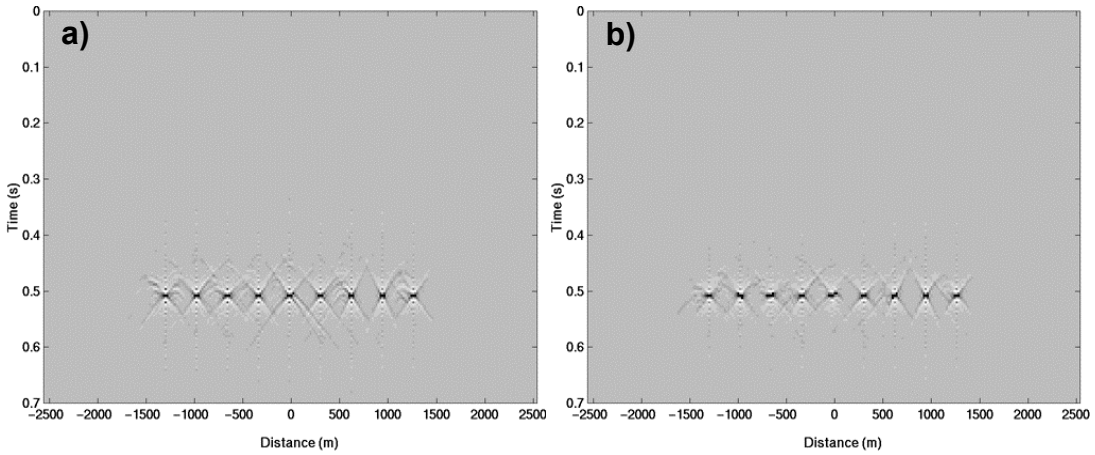

Fig. 5.8. The impulse responses of Figures 5.7a and 5.7b are inverted by extrapolating them –200m through the velocity profile of Figure 5.3. a) $L_{PN}^{-}L_{PN}^{+}\psi_{imp}$. b) $L_{A}^{-}L_{A}^{+}\psi_{imp}$. Both do a very good job of recovering the input of Figure 5.1.

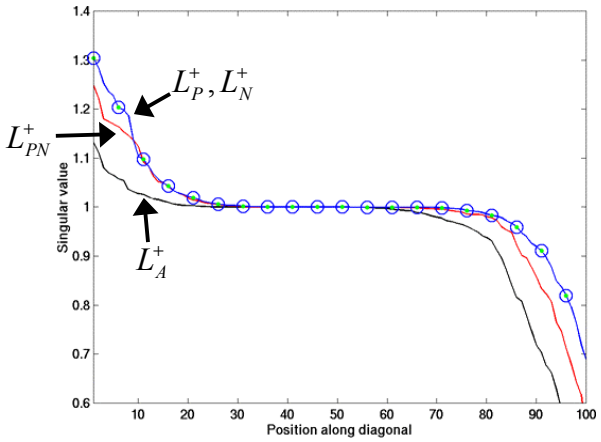

Fig. 5.9. A comparison of singular values for the velocity profile of Figure 5.3. The depth interval was 100m and the temporal frequency was 40Hz. The nonevanescent zone corresponds roughly to positions 1 through 70. All four extrapolators have singularities greater than one. During recursion, all four extrapolators will generate nonphysical growth of the wavefield. Extrapolator L_A^+ is the most stable, L_N^+ and L_P^+ exhibit identical stability and L_{PN}^+ has average stability. The singular values of L_A^+ decrease below unity sooner, as the evanescent boundary approaches, than the others. Thus, L_A^+ may be slightly more dispersive than the rest.

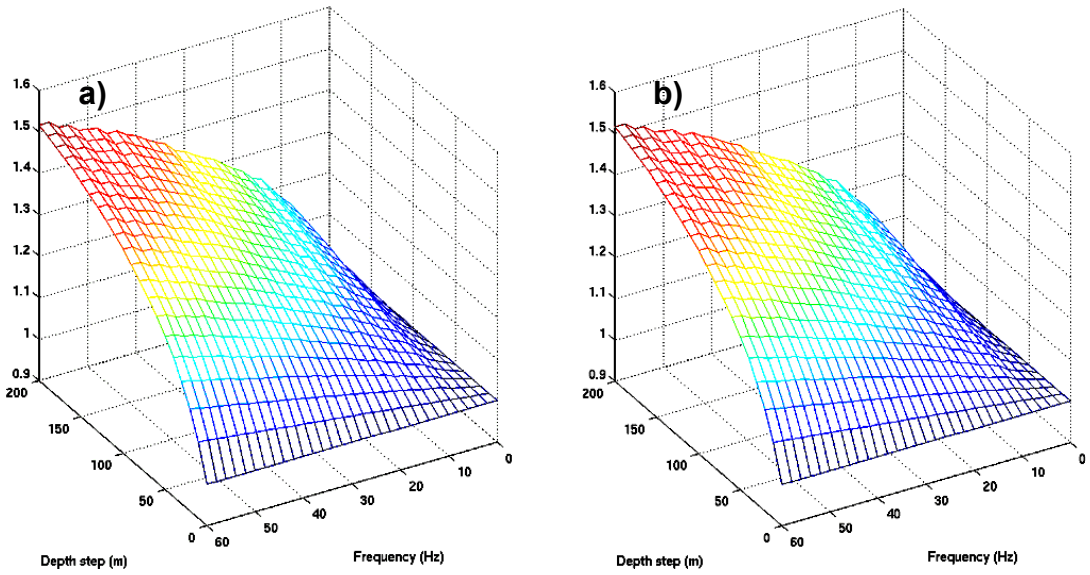

Fig. 5.10. The maximum singular values of L_N^+ a) and L_P^+ b) for the velocity profile of Figure 5.3. Maximum values for a range of temporal frequency and depth interval are plotted. They are essentially identical.

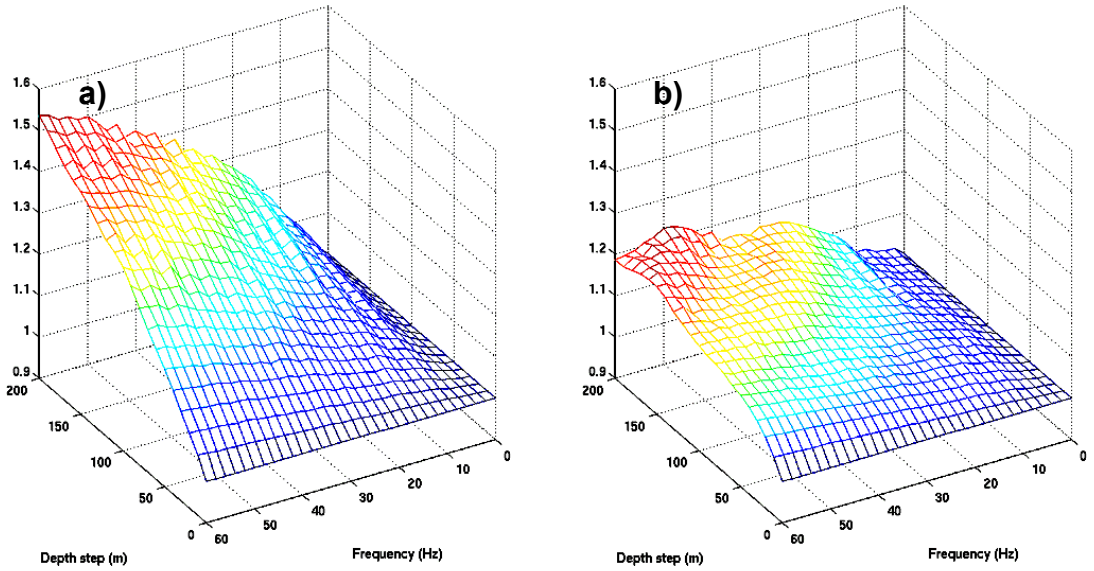

Fig. 5.11. The maximum singular values of L^{+}_{PN} and L^{+}_{A}, for the velocity profile of Figure 5.3, plotted for a range of depth intervals and frequencies. a) the values for L^{+}_{PN} are less than those of L^{+}_{N} and L^{+}_{P} every where but at the highest frequencies and largest depth steps. b) those for L^{+}_{A} average 80% the value of the other extrapolators.

CHAPTER 6

AN ERROR AND STABILITY ANALYSIS OF FOUR NONSTATIONARY WAVEFIELD EXTRAPOLATORS

6.0 INTRODUCTION

In this Chapter, wavefield extrapolators L_P^+, L_N^+, L_{PN}^+ and L_A^+ are evaluated for accuracy and stability by deriving the mathematical analogues of the inverse extrapolations presented in Chapter 5. The resulting equations represent propagation from $z = 0$ to z through a laterally variable medium, followed by propagation from z back $z = 0$. Assuming smooth variation of the extrapolation symbol α in lateral coordinate **x** it is shown that L_{PN}^+ and L_A^+ are invertible and that inversion of L_P^+ and L_N^+ results in complex valued error terms.

The Marmousi synthetic data set (Bourgeois et al., 1991) is used to compare the accuracy and stability of depth imaging methods based on the different extrapolators.

6.1 INVERSE OPERATORS, ACCURACY AND STABILITY

Inversion of a wavefield ψ extrapolated by L_P^+ has an associated error that results in an approximation ψ_P to ψ given by

$$\psi_P(\mathbf{x}) = \left[L_P^- \int \left[L_P^+ \varphi(\mathbf{m})\right](\mathbf{y}) \exp(i\mathbf{k}\cdot\mathbf{y}) d\mathbf{y}\right](\mathbf{x}) \ , \tag{6.1}$$

where $\mathbf{x} = (x_1, x_2)$ correspond to output space, $\mathbf{y} = (y_1, y_2)$ correspond to input space, $\mathbf{m} = (m_1, m_2)$ correspond to input wavenumbers, $\mathbf{k} = (k_1, k_2)$ correspond to output wavenumbers and φ is the spectrum of the input wavefield.

Equation (6.1) is the composition of two *pseudo-differential* operators L_P^+ and L_P^- that results in an equivalent operator L_P with the form

$$\psi_P(\mathbf{x}) = \left[L_P \varphi(\mathbf{m})\right](\mathbf{x}) \ , \tag{6.2}$$

or in integral form

$$\left[L_P \varphi(\mathbf{m})\right](\mathbf{x}) \ = \frac{1}{(2\pi)^2} \int c_P(\mathbf{x}, \mathbf{m}) \varphi(\mathbf{m}) \exp(-i\mathbf{m}\cdot\mathbf{x}) d\mathbf{m} \, , \tag{6.3}$$

with symbol c_P given by

$$c_P(\mathbf{x},\mathbf{m}) = \frac{1}{(2\pi)^2}\iint \alpha^-(\mathbf{x},\mathbf{k})\alpha^+(\mathbf{y},\mathbf{m})\exp(-i[\mathbf{k}-\mathbf{m}]\cdot[\mathbf{x}-\mathbf{y}])d\mathbf{y}d\mathbf{k}\,. \qquad (6.4)$$

Because inversion symbol c_P results from the composition of two pseudo-differential operators it has an asymptotic formula (Stein, 1993: 237)

$$c_P(\mathbf{x},\mathbf{m}) = 1 + i\nabla_{\mathbf{m}}\alpha^-(\mathbf{x},\mathbf{m})\cdot\nabla_{\mathbf{x}}\alpha^+(\mathbf{x},\mathbf{m}) + \frac{i^2}{2}\nabla_{\mathbf{m}}\nabla_{\mathbf{m}}\alpha^-(\mathbf{x},\mathbf{m}):\nabla_{\mathbf{x}}\nabla_{\mathbf{x}}\alpha^+(\mathbf{x},\mathbf{m}) + \cdots\,, \qquad (6.5)$$

where $\nabla_{\mathbf{m}}$ and $\nabla_{\mathbf{x}}$ are gradient operators and the **:** operator represents the contraction of two-second rank tensors. Symbol c_P is unity in the first term and all other terms represent error, with odd powers being complex valued. For α constant in **x**, c_P *is* unity and L_P equation (6.3) reduces to an inverse Fourier transform. (Inversion is exact for constant velocity.)

Inversion of L_N^+ applied to ψ results in an approximation φ_N to spectrum φ given by

$$\varphi_N(\mathbf{m}) = \left[L_N^- \frac{1}{(2\pi)^2}\int \left[L_N^+\psi(\mathbf{x})\right](\mathbf{k})\exp(-i\mathbf{k}\cdot\mathbf{y})d\mathbf{k}\right](\mathbf{m}). \qquad (6.6)$$

Equation (6.6) is a composition of two *adjoint-standard* pseudo-differential operators L_N^+ and L_N^-, whose equivalent operator L_N has the form

$$\varphi_N(\mathbf{m}) = [L_N \psi(\mathbf{x})](\mathbf{m}) \ , \tag{6.7}$$

or as an integral

$$[L_N \psi(\mathbf{x})](\mathbf{m}) \ = \int c_N(\mathbf{x},\mathbf{m}) \psi(\mathbf{x}) \exp(i\mathbf{m}\cdot\mathbf{x}) d\mathbf{x} \, , \tag{6.8}$$

with symbol c_N

$$c_N(\mathbf{x},\mathbf{m}) = \frac{1}{(2\pi)^2} \iint \alpha^-(\mathbf{y},\mathbf{m}) \alpha^+(\mathbf{x},\mathbf{k}) \exp(-i[\mathbf{m}-\mathbf{k}]\cdot[\mathbf{x}-\mathbf{y}]) d\mathbf{y} d\mathbf{k} \, . \tag{6.9}$$

Like c_P, inversion symbol c_N is the composition of two pseudo-differential operators and it too has an asymptotic formula (Appendix 9)

$$c_N(\mathbf{x},\mathbf{m}) = 1 - i\nabla_{\mathbf{m}}\alpha^-(\mathbf{x},\mathbf{m})\cdot\nabla_{\mathbf{x}}\alpha^+(\mathbf{x},\mathbf{m}) + \frac{i^2}{2}\nabla_{\mathbf{m}}\nabla_{\mathbf{m}}\alpha^-(\mathbf{x},\mathbf{m}) : \nabla_{\mathbf{x}}\nabla_{\mathbf{x}}\alpha^+(\mathbf{x},\mathbf{m}) - \cdots \, . \tag{6.10}$$

Symbol c_N is similar to c_P (equation (6.5)); the first term is unity and the error terms are products of derivatives. However, the odd powers of derivatives differ in sign. This suggests that an average of c_N and c_P will cancel complex values and increase the order of the error of the resulting symbol. In the limit of constant velocity, equation (6.8) reduces to a Fourier transform.

In the space domain, the inversion of the average operator L_A^+ is

$$[L_A\psi(\mathbf{y})](\mathbf{x}) = [L_A^- L_A^+ \psi(\mathbf{y})](\mathbf{x}) \ , \tag{6.11}$$

where, from Chapter 5 equation (5.32)

$$[L_A^+\psi(\mathbf{y})](\mathbf{x}) = \frac{1}{2}[L_N^+\psi(\mathbf{y})](\mathbf{x}) + \frac{1}{2}[L_P^+\psi(\mathbf{y})](\mathbf{x}) \ . \tag{6.12}$$

Expansion of equation (6.11) by replacing L_A^+ and L_A^- gives

$$[L_A\psi(\mathbf{y})](\mathbf{x}) = \frac{[L_P\psi(\mathbf{y})](\mathbf{x})}{4} + \frac{[L_N\psi(\mathbf{y})](\mathbf{x})}{4} + \frac{[L_P^- L_N^+\psi(\mathbf{y})](\mathbf{x})}{4} + \frac{[L_N^- L_P^+\psi(\mathbf{y})](\mathbf{x})}{4} \ . \tag{6.13}$$

The first two terms of L_A consist of the inversion operators L_P and L_N cast in the space domain as

$$[L_P\psi(\mathbf{y})](\mathbf{x}) = \int \psi(\mathbf{y}) \frac{1}{(2\pi)^2} \int c_P(\mathbf{x},\mathbf{k}) \exp(-i\mathbf{k}\cdot[\mathbf{x}-\mathbf{y}]) d\mathbf{k} d\mathbf{y} \tag{6.14}$$

and

$$[L_N\psi(\mathbf{y})](\mathbf{x}) = \int \psi(\mathbf{y}) \frac{1}{(2\pi)^2} \int c_N(\mathbf{y},\mathbf{k}) \exp(-i\mathbf{k}\cdot[\mathbf{x}-\mathbf{y}]) d\mathbf{k} d\mathbf{y} \ . \tag{6.15}$$

L_P and L_N are transposes in this domain. Substitution of c_P and c_N in equations (6.14) and (6.15) gives for L_P

$$[L_P\psi(\mathbf{y})](\mathbf{x}) = \psi(\mathbf{x}) + i\int\frac{1}{(2\pi)^2}\int\psi(\mathbf{x})\nabla_{\mathbf{k}}\alpha(\mathbf{x},\mathbf{k})\cdot\nabla_{\mathbf{x}}\alpha(\mathbf{x},\mathbf{k})\exp(-i\mathbf{k}\cdot[\mathbf{x}-\mathbf{y}])d\mathbf{k}d\mathbf{y} + i^2\cdots \quad (6.16)$$

and for L_N

$$[L_N\psi(\mathbf{y})](\mathbf{x}) = \psi(\mathbf{x}) - i\int\frac{1}{(2\pi)^2}\int\psi(\mathbf{y})\nabla_{\mathbf{k}}\alpha(\mathbf{y},\mathbf{k})\cdot\nabla_{\mathbf{y}}\alpha(\mathbf{y},\mathbf{k})\exp(-i\mathbf{k}\cdot[\mathbf{x}-\mathbf{y}])d\mathbf{k}d\mathbf{y} + i^2\cdots . \quad (6.17)$$

Operators L_P and L_N differ only in the sign of the odd orders of their derivatives (the odd orders are also complex). Their sum cancels these terms and increases the order of the error terms giving for the first two terms in equation (6.13)

$$\frac{[L_P\psi(\mathbf{y})](\mathbf{x})}{4} + \frac{[L_N\psi(\mathbf{y})](\mathbf{x})}{4} = \frac{\psi(\mathbf{x})}{2} + \frac{1}{2}i^2\int\frac{1}{(2\pi)^2}\int\psi(\mathbf{y})\nabla_{\mathbf{k}}\nabla_{\mathbf{k}}\alpha(\mathbf{y}):\nabla_{\mathbf{y}}\nabla_{\mathbf{y}}\alpha(\mathbf{y})\exp(-i\mathbf{k}\cdot[\mathbf{x}-\mathbf{y}])d\mathbf{k}d\mathbf{y} + \cdots . \quad (6.18)$$

The third term in equation (6.13) corresponds to forward extrapolation by L_N^+ followed by reverse extrapolation by L_P^-

$$[L_P^- L_N^+\psi(\mathbf{y})](\mathbf{x}) = \int\psi(\mathbf{y})\frac{1}{(2\pi)^2}\int\alpha^-(\mathbf{x},\mathbf{k})\alpha^+(\mathbf{y},\mathbf{k})\exp(-i\mathbf{k}\cdot[\mathbf{x}-\mathbf{y}])d\mathbf{k}d\mathbf{y} . \quad (6.19)$$

Substituting $\mathbf{u} = \mathbf{x} - \mathbf{y}$ in equation (6.19) gives

$$\left[L_P^- L_N^+ \psi(\mathbf{y})\right](\mathbf{x}) = \int \psi(\mathbf{x}-\mathbf{u}) \frac{1}{(2\pi)^2} \int \alpha^-(\mathbf{x},\mathbf{k}) \alpha^+(\mathbf{x}-\mathbf{u},\mathbf{k}) \exp(-i\mathbf{k}\cdot\mathbf{u}) d\mathbf{k} d\mathbf{u} \,. \quad (6.20)$$

Wavefield ψ can be approximated by Taylor series

$$\psi(\mathbf{x}-\mathbf{u}) = \psi(\mathbf{x}) - \mathbf{u}\cdot\nabla_{\mathbf{x}}\psi(\mathbf{x}) + (-\mathbf{u}\cdot\nabla_{\mathbf{x}})^2 \psi(\mathbf{x}) - \cdots . \quad (6.21)$$

Similarly, symbol α^+

$$\alpha^+(\mathbf{x}-\mathbf{u},\mathbf{k}) = \alpha^+(\mathbf{x},\mathbf{k}) - \mathbf{u}\cdot\nabla_{\mathbf{x}}\alpha^+(\mathbf{x},\mathbf{k}) + (-\mathbf{u}\cdot\nabla_{\mathbf{x}})^2 \alpha^+(\mathbf{x},\mathbf{k}) - \cdots . \quad (6.22)$$

Replacing ψ and α^+ in equation (6.20) with equations (6.21) and (6.22) gives

$$\left[L_P^- L_N^+ \psi(\mathbf{y})\right](\mathbf{x}) = \int \{[1 - \mathbf{u}\cdot\nabla_{\mathbf{x}} + \cdots]\psi(\mathbf{x})\} \frac{1}{(2\pi)^2} \int \alpha^-(\mathbf{x},\mathbf{k}) \{[1 - \mathbf{u}\cdot\nabla_{\mathbf{x}} + \cdots]\alpha^+(\mathbf{x},\mathbf{k})\} \exp(-\mathbf{k}\cdot\mathbf{u}) d\mathbf{k} d\mathbf{u} \,. \quad (6.23)$$

The first order terms in equation (6.23) are, beginning with the simplest

$$\psi(\mathbf{x}) \int \frac{1}{(2\pi)^2} \int \alpha^-(\mathbf{x},\mathbf{k}) \alpha^+(\mathbf{x},\mathbf{k}) \exp(-\mathbf{k}\cdot\mathbf{u}) d\mathbf{k} d\mathbf{u} = \psi(\mathbf{x}) \,, \quad (6.24)$$

next,

$$\begin{aligned}
&\nabla_{\mathbf{x}}\psi(\mathbf{x})\cdot\int\mathbf{u}\frac{1}{(2\pi)^2}\int\alpha^{-}(\mathbf{x},\mathbf{k})\alpha^{+}(\mathbf{x},\mathbf{k})\exp(-\mathbf{k}\cdot\mathbf{u})d\mathbf{k}d\mathbf{u}\\
&=\nabla_{\mathbf{x}}\psi(\mathbf{x})\cdot\int\frac{1}{(2\pi)^2}\int\mathbf{u}\exp(-\mathbf{k}\cdot\mathbf{u})d\mathbf{u}d\mathbf{k} \qquad (6.25)\\
&=0
\end{aligned}$$

and

$$\begin{aligned}
&\psi(\mathbf{x})\int\alpha^{-}(\mathbf{x},\mathbf{k})\nabla_{\mathbf{x}}\alpha^{+}(\mathbf{x},\mathbf{k})\cdot\frac{1}{(2\pi)^2}\int\mathbf{u}\exp(-\mathbf{k}\cdot\mathbf{u})d\mathbf{u}d\mathbf{k}\\
&=\psi(\mathbf{x})\int\alpha^{-}(\mathbf{x},\mathbf{k})\nabla_{\mathbf{x}}\alpha^{+}(\mathbf{x},\mathbf{k})\delta(\mathbf{k})d\mathbf{k} \qquad , \qquad (6.26)\\
&=\psi(\mathbf{x})\left\{\nabla_{\mathbf{k}}\alpha^{-}(\mathbf{x},\mathbf{k})\nabla_{\mathbf{x}}\alpha^{+}(\mathbf{x},\mathbf{k})+\alpha^{-}(\mathbf{x},\mathbf{k})\nabla_{\mathbf{x}}\nabla_{\mathbf{k}}\alpha^{+}(\mathbf{x},\mathbf{k})\right\}_{\mathbf{k}=0}\\
&=0
\end{aligned}$$

where for this last term

$$\begin{aligned}
&\nabla_{\mathbf{k}}\alpha^{\pm}(\mathbf{x},\mathbf{k})_{\mathbf{k}=0}=\pm\left[z\alpha^{\pm}(\mathbf{x},\mathbf{k})k_z(\mathbf{x},\mathbf{k})\nabla_{\mathbf{k}}k_z(\mathbf{x},\mathbf{k})\right]_{\mathbf{k}=0} \qquad (6.27)\\
&=0
\end{aligned}$$

and

$$\begin{aligned}
&\nabla_{\mathbf{k}}k_z(\mathbf{x},\mathbf{k})_{\mathbf{k}=0}=\left[\frac{1}{2}\left[\left(\frac{\omega}{c(\mathbf{x})}\right)^2+\mathbf{k}\cdot\mathbf{k}\right]^{-\frac{1}{2}}\mathbf{k}\right]_{\mathbf{k}=0}. \qquad (6.28)\\
&=0
\end{aligned}$$

Assuming that second order terms (and higher) are small, equation (6.23) reduces to the identity

$$\left[L_P^- L_N^+ \psi(\mathbf{y})\right](\mathbf{x}) \approx \psi(\mathbf{x}) \ , \tag{6.29}$$

from which it is inferred that, to first order, L_P^- and L_N^+ are inverses and therefore, the fourth term in equation (6.13) is

$$\left[L_N^- L_P^+ \psi(\mathbf{y})\right](\mathbf{x}) \approx \psi(\mathbf{x}) \ . \tag{6.30}$$

The inversion operator L_A equation (6.13) is now written to first order as

$$\left[L_A \psi(\mathbf{y})\right](\mathbf{x}) \approx \psi(\mathbf{x}). \tag{6.31}$$

The results from the previous discussion are sufficient to derive the inversion of L_{PN}^+

$$\left[L_{PN} \psi(\mathbf{y})\right](\mathbf{x}) = \left[L_P^{-\frac{1}{2}} L_N^{-\frac{1}{2}} L_P^{\frac{1}{2}} L_N^{\frac{1}{2}} \psi(\mathbf{y}) \right](\mathbf{x}) \tag{6.32}$$

and, using the associative properties of these operators, to first order L_P^- and L_N^+ are inverses therefore

$$\left[L_{PN} \psi(\mathbf{y})\right](\mathbf{x}) \approx \psi(\mathbf{x}) \ . \tag{6.33}$$

For comparison, L_P (equation (6.16)) to first order is

$$[L_P\psi(\mathbf{y})](\mathbf{x}) \approx$$
$$\psi(\mathbf{x}) + i\int \frac{1}{(2\pi)^2} \int \psi(\mathbf{x}) \nabla_{\mathbf{k}} \alpha(\mathbf{x},\mathbf{k}) \cdot \nabla_{\mathbf{x}} \alpha(\mathbf{x},\mathbf{k}) \exp(-i\mathbf{k}\cdot[\mathbf{x}-\mathbf{y}]) d\mathbf{k} d\mathbf{y} \qquad (6.34)$$

and for L_N

$$[L_N\psi(\mathbf{y})](\mathbf{x}) \approx$$
$$\psi(\mathbf{x}) - i\int \frac{1}{(2\pi)^2} \int \psi(\mathbf{y}) \nabla_{\mathbf{k}} \alpha(\mathbf{y},\mathbf{k}) \cdot \nabla_{\mathbf{y}} \alpha(\mathbf{y},\mathbf{k}) \exp(-i\mathbf{k}\cdot[\mathbf{x}-\mathbf{y}]) d\mathbf{k} d\mathbf{y} . \qquad (6.35)$$

Inverses L_{PN} (equation (6.33)) and L_A (equation (6.31)) have no error terms. Inverse operators L_P (equation (6.34)) and L_N (equation (6.35)) have error terms that are functions of spatial and wavenumber derivatives that are non zero for smooth variation in velocity. Thus, in this situation, extrapolators L_{PN}^+ and L_A^+ are more accurate than L_P^+ and L_N^+.

In terms of stability, again to first order, L_P and L_N have complex error terms, suggesting that L_P^+ and L_N^+ also generate complex values. Uncontrolled complex values during recursive application of these extrapolators may lead to the instability described in Chapter 5.

6.2 MARMOUSI

The Marmousi synthetic data (Bourgeois et al., 1991) were acquired for use in comparing depth imaging methods based on extrapolators L_N^+, L_P^+, L_A^+ and L_{PN}^+. The prestack data were depth imaged at a depth interval of 20m. This interval was chosen as

being large enough to illustrate the different stability and accuracy characteristics of the extrapolators without becoming unstable enough to preclude comparison. For a detailed description of prestack depth imaging using nonstationary extrapolators see Chapter 3.

Figure 6.1 shows the true reflectivity computed from the density and velocity profile of the model. Figures 6.2 through 6.5 show the depth images corresponding to L_N^+ (Figure 6.2), L_P^+ (Figure 6.3), L_A^+ (Figure 6.4) and L_{PN}^+ (Figure 6.5). The depth-imaging algorithm based on L_A^+ gives the best image, especially in the shallower part of the model. (Arrows annotated on the figures facilitate this comparison.) The steeply dipping faults are more clearly imaged using L_A^+ and a large part of the section is less obscured by noise.

Comparison of the average amplitudes of the images of Figure 2 through 5 show that L_A^+ and L_{PN}^+ are more stable than L_N^+ and L_P^+. The average absolute amplitudes corresponding to L_A^+ (~800) and L_{PN}^+ (~800) are 20% less than those corresponding to L_N^+ (~1000) and L_P^+ (~1000).

6.3 CHAPTER SUMMARY

A second error and stability analysis was presented for the nonstationary wavefield extrapolators L_N^+, L_P^+, L_A^+ and L_{PN}^+ defined in Chapter 5 based on analytic expressions that describe inversion of wavefields extrapolated by the four operators. The

analysis supports the discussion in Chapter 5 that L_A^+ and L_{PN}^+ are more accurate and more stable than elementary extrapolators L_N^+ and L_P^+. The first order result (i.e., smooth variation of the extrapolation symbol α in lateral coordinate **x**) proved the error related to the inversion of L_{PN}^+ and L_A^+ is less than the inversion of L_P^+ and L_N^+. Similarly, the greater stability of L_{PN}^+ and L_A^+ was indicated.

The Marmousi model data (Bourgeois et al., 1991) were used to provide a qualitative comparison of depth imaging methods based on the different extrapolators. The best image of the model was returned by the L_A^+ method. Comparison of the average amplitudes of the images showed that the depth images for all four extrapolators had grown in amplitude, but that L_{PN}^+ and L_A^+ had grown 20% less than L_P^+ and L_N^+.

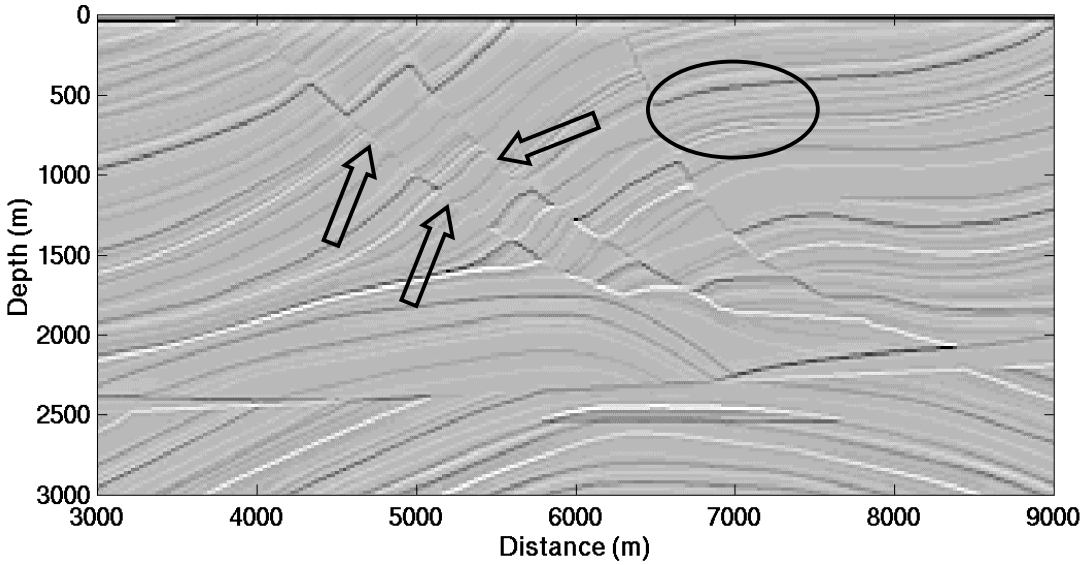

Fig. 6.1. The seismic reflectivity of Marmousi computed from the density and velocity profile of the model. The arrows and ring correspond to points of comparison with Figures 6.2 through 6.5.

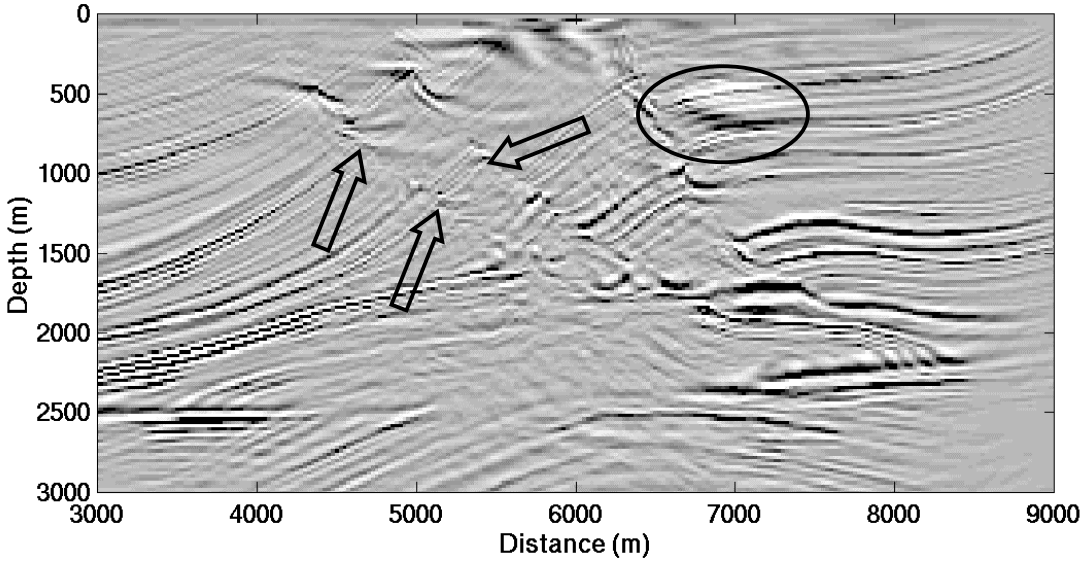

Fig. 6.2. Depth image of the Marmousi data set corresponding to L_N^+. The depth interval was 20m. The mean absolute amplitude of this image is approximately 1000. The arrows indicate points of comparison on two faults in the model. The ring encloses a flatter region that seems to suffer from noise. In this image the noise corresponds to a trough followed by a peak.

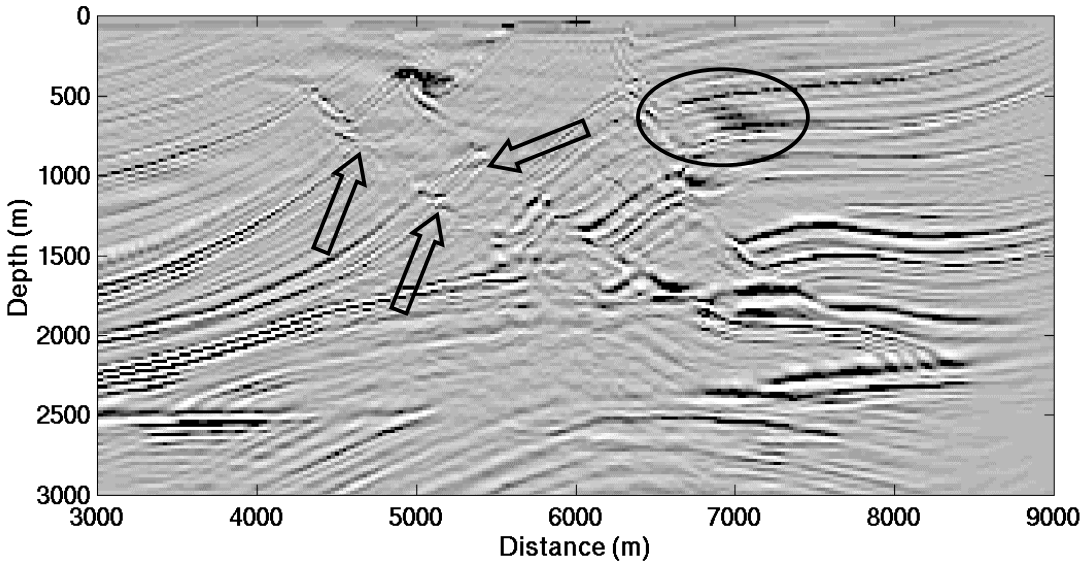

Fig. 6.3. Depth image of the Marmousi data set corresponding to L_P^+. The depth interval was 20m. The mean absolute amplitude of this image is approximately 1000. The images of the indicated faults are less well rendered by L_P^+ compared to L_A^+ (Figure 6.3). The noise in the ringed area is a strong peak.

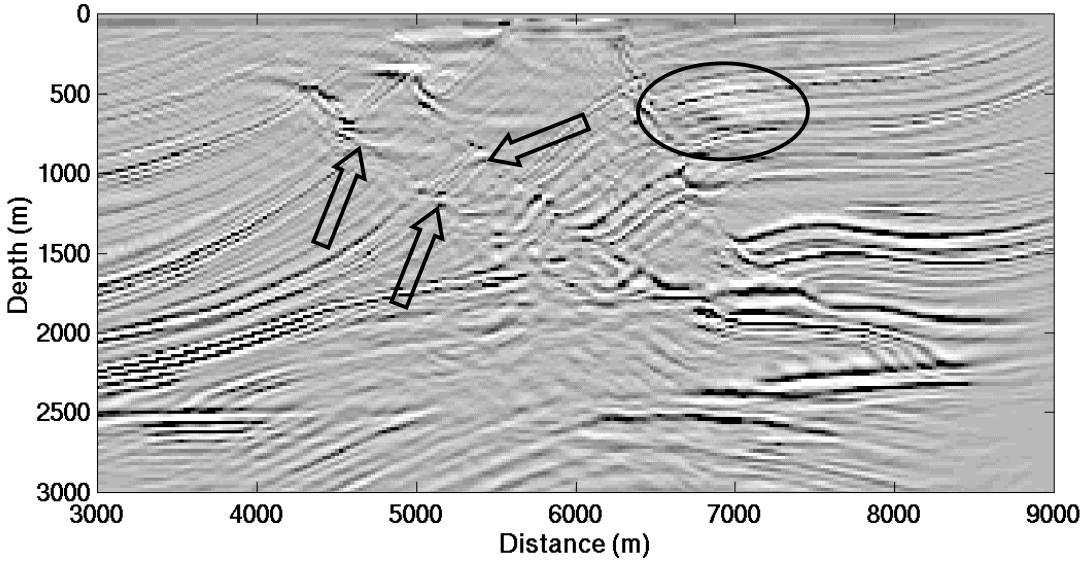

Fig. 6.4. Depth image of the Marmousi data set corresponding to L_A^+. The depth interval was 20m. The mean absolute amplitude of this image is approximately 800. The best focussing of the indicated faults is provided by this image. The noise in the ringed area is a strong trough.

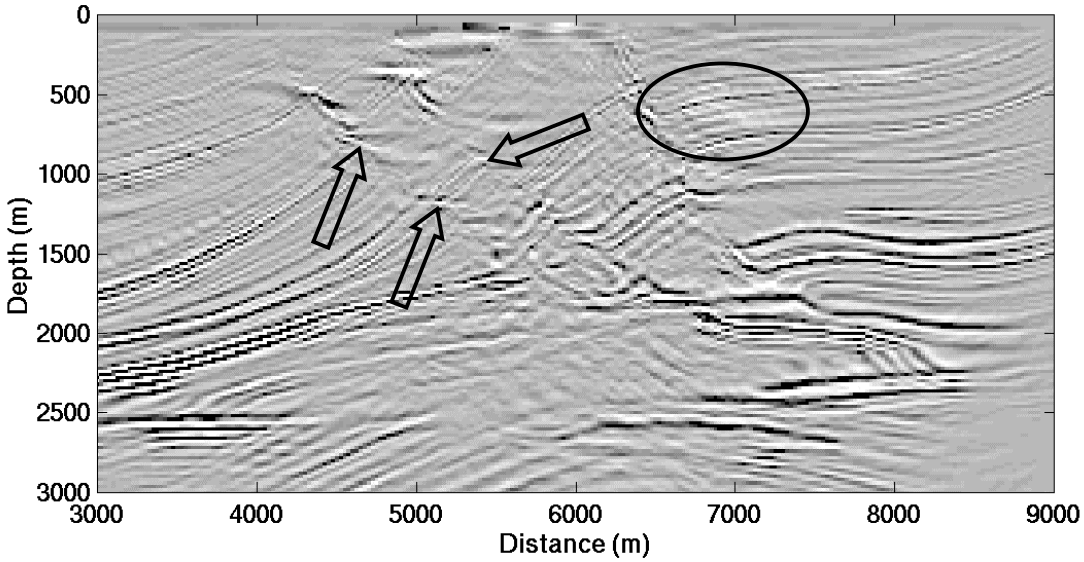

Fig. 6.5. Depth image of the Marmousi data set corresponding to L_{PN}^{+}. The depth interval was 20m. The mean absolute amplitude of this image is approximately 800. This image has the lowest noise in the ringed area.

CHAPTER 7

CONCLUSIONS

A new depth imaging method was presented based on nonstationary filter theory. It combines the well-known phase-shift-plus-interpolation method and the recently introduced nonstationary phase-shift method; both implemented as nonstationary filters into a single symmetric operator. It is suitable for imaging isotropic media whose velocity structure varies in all spatial coordinates. Implemented in a depth-imaging algorithm, the symmetric operator is used to compute incident and reflected wavefields at different depths using, respectively, a source waveform and geophone recordings. Seismic reflectivity (the image) is estimated by forming the ratio of the incident and reflected wavefields. Reflectivity is then immediately useful in providing a kinematic picture of the subsurface.

A simple implementation of the symmetric operator, one that required only a constant velocity extrapolator, was shown to be possible when the required velocity model is made piecewise constant laterally. Depth imaging would proceed by a sequence

of constant velocity phase shifts and applied spatial windows. The Marmousi synthetic data was used to test the utility of this method and a very good image resulted.

A new depth imaging method for dipping transversely isotropic (TI) media was presented based on the symmetric nonstationary phase shift (SNPS) method described in Chapter 3. The method is a cascade of two nonstationary extrapolators and is more accurate and more stable than other explicit-one-way extrapolators (Chapter 5; Chapter 6; Margrave and Ferguson, 1999b). Here, it was adapted for depth imaging in a TI medium with no restriction placed on the degree of the anisotropy, its heterogeneity or its axis of symmetry. Depth imaging of two TI models (physical seismic data) by SNPS provided superior images to those from isotropic and vertical transverse isotropy (VTI) methods.

Taylor series expansion of extrapolated wavefields leads directly to the elementary nonstationary wavefield extrapolators *combination* and *convolution*. Other more commonly implemented extrapolators are derived in this way and a comparison between them and nonstationary extrapolators was made. Nonstationary combination was found to be equivalent to infinite series implementations of recursive explicit extrapolators (often called ω-x methods) and thus more correctly approximates one-way extrapolation. No existing ω-x analogue exists for nonstationary *convolution*.

The relationship between nonstationary extrapolators and *pseudo-differential* operators provided a basis for an error analysis. Using the asymptotic formulae for the composition of two pseudo-differential operators, the errors corresponding to the combination and convolution operators were found to be complementary. (One of the

formulae may be original to this thesis.) That is, any composition of these operators, resulting in an averaging of their vertical wavnumbers, tends to increase the order of the resulting error and cancels complex values. A new symmetric extrapolator suggested by this analysis and an existing one (symmetric nonstationary phase shift) were shown to be more accurate and more stable than the elementary extrapolators.

A second error and stability analysis was presented for the nonstationary wavefield extrapolators L_N^+, L_P^+, L_A^+ and L_{PN}^+ defined in Chapter 5. The analysis was based on analytic expressions that describe inversion of wavefields extrapolated by the four operators. The expressions were based on asymptotic formulae for their inversion symbols. The analysis supports the conclusions expressed in Chapter 5 that L_A^+ and L_{PN}^+ are more accurate and more stable than elementary extrapolators L_N^+ and L_P^+.

The Marmousi synthetic data was used to provide a comparison of depth imaging using the different extrapolators. The largest mean absolute amplitudes of the resulting depth images corresponded to L_N^+ (approximately 1000) and L_P^+ (approximately 1000) indicating that recursive application of these extrapolators causes growth in the extrapolated wavefield. The mean amplitudes of L_A^+ (approximately 800) and L_{PN}^+ (approximately 800) are 20% less than L_N^+ and L_P^+ indicating greater stability. The best image of the model was returned by the L_A^+ method.

REFERENCES

Berkhout, A. J., 1981, Wave field extrapolation techniques in seismic migration, a tutorial: Geophysics, **46**, 1638-1656.

Berryhill, J. R., 1979, Wave-equation datuming: Geophysics, **44**, 1329 - 1334.

-------- 1984, Wave-equation datuming before stack: Geophysics, **49**, 2064 - 2066.

Black, J. L., Su, C. B., and Wason, C. B., 1984, Steep-dip depth migration: 54th Ann. Internat. Mtg. Soc. Expl. Geophys., Expanded Abstracts, 456-457.

Blacquiere, G., Debeye, H. W. J., Wapenaar, C. P. A., and Berkhout, A. J., 1989, 3D table-driven Berkhout, A. J., Cox, H., Verschuur, D., J., and Wapenaar, C., P., A., 1991, The Delphi approach to macro model estimation: in The Marmousi experience, EAGE, 87 - 111.

Bourgeois, A., Bourget, M., Lailly, P., Poulet, M., Ricarte, P., and Versteeg, R., 1991, Marmousi, model and data: in The Marmousi experience, EAGE, 5 - 9.

Claerbout, J. F., 1976, Fundamentals of geophysical data processing: McGraw-Hill Book Co., Inc.

--------- 1971, Toward a unified theory of reflector mapping: Geophysics, **36**, 467-481.

Daley, P. F., and Hron, F., 1977, Reflection and transmission coefficients for transversely isotropic media: Bull., Seis. Soc. Am., **67**, 661-675.

Etgen, J. J., 1994, Stability of explicit depth extrapolation through laterally-varying media: 64th Annual Internat. Mtg., Soc. Expl. Geophys., Expanded Abstracts, 1266-1269.

Ferguson, R., J., and Margrave G. F., 1999, A practical implementation of symmetric nonstationary phase shift: 69th Annual Internat. Mtg., Soc. Expl. Geophys., Expanded Abstracts, SPRO 11.5.

---------1998a, Depth migration in TI media by nonstationary phase shift: 68th Annual Internat. Mtg., Soc. Expl. Geophys., Expanded Abstracts, 1831-1834.

---------1998b, Depth migration by nonstationary phase shift: Annual Internat. Mtg., Can., Soc. Expl. Geophys., Expanded Abstracts, 150-151.

---------1997, Algorithm comparisons for nonstationary phase shift: CREWES 9th Annual Research Report, Ch. 31, 1-19

Fishman, L., and McCoy, J. J., 1985, A new class of propagation models based on a factorization of the Helmholtz equation: Geophys. J. astr. Soc., **80**, 439-461.

Gazdag, J., 1978, Wave equation migration with the phase shift method: Geophysics, **43**, 1342–1351.

Gazdag, J., and Squazerro, P., 1984, Migration of seismic data by phase shift plus interpolation: Geophysics, **49**, 124 - 131.

Gonzalez, A., Lynn, W., and Robinson, W. F., 1991, Prestack frequency-wavenumber (f-k) migration in transversely isotropic medium: 61st Ann. Internat. Mtg., Soc. Expl. Geophys., Expanded Abstracts, 1155-1157.

Grimbergen, J. L. T., Dessing, F. J., and Wapenaar, C. P. A., 1998, Modal expansion of one-way operators in laterally varying media: Geophysics, **63**, 995-1005.

Hale, D., Hill N. R., Stefani, J., 1992, Imaging salt with turning waves: Geophysics, **57**, 1453-1463.

Hale, D., 1991a, 3-D depth migration via McClellan transformations: Geophysics, **56**, 1778-1785.

---------- 1991b, Stable explicit extrapolation of seismic wavefields: Geophysics, **56**, 1770-1777.

Holberg, O., 1988, Towards optimum one-way wave propagation: Geophysical Prospecting, **36**, 99-114.

Isaac J. H., and Lawton, D. C., 1999, Image mispositioning due to dipping TI media: A physical seismic modeling study: Geophysics, **64**, 1230-1238.

Kitchenside, P. W., 1992, 2-D anisotropic migration in the space-frequency domain: Journal of seismic exploration, **2**, 7-22.

Love, A. E. H., 1927, A treatise on the mathematical theory of elasticity: Cambridge University Press, Cambridge.

Margrave, G.F., 1998, Theory of nonstationary linear filtering in the Fourier domain with application to time-variant filtering: Geophysics, **63**, 244-259.

Margrave, G. F., and Ferguson, R. J., 1999a, Wavefield extrapolation by nonstationary phase shift: Geophysics, **64**, 1067-1078.

---------1999b, An explicit symmetric wavefield extrapolator for depth migration: 69th Annual Internat. Mtg., Soc. Expl. Geophys., Expanded Abstracts, SPRO 14.4.

---------1998a, Nonstationary filters, pseudo-differential operators and their inverses: CREWES 11th Annual Research Report, Ch. 26, 1-17.

---------1998b, Explicit Fourier wavefield extrapolators: CREWES 11th Annual Research Report, Ch. 39, 1-24.

---------1997, Wavefield extrapolation by nonstationary phase shift: 67th Annual Internat. Mtg., Soc. Expl. Geophys., Expanded Abstracts, 1599-1602.

Martin, D., Ehinger, A., and Rasolofosaon, P N. J., 1992, Some aspects of seismic modeling and imaging in anisotropic media using laser ultrasonics: 62nd Ann. Internat. Mtg., Soc. Expl. Geophys., Expanded Abstracts, 1373-1376.

Meadows, M. A., and Abriel, W. L., 1994, 3-D phase-shift migration in transversely isotropic media: 64th Annual Internat. Mtg., Soc. Expl. Geophys., Expanded Abstracts, 1331-1348.

Meadows, M. A., Coen, S., and Liu, G., 1987, F-K migration in elliptically anisotropic media: 57th Ann. Internat. Mtg., Soc. Expl. Geophys., Expanded Abstracts, 659-661.

Morgan, T. R., 1983, Foundations of wave theory for seismic exploration: International Human Resources Development Corporation.

Peterson, B. E., 1983, Introduction to the Fourier transform and pseudo-differential operators: Pitman Publishing Limited.

Sena, A. G., Toksoz, M. N., 1993, Kirchhoff migration and velocity analysis for converted and nonconverted waves in anisotropic media: Geophysics, **58**, 265-276.

Soubaras, R., 1992, Explicit 3-D migration using equiripple polynomial expansion and Laplacian synthesis: 62nd Annual Internat. Mtg., Soc. Expl. Geophys., Expanded Abstracts, 905-908.

Stein, E. M., 1993, Harmonic analysis: real-variable methods, orthogonality, and oscillatory integrals: Princeton University Press.

Stoffa, P. L., Fokkema, J. T., de Luna Freire, R. M., and Kessinger, W. P., 1990, Split-step Fourier migration: Geophysics, **55**, 410-421.

Stolt, R., 1978, Migration by Fourier transform: Geophysics, **43**, 23-48.

Taylor M. E., Pseudodifferential operators: Prinston Univ. Press.

Temme, P., 1984, A comparison of common-midpoint, single-shot, and plane-wave depth migration: Geophysics, **49**, 1896 – 1907.

Thomsen, L., 1986, Weak elastic anisotropy: Geophysics, **51**, 1954-1966.

Ting, T. C. T., 1996, Anisotropic elasticity: Oxford University Press, New York, Oxford.

Treves, F., 1980, Introduction to pseudo-differential and Fourier integral operators: Plenum Press.

Tsvankin, I., 1997, Moveout analysis for transversely isotropic media with a tilted symmetry axis: Geophysical Prospecting, **45**, 479-512.

Uren, N. F., Gardner, G. H. F., and McDonald, J. A., 1990, The migrator's equation for anisotropic media: Geophysics, **55**, 1429-1434.

Uzcategui, O., 1995, 2-D depth migration in transversely isotropic media using explicit operators: Geophysics, **60**, 1819-1829.

Wapenaar, C. P. A., and Grimbergen, J.L.T., 1998, A discussion on stability analysis of wavefield depth extrapolation: 68th Annual Internat. Mtg., Soc. Expl. Geophys., Expanded Abstracts, 1716-1719.

Wu, R. S., 1992, Scattered field calculation in heterogeneous media using a phase-screen propagator: 62nd Annual Internat. Mtg., Soc. Expl. Geophys., Expanded Abstracts, 1289 - 1292.

Wu, R. S., 1994, Wide-angle elastic wave one-way propagation in heterogeneous media and an elastic wave complex-screen method: J. Geophys. Res., **99**, 751-766.

Wu, X. and Wu, R. S., 1998, An improvement to complex screen method for modeling elastic wave reflections: 68th Annual Internat. Mtg., Soc. Expl. Geophys., Expanded Abstracts, 1941-1944.

APPENDIX 1

REDUCTION OF THE NUMBER OF INDEPENDENT ELASTIC CONSTANTS BY REFLECTION ABOUT THE PLANE $x_1 = 0$, $x_2 = 0$

This appendix is adapted from Ting (1996: 40-48) and Love (1927: 127). Define the stress vector T_i as

$$T_i = \sigma_{ij} n_j , \tag{A1.1}$$

where n_i are the components of a unit surface normal. Transformation of **T** to a new coordinate system by the orthogonal transformation **Ω** is

$$\begin{aligned} T_i' &= \Omega_{ij} T_j \\ &= \left(\sigma_{ij} n_j\right)' = \left(c_{ijkl} \varepsilon_{kl} n_j\right)' \\ &= c'_{ijkl} \varepsilon'_{kl} n'_j \end{aligned} , \tag{A1.2}$$

where the prime indicates transformation to the new coordinate system. The elastic stiffnesses c' in the transformed coordinate system are given by

$$c'_{ijkl} = \Omega_{ip}\Omega_{jq}\Omega_{kr}\Omega_{ls}c_{pqrs} \quad . \tag{A1.3}$$

When $c' = c$ the material possesses symmetry with respect to Ω

$$c_{ijkl} = \Omega_{ip}\Omega_{jq}\Omega_{kr}\Omega_{ls}c_{pqrs} \quad . \tag{A1.4}$$

If Ω is specified as a reflection across a plane containing the x_3 axis

$$\Omega(\theta) = \begin{bmatrix} -\cos 2\theta & -\sin 2\theta & 0 \\ -\sin 2\theta & \cos 2\theta & 0 \\ 0 & 0 & 1 \end{bmatrix}, \tag{A1.5}$$

where θ is the angle that the plane makes with the x_1 axis then, for θ = 0

$$\Omega(\theta) = \begin{bmatrix} -1 & 0 & 0 \\ 0 & 1 & 0 \\ 0 & 0 & 1 \end{bmatrix} \tag{A1.6}$$

and equation (A1.4) requires that $c_{ijkl} = 0$ whenever one or three of *ijkl* equal unity. Thus, $c_{1112} = c_{1113} = c_{1222} = c_{1223} = c_{1233} = c_{1322} = c_{1323} = c_{1333} = 0$, or, in the contracted notation $C_{35} = C_{36} = C_{45} = C_{46} = C_{15} = C_{25} = C_{16} = C_{26} = 0$.

APPENDIX 2

SYMMETRY FOR ALL ANGLES ABOUT THE VERTICAL AXIS

This appendix is adapted from Ting (1996: 42). If a material has reflection symmetry about the plane $x_1 = 0$ and about a second plane making an angle of θ_0 with the x_1-axis (the axis of symmetry is the x_3-axis), the material has an infinite number of symmetry angles if θ_0 is equal to an irrational number times π. For example, for symmetry planes $\theta = 0$ and $\theta = \theta_0$, and a vector $\mathbf{x} = (x_1, x_2, x_3)^T$

$$\begin{aligned} \mathbf{x}^* &= \Omega(0)\Omega(\theta_0)\mathbf{x} \\ &= \begin{bmatrix} x_1 \cos 2\theta_0 - x_2 \sin 2\theta_0 \\ x_1 \sin 2\theta_0 + x_2 \cos 2\theta_0 \\ x_3 \end{bmatrix}, \end{aligned} \tag{A2.1}$$

can be written as a single operator

$$\mathbf{x} = \Omega(-\theta_0)\mathbf{x} \tag{A2.2}$$

and

$$\begin{aligned}\mathbf{x}^* &= \Omega(\theta_0)\Omega(0)\mathbf{x} \\ &= \begin{bmatrix} x_1\cos 2\theta_0 + x_2 \sin 2\theta_0 \\ -x_1 \sin 2\theta_0 + x_2 \cos 2\theta_0 \\ x_3 \end{bmatrix},\end{aligned} \tag{A2.3}$$

can be written as a single operator

$$\mathbf{x} = \Omega(2\theta_0)\mathbf{x}\,. \tag{A2.4}$$

Thus, if a material has symmetry planes at $\theta = 0$ and $\theta = \theta_0$ the material also has symmetry planes at $-\theta_0$ and $2\theta_0$. In fact, by applying the process repeatedly, the material has symmetry planes at $\theta = k\theta_0$ where k can be positive or negative. When θ_0 is a rational number times π, say, $\pi/2$, $\pi/3$, $\pi/4$, ..., $a\pi/b$, where a and b are integers, then

$$k\theta = \ldots,-\frac{a\pi}{b},\frac{a\pi}{b},2\frac{a\pi}{b},3\frac{a\pi}{b},\ldots,a\pi,\ldots,2a\pi,\ldots,4a\pi,\ldots, \tag{A2.5}$$

implies a finite number of angles of symmetry about z. For θ_0 that is an irrational number times π then

$$k\theta = \ldots,\frac{-\pi}{c},\frac{\pi}{c},2\frac{\pi}{c},\ldots, \tag{A2.6}$$

implies an infinite number of angles of symmetry. A material with infinitely many angles of symmetry about z is transversely isotropic.

APPENDIX 3

EQUATION OF MOTION

This appendix is adapted from Love (1927: 84-85) and Morgan (1983: 36-38). From Figure 3.21, a single component of force is a function of strains σ_{ij}

$$
\begin{aligned}
F_1 &= \left(\sigma_{11} + \frac{\partial \sigma_1}{\partial x_1} \Delta x_1 \right) \Delta x_2 \Delta x_3 - \sigma_{11} \Delta x_2 \Delta x_3 \\
&+ \left(\sigma_{12} + \frac{\partial \sigma_{12}}{\partial x_2} \Delta x_2 \right) \Delta x_1 \Delta x_3 - \sigma_{12} \Delta x_1 \Delta x_3 \\
&+ \left(\sigma_{13} + \frac{\partial \sigma_{13}}{\partial x_3} \Delta x_3 \right) \Delta x_1 \Delta x_2 - \sigma_{13} \Delta x_1 \Delta x_2 \\
&= \frac{\partial \sigma_{11}}{\partial x_1} \Delta x_1 \Delta x_2 \Delta x_3 + \frac{\partial \sigma_{12}}{\partial x_2} \Delta x_1 \Delta x_2 \Delta x_3 + \frac{\partial \sigma_{13}}{\partial x_3} \Delta x_1 \Delta x_2 \Delta x_3
\end{aligned}
,
$$

(A3.1)

where Δx_1, Δx_2 and Δx_3 are the lengths of the sides of a small volume of material. Then, for force F

$$F_i = \frac{\partial \sigma_{ij}}{\partial x_j} \Delta x \Delta y \Delta z \,. \tag{A3.2}$$

The force due to the applied stress is opposed by force due to the mass of the material displaced i.e.

$$F_i = \frac{\partial^2 u_i}{\partial t^2} \rho \Delta x \Delta y \Delta z \,, \tag{A3.3}$$

where ρ is the density of the material and $u_i = (u_1, u_2, u_3)$ are displacements in the coordinate directions. Equating (A3.2) and (A3.3) gives the equation of motion

$$\rho \frac{\partial^2 u_i}{\partial t^2} = \frac{\partial \sigma_{ij}}{\partial x_j} \tag{A3.4}$$

and, applying the stress-strain law (equation (A3.1))

$$\rho \frac{\partial^2 u_i}{\partial t^2} = \frac{\partial}{\partial x_j} \left[c_{ijkl} \varepsilon_{kl} \right]. \tag{A3.5}$$

The definition of linear strain, defined in terms of displacements u_i is

$$\varepsilon_{kl} = \frac{1}{2} \left(\frac{\partial u_k}{\partial x_l} + \frac{\partial u_l}{\partial x_k} \right) \tag{A3.6}$$

and, upon replacement in the equation of motion (A3.5) and using $c_{ijkl} = c_{ijlk}$ (Ting, 1996: 32)

$$\rho \frac{\partial^2 u_i}{\partial t^2} = \frac{\partial}{\partial x_j}\left[c_{ijkl} \frac{\partial u_k}{\partial x_l} \right]. \qquad \text{(A3.7)}$$

APPENDIX 4

P-WAVE VELOCITY IN A TI MEDIUM

This appendix is adapted from Daley and Hron (1977). The determinant in equation (3.11) can be written

$$\det\begin{pmatrix} p_1^2 A_{11} + p_2^2 A_{66} + p_3^2 A_{44} - 1 & p_1 p_2 A_{66} & p_1 p_3 [A_{13} + A_{44}] \\ p_1 p_2 A_{66} & p_1^2 A_{66} + p_2^2 A_{22} + p_3^2 A_{44} - 1 & p_2 p_3 [A_{23} + A_{44}] \\ p_1 p_3 [A_{13} + A_{44}] & p_2 p_3 [A_{23} + A_{44}] & p_1^2 A_{44} + p_2^2 A_{44} + p_3^2 A_{33} - 1 \end{pmatrix} = 0 \tag{A4.1}$$

where A_{mn} is related to the C_{mn} and density ρ by

$$A_{mn} = \frac{C_{mn}}{\rho}, \tag{A4.2}$$

with $A_{66} = \frac{1}{2\rho}[C_{11} - C_{12}]$. The components of slowness are

$$\frac{\partial \tau}{\partial x_i} = p_i \,. \qquad \text{(A4.3)}$$

Replacement of the slownesses p_i with their corresponding functions of velocity, equations (3.12) in the text and solving the determinant, results in 6thorder values for *v* and a very complicated relation. For a 2D medium, the (x_1, x_3) plane with the azimuthal angle $\phi = 0$, equation (A4.1) becomes

$$\det\begin{pmatrix} p_1^2 A_{11} + p_3^2 A_{44} - 1 & 0 & p_1 p_3 [A_{13} + A_{44}] \\ 0 & p_1^2 A_{66} + p_3^2 A_{44} - 1 & 0 \\ p_1 p_3 [A_{13} + A_{44}] & 0 & p_1^2 A_{44} + p_3^2 A_{33} - 1 \end{pmatrix} = 0 \,. \qquad \text{(A4.4)}$$

The solution of equation (A4.4) is only third order in *v* implying 3 roots corresponding to 3 modes of wave propagation, quasi-P, quasi-SV and quasi-SH. The solution for P-wave velocity v_p is given by equation (3.13) in the text.

APPENDIX 5

THE SECOND DEPTH DERIVATIVE OF THE RECORDED SEISMIC SPECTRUM FROM THE HELMHOLTZ EQUATION

The first term of the integrand in equation (5.3) is

$$\int \nabla_{\mathbf{x}}^2 \psi(\mathbf{x}, z) \exp(i\mathbf{k} \cdot \mathbf{x}) d\mathbf{x} = \int \exp(i\mathbf{k} \cdot \mathbf{x}) \frac{\nabla_{\mathbf{x}}^2}{(2\pi)^2} \int \varphi(\mathbf{m}, z) \exp(-i\mathbf{m} \cdot \mathbf{x}) d\mathbf{m} d\mathbf{x}, \tag{A5.1}$$

where ψ is expressed as an inverse Fourier transform of φ. (The notation for ω is suppressed for simplicity.) The Laplacian operates only on the Fourier kernal in equation (A5.1) and the order of integration can be reversed with the result

$$\int \nabla_{\mathbf{x}}^2 \psi(\mathbf{x}, z) \exp(i\mathbf{k} \cdot \mathbf{x}) d\mathbf{x} = -\frac{1}{(2\pi)^2} \int \mathbf{m} \cdot \mathbf{m} \varphi(\mathbf{m}, z) \int \exp(i\mathbf{x} \cdot [\mathbf{k} - \mathbf{m}]) d\mathbf{x} d\mathbf{m}, \tag{A5.2}$$

or, recognizing the delta function

$$\int \nabla_{\mathbf{x}}^2 \psi(\mathbf{x},z)\exp(i\mathbf{k}\cdot\mathbf{x})d\mathbf{x} = -\frac{1}{(2\pi)^2}\int \mathbf{m}\cdot\mathbf{m}\varphi(\mathbf{m},z)\delta(\mathbf{k}-\mathbf{m})d\mathbf{m} \qquad \text{(A5.3)}$$
$$= -\mathbf{k}\cdot\mathbf{k}\varphi(\mathbf{k},z)$$

Replacing spectrum φ with the Fourier transform of ψ gives

$$\int \nabla_{\mathbf{x}}^2 \psi(\mathbf{x},z)\exp(i\mathbf{k}\cdot\mathbf{x})d\mathbf{x} = -\mathbf{k}\cdot\mathbf{k}\int \psi(\mathbf{x},z)\exp(i\mathbf{k}\cdot\mathbf{x})d\mathbf{x}\,. \qquad \text{(A5.4)}$$

Equation (5.3) can now be written

$$\frac{\partial^2}{\partial z^2}\varphi(\mathbf{k},z) = -\int k_z^2(\mathbf{x},\mathbf{k})\psi(\mathbf{x},z)\exp(i\mathbf{k}\cdot\mathbf{x})d\mathbf{x}\,, \qquad \text{(A5.5)}$$

where the square of the vertical wavenumber k_z is

$$k_z^2(\mathbf{x},\mathbf{k})(\omega) = \left(\frac{\omega}{c(\mathbf{x})}\right)^2 - \mathbf{k}\cdot\mathbf{k}\,. \qquad \text{(A5.6)}$$

APPENDIX 6

THE SECOND DEPTH DERIVATIVE OF THE SEISMIC WAVEFIELD FROM THE HELMHOLTZ EQUATION

In equation (5.8), moving the operator in the square brackets inside the Fourier integral is possible due its independence of the wavenumber coordinates **k**

$$\frac{\partial^2}{\partial z^2}\psi(\mathbf{x},z,\omega) = -\frac{1}{(2\pi)^2}\int \varphi(\mathbf{k},z,\omega)\left[\left(\frac{\omega}{c(\mathbf{x})}\right)^2 \exp(-i\mathbf{k}\cdot\mathbf{x}) + \nabla_{\mathbf{x}}^2 \exp(-i\mathbf{k}\cdot\mathbf{x})\right] d\mathbf{k} \,. \tag{A6.1}$$

The Laplacian is thereby applied only to the Fourier kernal

$$\nabla_{\mathbf{x}}^2 \exp(-i\mathbf{k}\cdot\mathbf{x}) = -\mathbf{k}\cdot\mathbf{k}\exp(-i\mathbf{k}\cdot\mathbf{x}) \tag{A6.2}$$

and the equation for the second depth derivative (A6.1) becomes

$$\frac{\partial^2}{\partial z^2}\psi(\mathbf{x},z) = -\frac{1}{(2\pi)^2}\int k_z^2(\mathbf{x},\mathbf{k})\varphi(\mathbf{k},z)\exp(-i\mathbf{k}\cdot\mathbf{x})d\mathbf{k}\,, \tag{A6.3}$$

with k_z^2 given by equation (5.6).

APPENDIX 7

THE EQUIVALENCE OF THE SECOND DEPTH DERIVATIVES

The equivalence of the second depth derivatives, equations (5.5) and (5.9), is seen by converting both mixed domain expressions to a single domain. In the Fourier domain, for example, equation (5.5) requires ψ be replaced with the inverse Fourier transform of φ giving

$$\frac{\partial^2}{\partial z^2}\varphi(\mathbf{k},z)=\frac{1}{(2\pi)^2}\int\varphi(\mathbf{m},z)u(\mathbf{k},\mathbf{m})d\mathbf{m}, \qquad \text{(A7.1)}$$

where, for wavenumbers $\mathbf{m}=(m_x,m_y)$

$$u(\mathbf{k},\mathbf{m})=-\int\left[-\mathbf{k}\cdot\mathbf{k}+\left(\frac{\omega}{c(\mathbf{x})}\right)^2\right]\exp(i\mathbf{x}\cdot[\mathbf{m}-\mathbf{k}])d\mathbf{x}. \qquad \text{(A7.2)}$$

Separating equation (A7.2) into two terms gives

$$u(\mathbf{k},\mathbf{m}) = \mathbf{k}\cdot\mathbf{k}\int \exp(i\mathbf{x}\cdot[\mathbf{m}-\mathbf{k}])d\mathbf{x} - \int\left(\frac{\omega}{c(\mathbf{x})}\right)^2 \exp(i\mathbf{x}\cdot[\mathbf{m}-\mathbf{k}])d\mathbf{x}, \qquad \text{(A7.3)}$$

and, recognizing the delta function

$$u(\mathbf{k},\mathbf{m}) = \mathbf{k}\cdot\mathbf{k}\delta(\mathbf{m}-\mathbf{k}) - \int\left(\frac{\omega}{c(\mathbf{x})}\right)^2 \exp(i\mathbf{x}\cdot[\mathbf{m}-\mathbf{k}])d\mathbf{x}. \qquad \text{(A7.4)}$$

The Fourier transform of equation (5.9) is

$$\frac{\partial^2}{\partial z^2}\varphi(\mathbf{m},z) = \frac{1}{(2\pi)^2}\int \varphi(\mathbf{k},z)v(\mathbf{k},\mathbf{m})d\mathbf{k}, \qquad \text{(A7.5)}$$

where

$$v(\mathbf{k},\mathbf{m}) = -\int\left[-\mathbf{k}\cdot\mathbf{k} + \left(\frac{\omega}{c(\mathbf{x})}\right)^2\right]\exp(i\mathbf{x}\cdot[\mathbf{m}-\mathbf{k}])d\mathbf{x}. \qquad \text{(A7.6)}$$

Using the same process that leads to equation (A7.2), equation (A7.6) becomes

$$v(\mathbf{k},\mathbf{m}) = \mathbf{k}\cdot\mathbf{k}\delta(\mathbf{m}-\mathbf{k}) - \int\left(\frac{\omega}{c(\mathbf{x})}\right)^2 \exp(i\mathbf{x}\cdot[\mathbf{m}-\mathbf{k}])d\mathbf{x}. \qquad \text{(A7.7)}$$

Replacement of variables *u* and *v* in equations (A7.1) and (A7.5) with equations (A7.4) and (A7.5) leads to identical results.

APPENDIX 8

DERIVATION OF SYMBOLS $\hat{k}_z^2$ AND $\bar{k}_z^2$

Applying the first derivative operator, D_+^1, of equation (5.10) two times gives an expression for the second derivative

$$\frac{\partial^2}{\partial z^2}\varphi(\mathbf{k},z) \approx \left[D_+^1 \frac{\partial}{\partial z}\psi(\mathbf{x},z)\right](\mathbf{k}) = \int \pm ik_z(\mathbf{x},\mathbf{k})\frac{\partial}{\partial z}\psi(\mathbf{x},z)\exp(i\mathbf{k}\cdot\mathbf{x})d\mathbf{x} \quad \text{(A8.1)}$$

and, for general coordinates **w** and **n**,

$$k_z(\mathbf{w},\mathbf{n}) = \sqrt{\left(\frac{\omega}{c(\mathbf{w})}\right)^2 - \mathbf{n}\cdot\mathbf{n}}\,. \quad \text{(A8.2)}$$

The required first derivative $\frac{\partial}{\partial z}\psi$ is approximated as the inverse Fourier transform of the application of D_+^1 given by equation (5.10)

$$\frac{\partial}{\partial z}\psi(\mathbf{x},z) \approx \frac{1}{(2\pi)^2}\int\left[D_+^1\psi(\mathbf{x},z)\right](\mathbf{m})\exp(-i\mathbf{m}\cdot\mathbf{x})d\mathbf{m}\,. \qquad \text{(A8.3)}$$

The operator in equation (A8.3) is replaced and equation (A8.1) becomes

$$\frac{\partial^2}{\partial z^2}\varphi(\mathbf{k},z) = -\int\psi(\mathbf{y},z)\frac{1}{(2\pi)^2}\iint k_z(\mathbf{x},\mathbf{k})k_z(\mathbf{y},\mathbf{m})\exp(i\mathbf{m}\cdot[\mathbf{y}-\mathbf{x}])\exp(i\mathbf{k}\cdot\mathbf{x})d\mathbf{m}d\mathbf{x}d\mathbf{y}\,. \qquad \text{(A8.4)}$$

Manipulation of equation (A8.4) into a form similar to the exact second derivative of equation (5.5) involves the insertion of the term $\exp(i\mathbf{k}\cdot\mathbf{x})\exp(-i\mathbf{k}\cdot\mathbf{x})$ giving

$$\frac{\partial^2}{\partial z^2}\varphi(\mathbf{k},z) = -\int\hat{k}_z^2(\mathbf{y},\mathbf{k})\psi(\mathbf{y},z)\exp(i\mathbf{k}\cdot\mathbf{y})d\mathbf{y}\,, \qquad \text{(A8.5)}$$

where

$$\hat{k}_z^2(\mathbf{y},\mathbf{k}) = \frac{1}{(2\pi)^2}\iint k_z(\mathbf{y},\mathbf{m})k_z(\mathbf{x},\mathbf{k})\exp(i[\mathbf{m}-\mathbf{k}]\cdot[\mathbf{y}-\mathbf{x}])d\mathbf{m}d\mathbf{x}\,, \qquad \text{(A8.6)}$$

or, under an exchange of coordinates $\mathbf{x}\leftrightarrow\mathbf{y}$ and $\mathbf{k}\leftrightarrow\mathbf{m}$ (so that the output is in space coordinates **x** and wavenumbers)

$$\hat{k}_z^2(\mathbf{x},\mathbf{m}) = \frac{1}{(2\pi)^2}\iint k_z(\mathbf{x},\mathbf{k})k_z(\mathbf{y},\mathbf{m})\exp(i[\mathbf{k}-\mathbf{m}]\cdot[\mathbf{x}-\mathbf{y}])d\mathbf{m}d\mathbf{y}\,. \qquad \text{(A8.7)}$$

Equation (A8.7) is a symbol of the *composition* of two pseudo-differential operators. That is, it results from a pseudo-differential operator of the general form

$$[T_c f(\mathbf{x})](\mathbf{k}) = [T_a T_b f(\mathbf{x})](\mathbf{k}) \,, \tag{A8.8}$$

where T_a and T_b are two pseudo-differential operators with symbols *a* and *b* acting on a function *f* of coordinates **x** and T_c represents an equivalent combination operator with symbol *c* (Stein, 1993: 238). In equation (A8.7) symbols *a* and *b* correspond to $k_z(\mathbf{x})$ and $k_z(\mathbf{y})$ and symbol *c* corresponds to $\hat{k}_z^2(\mathbf{x})$. The symbols *c* of composition operations like equation (A8.8) have asymptotic formulae (Stein, 1993: 237). For example, beginning with equation (A8.7), compute the forward Fourier transform over **y**

$$\hat{k}_z^2(\mathbf{x},\mathbf{m}) = \frac{1}{(2\pi)^2}\int k_z(\mathbf{x},\mathbf{k}) K_z(-[\mathbf{k}-\mathbf{m}],\mathbf{m}) \exp(i\mathbf{x}\cdot[\mathbf{k}-\mathbf{m}])d\mathbf{k} \,, \tag{A8.9}$$

where

$$K_z(-[\mathbf{k}-\mathbf{m}],\mathbf{m}) = \int k_z(\mathbf{y},\mathbf{m}) \exp(-i\mathbf{y}\cdot[\mathbf{k}-\mathbf{m}])d\mathbf{y} \,. \tag{A8.10}$$

The replacement of variables $\mathbf{n} = \mathbf{k} - \mathbf{m}$ gives for equation (A8.9)

$$\hat{k}_z^2(\mathbf{x},\mathbf{m}) = \frac{1}{(2\pi)^2}\int k_z(\mathbf{x},\mathbf{m}+\mathbf{n}) K_z(-\mathbf{n},\mathbf{m}) \exp(i\mathbf{x}\cdot\mathbf{n})d\mathbf{n} \,, \tag{A8.11}$$

or equivalently

$$\hat{k}_z^2(\mathbf{x},\mathbf{m}) = \frac{1}{(2\pi)^2}\int k_z(\mathbf{x},\mathbf{m}-\mathbf{n}) K_z(\mathbf{n},\mathbf{m}) \exp(-i\mathbf{x}\cdot\mathbf{n})d\mathbf{n} \,. \tag{A8.12}$$

Expansion of symbol k_z gives

$$k_z(\mathbf{x},\mathbf{m}-\mathbf{n}) = k_z(\mathbf{x},\mathbf{m}) - \mathbf{n}\cdot\nabla_{\mathbf{m}} k_z(\mathbf{x},\mathbf{m}) + \frac{1}{2}(-\mathbf{n}\cdot\nabla_{\mathbf{m}})^2 k_z(\mathbf{x},\mathbf{m}) - \cdots \quad \text{. (A8.13)}$$

Replacement of k_z in equation (A8.12) with the above expansion gives

$$\hat{k}_z^2(\mathbf{x},\mathbf{m}) = k_z(\mathbf{x},\mathbf{m})k_z(\mathbf{x},\mathbf{m}) - \nabla_{\mathbf{m}} k_z(\mathbf{x},\mathbf{m})\cdot\frac{1}{(2\pi)^2}\int K_z(\mathbf{n},\mathbf{m})\mathbf{n}\exp(-i\mathbf{n}\cdot\mathbf{x})d\mathbf{n}$$
$$+\frac{1}{(2\pi)^2}\int(\mathbf{n}\cdot\nabla_{\mathbf{m}})^2 k_z(\mathbf{x},\mathbf{m})K_z(\mathbf{n},\mathbf{m})\exp(-i\mathbf{n}\cdot\mathbf{x})d\mathbf{n} - \cdots \quad \text{. (A8.14)}$$

The recognition that $\mathbf{n}\exp(-i\mathbf{n}\cdot\mathbf{x}) \Leftrightarrow -i\nabla_{\mathbf{x}}\exp(-i\mathbf{n}\cdot\mathbf{x})$, leads to the result

$$\hat{k}_z^2(\mathbf{x},\mathbf{m}) = k_z(\mathbf{x},\mathbf{m})k_z(\mathbf{x},\mathbf{m}) - i\nabla_{\mathbf{m}} k_z(\mathbf{x},\mathbf{m})\cdot\nabla_{\mathbf{x}} k_z(\mathbf{x},\mathbf{m})$$
$$+\frac{i^2}{2}\nabla_{\mathbf{m}}\nabla_{\mathbf{m}} k_z(\mathbf{x},\mathbf{m}) : \nabla_{\mathbf{x}}\nabla_{\mathbf{x}} k_z(\mathbf{x},\mathbf{m}) - \cdots \quad , \quad \text{(A8.15)}$$

where the third term in equation (A8.15) is a constant times the product of two-second rank symmetric tensors contracted over both coordinates.

By a similar process, as above, the expression for $\bar{k}_z^2$ equivalent to equation (A8.12) is

$$\bar{k}_z^2(\mathbf{x},\mathbf{m}) = \frac{1}{(2\pi)^2}\int k_z(\mathbf{x},\mathbf{m}+\mathbf{n})K_z(\mathbf{n},\mathbf{m})\exp(-i\mathbf{x}\cdot\mathbf{n})d\mathbf{n} \,. \quad \text{(A8.16)}$$

Equation (A8.16) differs from (A8.12) by the positive value of **n**; **n** is negative in (A8.12). The resulting asymptotic formula for $\bar{k}_z^2$ is

$$\bar{k}_z^2(\mathbf{x},\mathbf{m}) = k_z(\mathbf{x},\mathbf{m})k_z(\mathbf{x},\mathbf{m}) + i\nabla_{\mathbf{m}}k_z(\mathbf{x},\mathbf{m})\cdot\nabla_{\mathbf{x}}k_z(\mathbf{x},\mathbf{m}) + \frac{i^2}{2}\nabla_{\mathbf{m}}\nabla_{\mathbf{m}}k_z(\mathbf{x},\mathbf{m}):\nabla_{\mathbf{x}}\nabla_{\mathbf{x}}k_z(\mathbf{x},\mathbf{m}) + \cdots \quad . \qquad \text{(A8.17)}$$

Asymptotic formulae $\bar{k}_z^2$ and $\hat{k}_z^2$ are exact in the first term with all higher terms corresponding to error. The difference in sign of their odd ordered terms suggests that their average will increase the order of the error of the resulting symbol by canceling these terms. Also, because these terms are complex valued, removing them reduces the presence of uncontrolled complex terms that, in a recursive application, may lead to instability.

APPENDIX 9

THE ASYMPTOTIC FORMULA FOR c_N

Computing the spatial Fourier transform in c_N equation (6.9) gives

$$c_N(\mathbf{x},\mathbf{m}) = \frac{1}{(2\pi)^2}\int A^-(\mathbf{m}-\mathbf{k},\mathbf{m})\alpha^+(\mathbf{x},\mathbf{k})\exp(-i[\mathbf{m}-\mathbf{k}]\cdot\mathbf{x})d\mathbf{k}\,. \qquad \text{(A9.1)}$$

Equation (A9.1) can also be written

$$c_N(\mathbf{x},\mathbf{m}) = \frac{1}{(2\pi)^2}\int A^-(\mathbf{u},\mathbf{m})\alpha^+(\mathbf{x},\mathbf{m}-\mathbf{u})\exp(-i\mathbf{u}\cdot\mathbf{x})d\mathbf{u}\,. \qquad \text{(A9.2)}$$

Expanding α^+ results in

$$c_N(\mathbf{x},\mathbf{m}) = \frac{1}{(2\pi)^2}\int A^-(\mathbf{u},\mathbf{m})[\alpha^+(\mathbf{x},\mathbf{m})-\mathbf{u}\cdot\nabla_{\mathbf{m}}\alpha^+(\mathbf{x},\mathbf{m})+\cdots]\exp(-i\mathbf{u}\cdot\mathbf{x})d\mathbf{u}\,,$$

(A9.3)

that provides an asymptotic formula for c_N that is similar to that of c_P by recognizing that coordinates **u** arise as spatial derivatives of the Fourier kernal thus

$$c_N(\mathbf{x},\mathbf{m}) = 1 - i\nabla_{\mathbf{m}}\alpha^-(\mathbf{x},\mathbf{m})\nabla_{\mathbf{x}}\alpha^+(\mathbf{x},\mathbf{m}) + \frac{i^2}{2}\nabla^2_{\mathbf{m}}\alpha^-(\mathbf{x},\mathbf{m}) : \nabla^2_{\mathbf{x}}\alpha^+(\mathbf{x},\mathbf{m}) - \cdots \quad . \text{(A9.4)}$$